University of Neuchâtel

REALIZATION OF A MINIATURIZED ELECTRON BEAM COLUMN FOR LOW-ENERGY LITHOGRAPHY APPLICATION

A dissertation

submitted to the Faculty of Sciences of the University of Neuchâtel

to obtain the degree of Doctor of Sciences

by

Michel Despont

Ingenieer in Microtechnology Dipl. EPFL

Institute of Microtechnology

Rue Jaquet-Droz 1, CH - 2000 Neuchâtel

Switzerland

1997

IMPRIMATUR POUR LA THÈSE

Réalisation d'une optique électronique miniaturisée
pour des applications lithographiques à basse énergie.

de M. Michel Despont

UNIVERSITÉ DE NEUCHÂTEL
FACULTÉ DES SCIENCES

La Faculté des sciences de l'Université de Neuchâtel sur le rapport des membres du jury,

Messieurs N.F. de Rooij (directeur de thèse), H.-P. Herzig, P. Vettiger (Rüschlikon), P. Chang (Rüschlikon) et U. Stauffer (Bâle)

autorise l'impression de la présente thèse.

Neuchâtel, le 17 décembre 1996

Le doyen:

R. Dändliker

R. Dändliker

Contents

Summary

An array of miniaturized electron columns (microcolumns) working at low energy have great potential for lithography applications. A microcolumn features the flexibility and high resolution of e–beam technology, together with the throughput capabilities of parallel writing. In addition, working at low energy reduces the proximity effect inherent to e-beam lithography, and miniaturization reduces the cost of such a system.

The concept used was originaly developed by T.H.P Chang and is based on an STM stage to align the tip which is operated in field emission with respect to the axis of a miniaturized electron optical system. For low energy, such a system has been demonstrated an higher brightness than a conventional e-beam column.

In this work, means to microfabricate the components of a microcolumn working at 100 eV have been studied, developed, and applied. Special attention was given to developing processes suitable for batch processing of microcolumn elements or arrays of microcolumns.

Fabrication of miniaturized lenses was the main part of this thesis, and two different processes have been successfully used for this purpose. First, lenses were made of silicon membrane as the electrode and Pyrex as the dielectric spacer, and assembled by anodic bonding. Second, lenses were fabricated in a completely integrated silicon chip using an epitaxial structure and selective anisotropic etching to fabricate the electrode in a highly doped epitaxial layer. The electrode isolation is performed by *pn* junctions in reverse-bias

mode. In addition, preliminary experiment and fabrication of a double deflection system has also been performed.

For this purpose, the following techniques have been developed:

1. AC anodic bonding for fabricating the silicon membrane/Pyrex spacer/silicon membrane stack.
2. Electron beam exposure through thin membranes to perform high-accuracy alignment between the electrodes of the lens.
3. High-quality membrane and multi-membrane fabrication by selective anisotropic etching and silicon epitaxy.
4. Alignment procedure using thickness contrast with electron beam imaging.
5. Gold-silicon eutectic bonding to achieve a electronicaly conducting bond.
6. Technique allowing a freestanding electroplated structure on a glass wafer by using a photoetchable glass in which the exposed parts of the glass are used as a sacrificial layer.
7. Very high-quality reactive ion etching (RIE) process to fabricate holes in a silicon membrane with vertical walls and a wall roughness of less than 10 nm.
8. Selective passivation technique to prevent leakage currents at the silicon surface.
9. Low stress plasma enhancement chemical vapor deposition (PECVD) of a silicon oxide-nitride layer (SiON) for use as a mask for silicon membrane structuration without deforming the membrane.

Finally, first results of imaging and lithography with a 100-eV and 200-eV microcolumn are presented.

Chapter 1

Introduction : Challenge in sub–100 nm lithography

Lithography accounts for nearly 35 % of the cost of integrated circuit fabrication [1]. Presently the significant part of this is mostly done by optical lithography. Its leading position is explained by its high throughput and its relative simplicity. The next 10 years will be a turning point in microelectronic lithography, because the demand to reduce feature dimensions anticipates sizes which are not demonstrated by optical lithography. As an illustration of this evolution, table 1.1 gives the expected trend of the driving technology of dynamic random access memory (DRAM). The same predictions are made for the whole microelectronic world; for example microprocessors, high density logic chip, ASIC, etc. But this fact will not stop the need for smaller dimensions, and other techniques will start to be cost competitive for mass production. Hence, standard microelectronics will continue their down scaling. In addition new devices and applications like quantum effect devices will involve and do require sub-100 nm dimensions.

Optical lithography is currently the major technology to be used for the fabrication of VLSI chips, it is considered to reach its resolution limits at 180 nm by using 193 nm expo-

DRAM production year	1992	1995	1998	2001	2004	2007	2010
Feature size [nm]	500	350	250	180	130	100	70
Bits [bit]	16M	64M	256M	1G	4G	16G	64G
Processing cost [$/cm^2]	4.00	3.90	3.80	3.70	3.60	3.50	NA
Lithography cost [$/cm^2]	1.40	1.37	1.33	1.30	1.26	1.23	NA

Table 1.1: Estimated trend of the DRAM evolution for the next decade [2].

sure wavelength and phase shift masks [3]. Although optical lithography has constantly pushed its limits further down in the past, the sub-100 nm regime will most likely not be the optical lithography age. Therefore the following technologies are being considered to he the main techniques to play an important role for structuring sub-100 nm devices with high throughput:

1. X-ray lithography.
2. Electron lithography.
3. Ion lithography.

X-rays are generally used in proximity mode, where the mask is hold in close proximity to the wafer to be exposed. The key element is the mask, it consists of a very thin membrane (few microns thick) of Si, SiC, SiN or diamond and an absorbing layer of gold, tungsten or tantalum on top which is patterned by the structures to be exposed. The high resolution of this technique is due to the very low wavelength of the radiation greatly reducing the diffraction effects and the close proximity between mask and wafer. On the other hand the exposure wavelength should not be too small, otherwise the absorber layers need to he very thick which is quite difficult to pattern with sub-100 nm resolution. In practice, the wavelength used is between 0.4 nm and 1.2 nm (soft X-ray). The main

advantage of X-ray lithography is its throughput which is comparable to that of the optical lithography. However the technology is not yet mature with still many mask problems like membrane stress, distortion, stability, heating etc. to be solved. In addition, the approach is quite complicated and expensive because of the costly light source, vacuum operation and mask technology. Its resolution can be very high if the gap between the mask and the wafer is very small or in contact. Patterns with 30 nm of feature sizes have already been achieved in research [4], with a gap lower than 1 μm. But for ULSI (Ultra Large Scale Integration) this small gap is not realistic, because the exposed area must be as large as possible to have the highest exposure throughput as possible, and fabricating membranes as flat as I μm is not feasible. The manufacturing limit is currently considered at 70 nm, corresponding at a gap of 5 μm [5]. An interesting new idea to simplify the mask fabrication, is to use a reflection mask [6, 7]. In addition, masks are easier to fabricate and also reduction exposure can be done.

Electron lithography is the most established technique for large scale sub-100 nm lithography. The main technique used is the scanning of a focused electron beam on a wafer to expose shapes which can be as small as 5 nm [8]. Another advantage of focused e-beam is its depth of focus, allowing high resolution even over topographical steps on the wafer as they are present on microelectronic chips. The use of a very small focused beam to "draw" the structures results in very high resolution but it is a relatively slow process since the beam is addressing serially pixel after pixel. The throughput issue has been addressed by three approaches a) variable shape beam concept b) e-beam projection lithography and c) parallel beams. The variable shape beam is still a serial approach but it adapts the size of the rectangular beam dynamically according to the size of the shape to be exposed. The rectangular variable shape is formed by two mechanical apertures within the column. By changing the position of the two apertures, the rectangular beam shape can dynamically be adapted to the size to be exposed. This greatly reduces the

number of exposed pixels and hence considerably improves exposure throughput. This concept is today widely used in many commercial systems which operate in mask houses and are used in optical/e-beam mix-and-match wafer fabrication [9].

In electron projection systems, the pattern on a stencil mask is being projected (with or without demagnification) onto the wafer [10, 11]. Such masks are even more difficult to realize than for X-ray lithography and the resolution hardly reaches the 100 nm limit because of coulomb effects which cause aberrations [12-14].

The third approach to improve throughput makes use of parallel beams which are generated by an array of lenslets which are illuminated from a single cathode [15, 16]. Although parallel approaches are inherently interesting for high throughput, the bottleneck of this approach seems to be homogeneity and stability of the beamlet array.

Another parallel electron-based concept is proposing to use an array Scanning Tunneling Microscopes (STM) operating in field emission mode with the sample to be exposed in close proximity. STM lithography can achieve very high resolution by hydrogenisation and oxidation of silicon featuring sub-10 nm resolution [17], or by structuring self-assembled monolayers (SAM) with 20 nm feature size [18, 19]. However, the use of the sample as a part of the probe forming optics leads to severe tip-target interaction problems, in addition throughput needs to be improved.

More recently, an interesting new approach has been proposed and explored by Chang et al [20] which is based a field emitter as proposed by Spindt [21], STM-type field emission alignment, and microfabrication techniques to build a miniaturized e-beam column. Besides its compactness, small size and low cost, the approach has great potential for batch fabrication of lens and column arrays. The latter feature and the high resolution of focused e-beam makes the microcolumn array very attractive for sub-100 nm high throughput lithography applications.

A fundamental problem of e-beam lithography is the scattering of primary-,

backscattered- and secondary electrons when they penetrate, reflect or escape from the substrate or resist layer. This generates unwanted exposures of the resist layer depending on the exposures within the proximity of the pixel/shape of interest. Depending on proximity shapes, the exposed structures may be over-exposed or even deformed in its shape. This limiting effect for e-beam lithography is called proximity effect and was first described and characterized by Chang [22]. The problem has been reduced/solved by several software proximity correction techniques which calculate for complete circuit layouts the total dose for every single shape received by the primary, backscattered and secondary electrons from the own and proximity shapes. Afterwards, the program determines a new primary dose for every shape such that each shape of the layout receives the same total dose. Many publications have successfully demonstrated uniform exposures and undistorted patterns for even large and dense layouts. However, for dense and large layout, the program require substantial computer power. Other solutions use very high (> 100 keV) beam energies to make the scattering range much broader but also more uniform or much lower beam energies (< 1 keV) to reduce the scattering range below the minimum gap between two shapes.

Ion lithography makes use of the same principle concepts as electron lithography but is using ions instead of electrons. Its main advantage compared to electron lithography is the very low scattering range of the ions which greatly reduces proximity effect. However its disadvantage is damage or modification of the underlaying layers. The problem can be solved by using multilayer resist technique whereby the ions only expose the top imaging layer and do not penetrate through the thick bottom layer, hence the underlaying layer are not exposed to the ion beam. However the techniques requires additional dry etch steps to transfer the pattern into the bottom layer. Prototypes of ion projection lithography systems are already being in use and tested [23]. But as with all future mask projection systems, the membrane masks are very difficult to make and their life time is still a

problem since ion milling is degrading the mask quality. Space charge effects limit the resolution to about about 90 nm [24]. Similar to e-beam, ion lithography is also possible with focused ion beams. Systems are commercially available which are mostly used for machining and deposition of materials to repair masks and circuits or prepare samples for TEM investigations.

In recent years many other approaches have been reported for sub-100 nm lithography techniques, they include atomic lithography using light force [25], nanoscale modification of phase change materials with near-field light [26], field evaporation of metal clusters [27], or atomic manipulation for patterning on ultra thin film [28]. All these techniques are in their very early and exploratory stage and need considerable more work to be judged as valuable future approaches. The clearly most interesting and promising approaches which have been reported lately make use of imprint and stamping techniques. Provided that high quality and durable molds can be fabricated, they offer great potential for future high throughput sub-100nm lithography [29, 30]

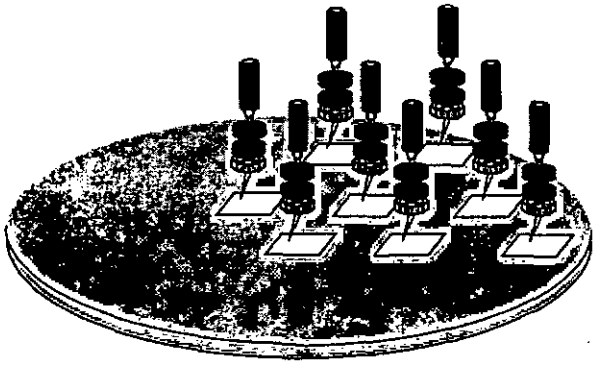

Figure 1.1: Basic concept of arrayed microcolumn lithography.

In this context, the idea of using an array of miniaturized *focused* low energy electron beam columns, proposed by Chang [31] as is shown in figure 1.1, offers great potential as a lithography tool for the future. It has the flexibility of the scanning based lithography (no–mask needed), high deflection speed, and high throughput. The miniaturization allows the arraying and hence is increasing throughput to be competitive with optical and X–ray lithography. The miniaturization also reduces the fabrication cost of such tools. The low energy ($\leq$ 1 keV) drastically reduces the scattering of electrons in the material, and will avoid many of the proximity problems. To summarize, table 1.2 compares the keys points of the most promising lithography methods for the near future.

Lithography concept	System cost	Throughput	Resolution	Exposure over a step	Vacuum	Other advantages	Other disadvantages
Optical (193 nm Stepper)	+ +	+ + +	- -	- -	No		
X–ray (synchrotron source)	- - -	+ + +	+ +	- -	Yes		Mask fabrication
Focused e–beam (conventional tool)	- -	- -	+ + +	+ + +	Yes	No mask needed	Proximity correction
Focused ion beam	- -	- -	+ + +	+ + +	Yes	No mask needed	induce damage
Electron Projection	-	+ + +	- -	+ +	Yes		*Proximity correction* Mask fabrication
Ion Projection	-	+ + +	- -	+ +	Yes		Mask fabrication
Arrayed STM	+ + +	+	+ + +	- -	No		Tip scratch
Stamping	+ + +	+ + +	+ + +	?	No		mold quality and degradation
Arrayed e–beam microcolumn	+ +	+ +	+ + +	+ + +	Yes	No mask needed	

Table 1.2: Comparison of several key points between the most promising lithography concepts for the near future.

Provided that arrays of microcolumns can be fabricated, this technique becomes very

attractive for sub-100nm lithography applications even for mass production. In addition, microcolumns (single and arrays) operating at low energies have other interesting applications in for *in-situ* inspection, microscopy, metrology, testing, recording, and holography [20, 32, 33].

It is the objective of this thesis to explore schemes and fabrication techniques suitable for integrated lens and deflector arrays because the parallel microcolumn approach is an attractive future possibility for lithography and many other applications.

Chapter 2

From a standard electron system to a miniaturized system

In this chapter the concept of e–beam lithography will be introduced by the presentation of a vector scan e–beam tool, which is the exposure technique foreseen to he used with the microcolumn. A presentation of the low energy miniaturized electron beam column will follow, hy explaining what are the henefits of downscaling and work at low energy, and also their limitations. To place this work in the present state of the research in this field, an overview of other research teams working with microcolumns will be done. And, finally, the objective of this work will be specified.

2.1 Concept of a focused electron beam lithography tool

As already mentioned in the introduction, e–beam lithography is actually most often used to pattern sub–100 nm feature size. Its concept is perfect for experimental device fabrication in research or for mask fabrication, where the exposure time is not the crucial

issue. Basically, the focused electron beam is electromagnetically deflected over the surface of the resist-coated sample in such a way as to fill in tbe pattern. When, for example, using a positive tone process, tbe chain of tbe resist polymers of the exposed areas (or more precisely tbe volume) are dissociated by the energy supply by the beam producing a molecular weight contrast between tbe exposed areas and the not-exposed areas. By using an appropriate developer, this contrast can be revealed by a subsequently higher solubility of the exposed part.

Electron beam lithograpby systems are currently available in a large range of capabilities and degree of sophistication. They consist mainly of four subsystems: an electron optical column, a pattern generator and a beam deflection electronics, a specimen stage, and a mark recognition system (Fig. 2.1a).

The electron optical system uses the conventional beam forming concept of a Scanning Electron Microscope (SEM), wbere a condenser and an objective lens focus the electron beam onto the sample surface by demagnification of the image of a tbermionic electron gun source. Tbe beam deflection scheme mostly used is the so-called vector scan technique, wbere for efficiency the beam addresses only the pattern areas requiring exposure. The usual approach is to decompose the pattern into a series of primitives shapes, e.g. rectangles and parallelograms, whose specifications can be stored in a condensed data format. Tbe role of the pattern generator is to generate digital beam deflection signals corresponding to tbe filling in of these primitive shapes on a discrete position grid (Fig. 2.1b). Tbe resulting X,Y position signal is used to drive the deflection coils (or electrostatic plate) on the column, and the beam is stepped with a dwell time at each grid point corresponding to the assigned area exposure dose for the resist. It can also be turned off completely by the pattern generator (blanked) wben moving from one primitive shape to tbe next.

Because the exposure field is limited in practice by deflection aberrations, a large pattern is usually subdivided into a series of fields, which are written sequentially. Tbe

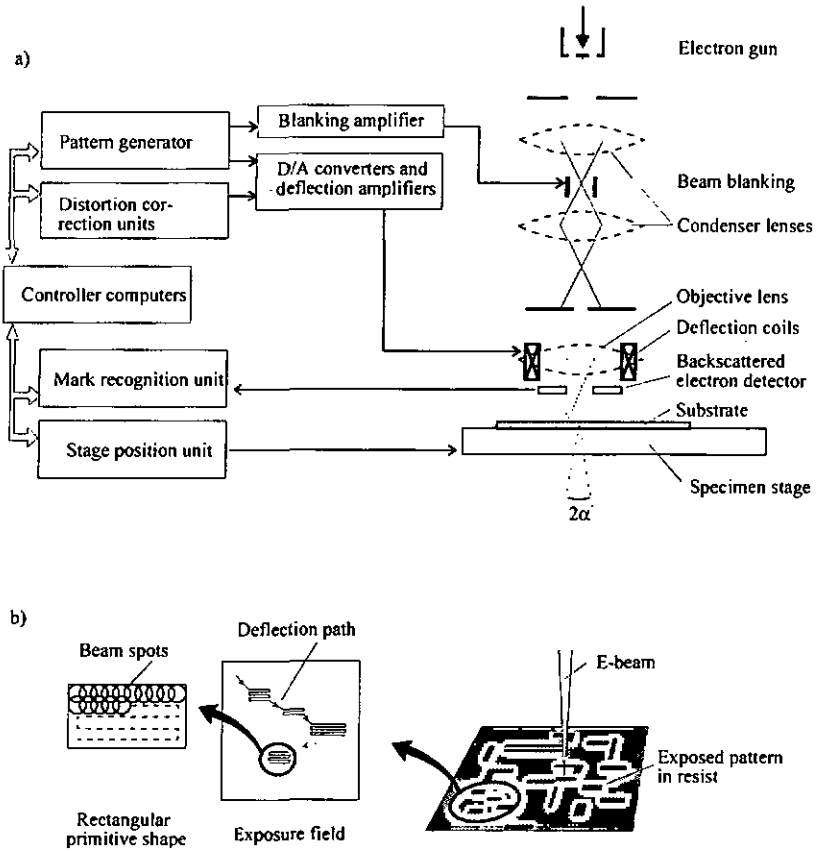

Figure 2.1: a) Schematic electron beam litbograpby system. b) Vector-scan exposure scheme. The sample surface is subdivided into exposure fields(chips), in wbich the pattern is broken down into primitive shapes. Each primitive sbape is filled in (exposed) by stepping tbe beam position at regular intervals over its area.

necessary sample movement from one field to the other (stitching) is provided by a motorized stage, and its position is controlled to a high precision by laser interferometry.

The stepper doing the stitching is also one of the key elements for any other kind of lithography system (X-ray, electron, ion, optical) for sub-100 nm lithography.

Finally, in order to ensure proper layer to layer positioning of the pattern, the lithography system is capable of using alignment marks previously defined on the sample surface. The marks are located in the coordinate system of the beam deflection by relying on a high contrast in backscattered electron signal. An elaborate set of automated calibration procedures can then be used to map the coordinate system of the deflection to that sample, and to correct for various distortions (offset, rotation, non-orthogonality and improper scaling).

The minimum achievable feature size is strongly influenced by two factors inherent to the electron beam: the diameter of the focused electron beam, and the so-called proximity effect due to the back scattering of electrons. The beam current I, the exposure field size S^2, the beam-stepping frequency f, and the dose D required for a given resist are related by a dependence of the form:

$$I \propto DfS^2,$$

which implies that an optimal choice of the beam current results from a trade-off between the exposure field size, the sensitivity of the resist, and the writing time. Both the field size and the stepping frequency can only be chosen in a limited interval due to hardware limitation. As an example of a commercially available system, the characteristic data for the ZBA 31 H lithography system from Jenoptik Technologie GmbH is given in table 2.1. A second main limitation to the achievable feature size originates from the undesired backscattering of incident electrons in the depth of the sample. This results in dose contribution to resist areas which are remote from the point of incidence of the beam, so that features of various sizes do not necessarily develop out simultaneously when exposed with the same area dose [34]. This is referred to as the proximity effect, since it depends strongly on the density of the pattern layout as well as on the features dimensions. Most

schemes employed for the correction of the proximity effect consist of assigning lower doses to certain features so that the effective dose received by all exposed areas is uniform [22].

Wafer size	up to 200 mm	Throughput	2 to 5 6"wafers/h
Acceleration voltage	20 kV	Cathode	LaB_6
Beam format	Shape beam 0.1 to 5 μm	Interferometer accuracy	5 nm
Resist sensitivity	0.1 to 1000 $\mu C/cm^2$	Stitching accuracy	0.05 μm (3 σ)
Overlay accuracy	0.06 μm (3 σ)	Resolution	0.1 μm

Table 2.1: Specification of the ZBA 31 H lithography system from Jenoptik Technologie GmbH [35]

2.2 Lowering the e-beam energy and miniaturization of the e-beam system

Advantages of the microcolumn have already been enumerated in the introduction. But to achieve or to use such tools for lithography applications, different problem need to be solved and different rules need to be applied, such as improving the fabrication tolerance and using new very thin resists.

2.2.1 Working at low energy

One of the main resolution problems for VLSI in electron beam lithography is the proximity effect due to backscattered electrons. In a microscopic point of view, the incident electron striking in the material can follow one of this three schemes:

1. unscattered electrons, which pass through the sample without deflection or suffering any energy loss,

2. elastically scattered electrons, which are primarily collisions due to the screening of nuclear and can result in large ($> 90°$) deflections, although most are smaller angle deflections. Some of the electrons can also be scattered at phonons, suffer small (1-10 meV) energy losses and are indistinguishable from elastically scattered electrons.

3. inelastically scattered electrons, which the angle of scattering depends on the energy lost by the incident electron. This occurs as discrete events, with the generation of secondary electrons from the outer shell at low energy (up to $\sim$ 50 eV and with a maximum around 2 to 5 eV), excitation of density oscillations in metal electron plasmas, inner-shell ionizations that lead to X–ray emission and Auger electron emission, creation of electron-hole pairs followed by photon emission (cathodoluminescence), transition radiation, and lattice vibrations (phonon excitation).

Generation of secondary electrons by the inelastically scattered primary electrons is useful for lithography, because one primary electron can hence generated many secondary electrons which will participate at the resist exposure. In contrary, the elastically scattered electron process, is a draw-back for the lithography application because, depending on the energy, the scattering can bring these electrons far away from the beam impact and generate secondary electrons not only at the desired place but also around this place. To evaluate the effect of this phenomenon to lithography applications, the following "Two Gaussian Function" is used:

$$D(r) = \frac{1}{\pi(1+\eta)}\left(\frac{1}{\alpha^2}e^{-r^2/\alpha^2} + \eta\frac{1}{\beta^2}e^{\frac{-r^2}{\beta^2}}\right).$$

This formula describes the absorbed dose at a distance r from the incident beam due to forward scattering (in the first term) and due to the backscattering from the substrate.

The dose is normalized to the dose needed for exposing an infinite shape in a resist. α describes the lateral extent of the exposure due to the primary and small angle scattered electrons, β is the extent of the backscattered electron exposure, and η is the relative contribution of the backscattered electron exposure to the total exposure. α depends on the diameter of the incident beam, β on the energy through the mean free path of electrons in the material, and η to the sample material, while depending on the atom number Z, the screening effect of the nucleus is more or less large. These parameters are determined experimentally for each energy and substrate used [36].

To reach very high resolution e-beam lithography, two techniques are applied in order to cope with the proximity effect: (1) Applying complicated proximity correction computing to modulate the dose given for each part of the pattern versus the density of the surrounding area to be patterned, using the above formula or, (2) increasing the accelerating voltage up to 100 kV so that the higher energy electrons forwardscatter less in the resist and the backscattered electrons emerge over a large area ($\sim$ 20 μm diameter) and provided a relatively constant dose background (β is large).

But a third method can be applied; it consists of using low energy electrons ($\leq$ 1 keV) to minimize the penetration depth of electrons in the materials and so the area where backscattered electrons emerge at the surface. Hence the energy deposited in the resist is localized very close to the beam impact and does not contribute to the exposure any further. Figure 2.2 [37], shows a Monte Carlo simulation of penetration depth of electrons in a silicon sample covered by 66 nm of PMMA. It clearly shows, the confinement of electrons with lowering of their energy; but also, by lowering their penetration in the substrate, much less secondary electrons are generated in this substrate, while more are generated in the resist layer. Hence because electrons do not interact anymore with the substrate, the exposure gets independent of the substrate. It also leads to a higher efficiency of lithography processing for small features, since practically all secondary electrons are generated

in the resist and they can all interact with the polymer chain of the resist. Such a trend of reduction of the required dose with respect to the energy of the electron beam was observed many times for energies down to several hundred electron-volt with, of course, a resist thickness adapted to the penetration depth of the electron beam energy [37-39]. However, other experiments show that for very low energies (from several electron-volts to one hundred electron-volts), an inverse dependence of the required dose is observed [40, 41]. In fact the approximation of the "Two Gaussian Function" is no longer valid at low energies. An optimum dose electron energies can be found to minimize the dose required to exposed a resist.

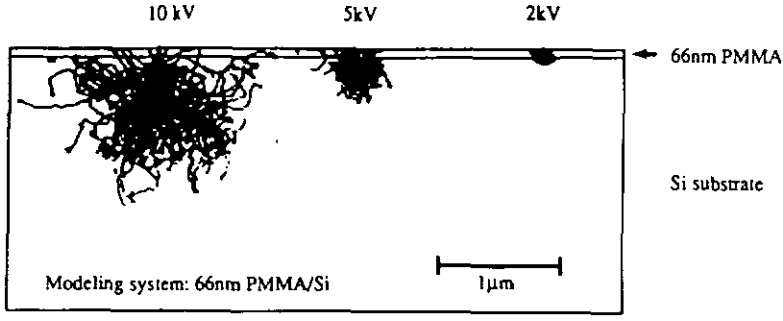

Figure 2.2: Monte Carlo simulation illustrating that less energy creates a smaller interaction area, a smaller lateral electron scattering range, and a thinner surface imaging layer (*after* [37]).

At very low energies, the electrons do hardly react with the resist or with the material since they are not sufficiently energetic. This is illustrated by the mean free path of electron versus their energy in different materials as shown in figure 2.3. Independent of the material, there is a minimum mean free path, representing a very high probability to

have an interaction of an electron with the material.

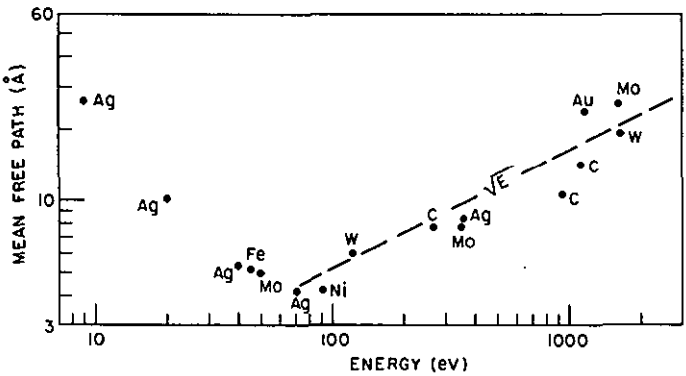

Figure 2.3: Mean free path of electrons in various materials (after [42]). Note the minimum near 75 eV, and the increase approximatively proportional to $\sqrt{E}$ between 100 and 2000 eV.

This minimum of the mean free path at $\approx$ 75 eV was the principle motivation of starting a project to investigate the realization of a miniaturized electron system working in the 100 eV range. But of course, looking at the extremely low depth of penetration of such electrons, new resists with a thickness in the order of 1 nm must he developed which can mask well enough for standard microelectronic processes like etching, implantation, etc. Possible candidates are, for example, passivation layers and self-assembled monolayers (SAM). Both have successfully been used in scanning tunneling microscope (STM) based lithography [40, 19].

A last advantage of low energy, is that since the electron penetration in the material is very low during the lithography, the damage caused to the underlaying material, which can be part of a microelectronic device, is reduced.

2.2.2 Miniaturized e-beam column

To work at low energy, the miniaturization of the electron beam column is a necessity to reaching a high quality electron beam. As we will see later, by downscaliog the column, the effective brightness and the beam diameter can both be improved. However, the miniaturization has its limits (especially for the lens fabrication), given by the fabrication tolerance as well as the electrical breakdown voltage in the vacuum. The tolerances in the microfabrication techniques is for the best case in the 10 nm range. This will limit mainly the minimum diameter of the holes in the electrodes, the bores, to about 1 μm, to keep an acceptable roundness and smoothness of the bore shape [43]. The electrical breakdown, will mainly limit the minimum spacing between two electrodes for a given applied voltage. Generally, this value in the vacuum is on the order of 10^4 V/mm [20]. With very small dimension (in the micrometer range) this value can be 2 to 4 time higher [44].

The miniaturization of the e-beam system down to an inch cube offers other significant advantages. An obvious benefit in having a very small tool to be used as a mini-SEM is cost reduction in mass production. But new applications would be possible, like in-situ inspection in, for example, the chamber of an evaporator or of an MBE (Molecular Beam Epitaxy). It can also be used in conjunction with an AFM and an STM to realize a nanolab with a wide type of surface inspection and scan range. Its small size allows also e-beam system to be built with many of such microcolumns. As already mentioned, an array of these columns would overcome the main problem of electron beam lithography; namely, the throughput. In addition, the throughput is also a key challenge in meteorology, and such arrays can be attractive for such a field. Non-contacting integrated circuit testing can also be an application; for example, the microcolumn can be used for injecting charge in the electrical circuit, and also to visualize the resulting signal with another column in voltage contrast imaging. Other applications can be found as a miniature spectrometer

to provide material analysis capability, or using a microcolumn in a flat panel display or for high density storage [31].

2.3 State of the art in microcolumn fabrication

If in the previous discussion the idea of a miniaturized electron system was mentioned [45-47], the actual starting point was done by Philip Chang and co-workers at IBM T.J. Watson Research Laboratory [48, 49, 20]. His idea was to combine micromachined lenses with an Scanning Tunneling Microscope (STM) where the tip will be used in field emission mode and where the scanner is used to align the tip with the source lenses, creating a so-called STM Aligned Field Emission (SAFE) microsource. This configuration allows one to use a broad type of tip material, to bring the tip far away from the lenses, for preparation (flash annealing) or for exchanging. It also allows one to have a very precise positioning with regard to the lens axis, which is crucial for the quality of the beam. Chang also developed a selective scaling method [20] showing a significant improvement of the effective brightness over a conventional source with low energy electrons. In his work, he focused mainly on the 1 keV microcolumn, which is a compromise between the possible miniaturization and the problems you can have with lower energy (charging effect, coulomb interaction). To this date results as good as 10 nm resolution at 1 nA and 1 keV have been achieved by this group [50]. Their present setup is shown in figure 2.4. They used as a source, monocrystaline tungsten tips, transition metal carbide tips in field emission [50], and Zr/O/W Schottky emitters [51]. Lenses are made out of silicon membranes as electrodes and Pyrex as spacers. The assembling is made by an anodic bonding technique and aligned manually under an optical microscope [43]. The deflection system was done by fine machining, but a micromachined version is planed [52]. They also fabricated an integrated secondary electron detector based on a Metal-Semiconductor-

Metal diode (MSM) [53]. This Ph.D. work was based mainly on the approach of Chang which, to my knowledge is the only demonstrated technique with a performance good enough to be competitive with a conventional e-beam system.

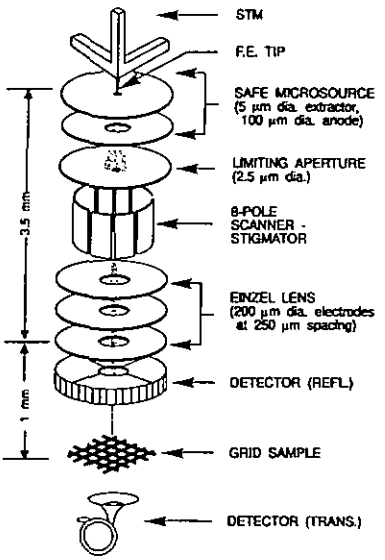

Figure 2.4: Current microcolumn setup used by T.H.P. Chang and co–workers [50].

However, other approaches were also developed to fabricate a specific element of the microcolumn. D.A. Crewe and co-workers at the Microfabrication Application Laboratory of the University of Illinois at Chicago proposed a kind of "self assembled" technique for the fabrication of the lenses. While the electrodes are also made out of silicon membrane, the spacers are made by optical fibers. In the electrode chips, grooves are machined to receive the fibers and thus have an alignment between the electrodes [54, 55]. They also studies the feasibility of an array of microcolumns made of capillary tubes (cover with gold) as electrodes positioned in silicon V–grooves [56]. R.F. Pease and co-workers

of Stanford University have investigated the possibility of using miniaturized magnetic lenses and more recently started to study the performance of a microcolumn working at 10 keV with a final retarding electrode reducing the energy to 100 eV at the landing [57]. D. Rugar's group had also fabricated a miniaturized magnetic lenses [58]. The National Nanofabrication Facility of Cornell University are also involved in microcolumn study, mainly by the fabrication of a fully integrated gun (tips and electrodes) [59, 60]. Tips are made in silicon, and electrodes of tungsten are deposited and patterned by a plating technique. Precise alignment of electrodes is done by adding an electrostatic actuator to the electrode structure. They are also involved in the fabrication of Titanium Nitride Coated Tungsten cold field emission sources [61]. Micron-scale lenses were also fabricated by Fink and co-worker in IBM Zurich Laboratory in collaboration with Philips. They have tested two element lenses for holography applications [44]. The technique used, is a combined thin film technology and Focused Ion Beam (FIB) drilling. Finally, at the University of Tübingen, in the group of D.P. Kern, activities in this field have been started few years ago mainly with integrated secondary detectors based on MSM diode [62, 63], but now extended to microlenses fabrication [64].

2.4 Objective of this thesis

The goal of this work is to microfabricate the elements of a microcolum working at 100 eV as shown in figure 2.5. As already mentioned, this work is based on the Chang set-up. The same SAFE approach will be used, but with a configuration more suitable for lower energy (100 eV). It consist of:

1. A scanning tunneling microscope (STM) operated in field emission mode
2. A source lens to extract and accelerate the electrons from the tip, and to limit the beam diameter with an aperture.

3. A scanner-stigmator stage, to scan the beam and correct its astigmatism.

4. Ao ohjective lens to focus the beam at the sample level.

Because we are maioly focusing on lithography applicatioos, a special effort was done to find fabrication solutions allowing the hatch processing of microcolumn elements, or even tbe direct fabrication of arrayed elements. If a parallel e-beam lithograpby system is to have the potential to compete with optical lithography in terms of throughput and effective cost of the lithography process, tben the array must contain hundreds of single columns [31]. It would be not realistic to process and to assemble the microcolumns into such a huge array by serial processiog. However, the batch processing can not be performed to the detriment of quality; e-beam lithography must acbieve a sub-100 nm resolution io order to be attractive.

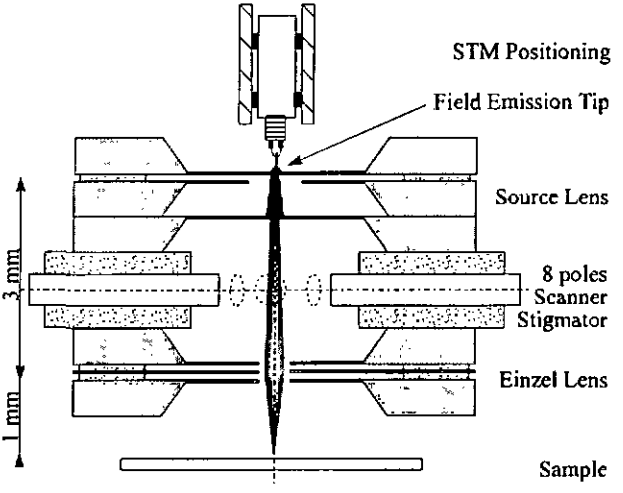

Figure 2.5: Basic setup of the microcolumn built-up during this Pb.D. work.

The above cited group working in this area did not really resolve the problems of batch processing. This is apparent if we look at the methods for the fabrication of the stack forming the lenses used by the Chang group, the method used by the Crewe group or the method used in the Cornell University. The assembly and the alignment in the first group are made manually under an optical microscope with the help of a micromanipulator. In the second group, they use reference V-grooves made in the silicon chips containing the different electrodes of the lens. The chips are assembled together trough an optical fiber insuring by its positioning in this groove the alignment. In the third group, it is planned to integrate actuators for doing the fine positioning of each electrodes. In the first case even if the result is quite good (alignment in the 1 μm range was achieved [43]), it is not really a simple process suitable for large array fabrication. In the second case it is more batch processing oriented, but the accuracy of such a technique is not very high (around 5 μm) and certainly not enough for high-resolution optics. The third case allows batch processing, but shifts the problem to another place; i.e. having additional wiring and electronic control for positioning each electrodes individually, and then for the whole array.

It is not a simple problem, since this is really a 3D microfabrication. The lateral accuracy of the electrodes alignment is in the range of the very high quality microprocessing (sub micrometer), hut this alignment is between two devices which are usually not in the same chip, and which are separated vertically by a couple of tens of micrometers. It is a very specific problem which has not already been solved in low cost fabrication manner suitable for fabricating arrays of microcolumns.

Developing new techniques allowing the fahrication of such devices is one of the goals of this thesis. This is true not only for the lens, but also for the octupole. Two parts of the microcolumn will not he discussed: the tip as was fabricated by my colleague Camille Stebler [65], and the detector. A hrief survey of both of these topics is done in

the following chapter to have a global overview of the system. Also, magnetic lens theory will not be treated since even if from the aberration point of view, they are better than the electrostatic lenses, it is really quite difficult to realize them in very small dimensions.

Chapter 3

The miniaturized electron column system

In this chapter, an overview of the different parts of the microcolumn shown in figure 2.5 is presented. The electron optics is described in such a way so as to give an intuitive understanding of how electrons can interact with electro-magnetic fields to be slowed down, accelerated or deviated. The general rules of T.H.P Chang approach to optimize the electron optics of the microcolumns is also described. To have more information about the theory of electron optics, there is references [66-70], and for the microcolumn optimization, there is [48, 20, 50].

3.1 Electron optics

When a charged particle travels trough a region containing a magnetic field or/and an electrostatic field, forces will be exerted on it so as to deflect and alter its speed. This effect is described by the equation of motion;

$$\mathbf{F} = m\ddot{\mathbf{r}} = -q(\mathbf{E} + \mathbf{u} \times \mathbf{B}).$$

Where **F** is the force acting on an electron having a charge q, a mass m, a speed **u**, and a trajectory r, while passing through an electric field **E** and a magnetic field **B**.

The term of electron optics is used because all electrostatic and magnetic fields with either circular or planar two-dimensional symmetry possess the properties of optical-light lenses. They can project electron-optical images, or form highly focussed spots of electrons. Useful descriptions of electron trajectories can thus he ohtained hy applying the laws of geometric optical image projection. Hence the electron optic system can he simplified hy talking ahout optical planes and focal, rather then needing to have a complex description of the electro-magnetic field distribution. One major difference, however, between the two optics is that the electrons have much more aberration, since the refracting regions formed hy the electro-magnetic field cannot he shaped as well as the glass lenses used in light optics.

This similarity between electron and light optics is illustrated hy the law of refraction of an electron in an electrostatic field, which is the hasis of electron optics. We assume an electron traveling at a constant speed u_1 through a region of uniform potential V_1. Suppose the electron passes through a poteatial step into another space of uniform potential V_2. At the step, the path of electron will suddenly change as shown in figure 3.1. Assuming that potential V_2 is greater than V_1, the normal velocity component u_y of the electron will be increased, causing the electron to accelerate in a direction perpendicular to the step. The tangential component u_x of the velocity, remains unchanged. Expressing electron speeds in terms of the potential,

$$\frac{\sin\theta_1}{\sin\theta_2} = \frac{\sqrt{V_2}}{\sqrt{V_1}}.$$

This equation is the same as Snell's law in light optics, where the square root of the potential is equivalent to a refractive index. Whereas light travels more slowly in a material of higher refractive index, electrons travel faster as the voltage is increased. Even if this concept of voltage step is not realistic in electron devices, a gradient of potential

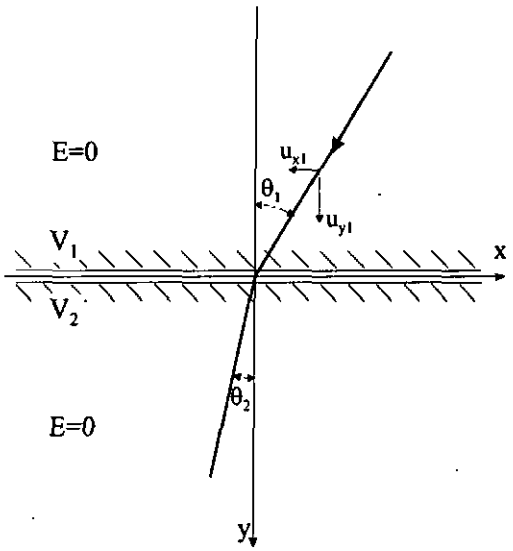

Figure 3.1: Refraction of electron trajectory at a step change in potential.

can be seen as a multitude of small voltage steps, and from this an equivalent step at a given location can be associated. This is used in finite elements numerical computation under the paraxial approximation.

The term paraxial means that only electrons ray closed to the optical axis are taken into account, and therefore only electron paths at small angles with respect to the axis are considered.

3.2 Electron emission

To have electrons emit out of a conductor, they must overcome the work function Φ_0 due to the surface potential. This can be done (1) by increasing the temperature that some electrons have an high enough energy to overcome the potential barrier, namely

thermionic emission, or (2) by tunneling of electrons through the potential barrier by applying a very high electric field (up to 10^9 V/m), the cold field emission, or (3) by lowering the potential barrier upon application of an electric field and by increasing tbe energy of electrons with a temperature increase, the Schottky emission. Tbese three kinds of emission, are illustrated in figure 3.2. These different possible operations of an emitter coupled with a wide range of materials and tip shapes, offer many different characteristic of emission. Tbe most important properties of an electron emitter for use in a microcolumn are:

1. The beam energy spread
2. The size of the virtual source
3. The beam current noise
4. The angular current intensity
5. The operating vacuum required
6. The stability of the geometry and the emission distribution
7. The processing required to prepare the tip during operation

At low energy, the heam spread is an important factor since it will influence the chromatic aberration wbich is proportional to tbe ratio between the energy spread and the mean emitted energy. For lithography application, a high angular current intensity and a very stable emission are required, because of dose and bomogeneity of the dose consideration.

Thermal emission is not suited for microcolumn application, because of its high energy spread emission, its relatively low emission density, and tbe high temperature required to bave a sufficient emission current (up to $\sim$ 2000°C) which can affect tbe other parts of the microcolumo, since tbe emitter work in close proximity to the optic column.

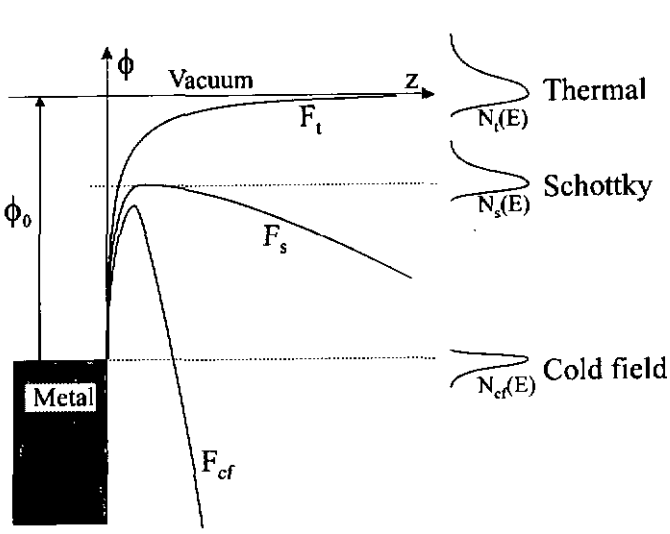

Figure 3.2: Diagram of the electron potential energy at the surface/vacuum interface showing the potential barrier deformation (F) due to the electric field applied and the emission energy distribution (N(E)) for the thermal, Schottky, and cold field emission.

The cold field emission cathodes most commonly used are fabricated from <310> and <111>-oriented tungsten. The slightly oxidized, <100> direction is sometimes used since it yields, as does the <310> and <111> directions, a low work function plane on the emitter apex. Typically the radii of the cold field emission cathodes are < 0.1 μm. In contrast the Schottky emission cathode most commonly used is a ZrO coated, W<100>-oriented emitter which provides a substantial, but localized, lowering of the work function from 4.6 to 2.8±0.2 eV for the (100) plane. In addition, the Zr/O/W(100) cathode is extremely thermally stable due to the low volatility of the ZrO layer and the underlaying tungsten at the operating temperature of ~1800 K. Table 3.1 presents several typical values of the field emission and Schottky emission tips described above.

	Schottky emitter	Cold field emitter
Current stability $\delta I/I$ [%]	0.1 to 1	4 to 6
Angular current density [mA/sr]	0.2	0.2
Tip radius [μm]	0.3 to 1	< 0.1
Energy spread ΔV [V]	0.3 to 1	0.2 to 0.3
Working pressure [torr]	$<1x10^{-8}$	$<1x10^{-10}$

Table 3.1: Summary of the various emission parameters for the Schottky emission and cold field emission cathodes.

Both of these tip types have advantages and disadvantages for low energy lithography applications. The Schottky emitter has an higher stability than the cold field emitter, which is crucial for the lithography process. For example, a current fluctuation of less than 1% in a few hours, is required for lithography. This is not the case with cold field emitters. Nevertheless, for our experiment we will use cold field emission cathodes, since their fabrication are simpler, and because at very low energy the energy spread emission will be a bigger problem than with a system working at a more conventional voltage. Finally to demonstrate the feasibility of microcolumns for low energy lithography, the high current stability is not that critical.

In our experiment, therefore, we have used DC electrochemically etched single crystal W<111> and W<310> wires (Ø 0.125 mm) [71]. These types of source have a virtual source size in the 5 nm range.

3.3 Electrostatic lens

In this section, the focusing effect of an electrostatic lens is described in an axially symmetrical system and under the paraxial approximation. The system will he describe in cylindrical coordinate (r, z, ϕ). Since the system is axially symmetrical, the potential is oot dependent on ϕ. We assume a power-series expansion io r^2 for the potential [66],

$$V(r,z) = V_0(z) + c_2(z)r^2 + c_4(z)r^4 + ...,$$

where $V_0(z)$ is the potential on the axis. The potential distribution is described by the Laplace equation,

$$\nabla^2 V = 0,$$

where V is the voltage potential distribution given hy the electrode geometry and the resultant shape of the equipotential line. To determine the coefficients, tbe Laplace equation is used in cylindrical coordioates and with oo depeodence on ϕ,

$$\frac{1}{r}\frac{\partial}{\partial r}(r\frac{\partial V}{\partial r}) + \frac{\partial^2 V}{\partial z^2} = 0.$$

Performiog these operation on the power series,

$$\frac{1}{r}\frac{\partial}{\partial r}(r\frac{\partial V}{\partial r}) = 2^2 c_2 + 4^2 c_4 r^2 + 6^2 c_6 r^4 + ...,$$

$$\frac{\partial^2 V}{\partial z^2} = V_0'' + c_2'' r^2 + c_4'' r^4 + ...$$

The power series is therefore,

$$V(r,z) = V_0(z) - V_0''(z)\frac{r^2}{2^2} + V_0^{IV}(z)\frac{r^4}{2^2 4^4} - ....$$

This equation allow us to koow the whole potential distribution by just koowing its distribution on the axis z.

In the case of the equation of motion, and taking into account that oo magnetic field is applied and there is no dependence on ϕ,.

$$\ddot{r} = -\frac{q}{m}\frac{\partial V}{\partial r}, \quad \ddot{z} = -\frac{q}{m}\frac{\partial V}{\partial z}.$$

Time can be eliminated and the two equations combined into a single radial trajectory equation,

$$\dot{r} = \frac{dr}{dz}\dot{z}, \quad \ddot{r} = \frac{dr}{dz}\ddot{z} + \frac{d^2r}{dz^2}\dot{z}^2;$$

and by using the energy conservation

$$\frac{1}{2}m(\dot{r}^2 + \dot{z}^2) = -qV,$$

the two equations of motion can be fused into one,

$$2V\frac{d^2r}{dz^2} = (\frac{\partial V}{\partial r} - \frac{dr}{dz}\frac{\partial V}{\partial z})(1 + (\frac{dr}{dz})^2).$$

This is a nonlinear differential equation but because we are under the paraxial approximation dr/dz is small, and the second term of the right part can be approximated to one. For the same reason V, $\partial V/\partial r$, and $\partial V/\partial z$ can be approximated by the first terms of their respective series of the potential distribution equation. Thus

$$V \approx V_0(z), \qquad \frac{\partial V}{\partial r} \approx -V_0''(z)\frac{r}{2}, \qquad \frac{\partial V}{\partial z} \approx V_0'(z).$$

This leads to the final form of the paraxial ray equation:

$$\frac{d^2r}{dz^2} + \frac{dr}{dz}(\frac{V_0'}{2V_0} + \frac{r}{4}\frac{V_0''}{V_0}) = 0.$$

This equation has several interesting features. First, it is independent of the ratio q/m. Second, the derivatives V_0' and V_0'' are normalized with respect to V_0; hence, it is the field distribution and its shape that gives the electron trajectory and not the field intensity. This meaning that the same focusing can be made with scaling down the lenses, which is

very important for miniaturized lenses. And second, the equation is unchanged in form if a scale factor is applied to r; i.e. two beams parallel to the optical axis but not at the same distance from the axis will cross the axis at the same point, thus allowing us to talk about electron lenses. In reality, this last point is an artifact that arise from the limited series taken for describing the potential distribution, and if extra terms are added, various aberrations of these lenses are revealed.

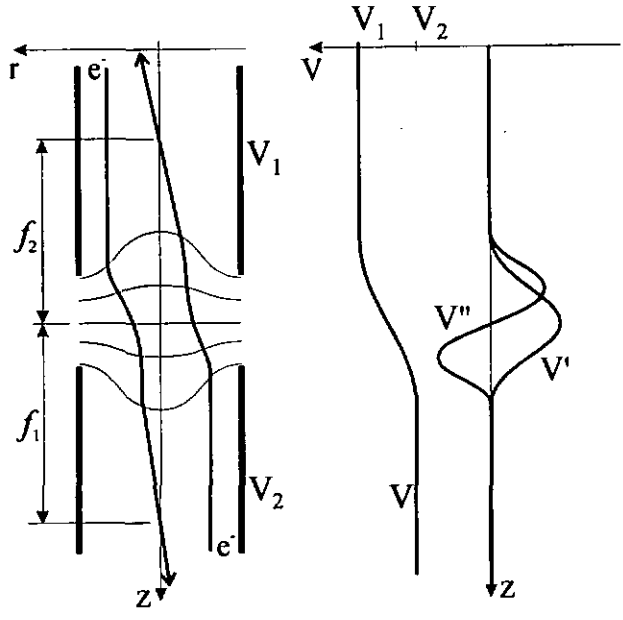

Figure 3.3: Electron trajectory, potential distribution, and their first and second derivatives, in an electrostatic lens formed by two cylinders at different potentials and separated by a small gap.

The lenses have a convergent region where, the axial potential curves concavely upward, and a divergent region, where the potential curves concavely downward; but the global

effect is convergent. To explain the converging nature of electron lens, figure 3.3 illustrate the simple case of two element lens. The electrons going through the first part of the lens (convergent) find potential lines which have a higger longitudinal component than in the second region (divergent), since the focusing effect of the convergent part bring electroos closer to the lens axis, and because they are closer to the axis they find potential lines which have a lower longitudinal component, they will be less deflected in the divergent part.

However depending of the electron path (from the higher potential to the lower, or inversely) a different focal length is found. This is due to the accelerating or decelerating effect of such bipotential lens. An electron coming from a high potential area is slowed down when arriving into the lens, hence it has a lower velocity in the divergent area than in the convergent one. As a consequence, the divergent effect will be larger since the electron flying time in the divergent area is larger than in the convergent area, leading to a lower global focusing effect and a bigger focal length. The same argumentation can be give for an electron coming from a low potential area to a high one; in this case the electron is accelerated, and its flying time will be larger in the convergent area compare to the divergent area, hence the global focusing effect is larger, and the focal length smaller.

If the potential distribution is known then the two focal length of the lens can be calculated from the paraxial ray equation. In the example of figure 3.3, the following relation can be found:

$$\frac{f_1}{f_2} = -\frac{\sqrt{V_2}}{\sqrt{V_1}},$$

where f_1 and f_2 are the focal length for a beam coming from the top and from the bottom respectively. This is similar to the law in light optics for a lens of two different media. The magnification of the lens M is in this case is:

$$M = \frac{f_1}{f_2}\frac{L_2}{L_1} = \frac{\sqrt{V_2}}{\sqrt{V_1}}\frac{L_2}{L_1},$$

where L_1 and L_2 are the object and image distances to the lens, respectively.

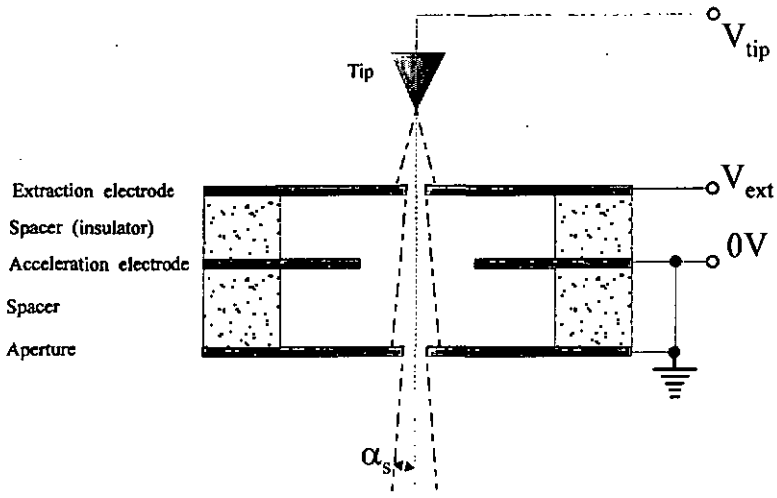

Figure 3.4: Basic microsource configuration.

The configuration of the gun is shown in figure 3.4. It consists of three electrodes; (1) the extraction electrode where a potential is applied to allow a field emission of electrons, (2) the accelerating electrode, to give to the electrons the desired energy, and (3) an aperture to limit the diameter of the beam. We can talk about a source lens because during the extraction-accelerating process, there is also a focusing effect. Typically, the source tip will operate at a distance to the extraction electrode of 20 μm. This present a compromise between the efficiency of the extraction and the electric non-desired field deformation, due to the roughness and the cleanness of the extraction electrode, which must be kept low in order to avoid beam aberrations. The energy of the electrons is defined by the applied voltage between the tip and the acceleration electrode. But the accelerating electrode can also play the role of a retarding electrode (deceleration) if the voltage between the tip and first electrode is too high and to have the right electrons

energy (100 eV in our case) they need to be decelerate. The aperture, since it is placed in a field free region, is chiefly a limitation of the emission angle provided by the source, will define the electron beam current of the microcolumn which is:

$$I = \pi \alpha_0^2 \frac{dI}{d\Omega_0},$$

where α_0 is the semiconvergent angle at the exit of the source and $dI/d\Omega_0$ is the characteristic angular emission density. It is clear that for having the maximum beam current, the semiconvergent angle should be as high as possible.

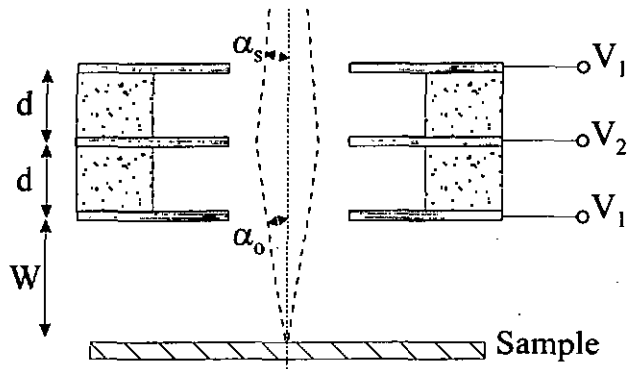

Figure 3.5: Basic micro-objective lens configuration.

The configuration of the objective lens is given in figure 3.5, which is in this case an Einzel lens, while both external electrode have the same potential. It consists of three electrodes, each with generally the same bore diameter and the same spacing. Its goal is to focus the electron beam on the sample surface. If the voltages of the two external electrodes are at the same voltage with the same distance from the central electrode and the same bore diameter, it is a symmetrical Einzel lens, and its focal length can be evaluated as [68]:

$$\frac{1}{f} \approx \frac{3}{8d}(\frac{V_2 - V_1}{V_1})^2, \qquad \text{if} \quad \frac{|V_2 - V_1|}{V_1} \ll 1.$$

This configuration can be used with both $V_1 > V_2$ and $V_2 > V_1$. However with $V_1 > V_2$ there are fewer aberrations. Different external potentials can be also applied; in this case, the lens has an additional retarding or accelerating effect. The design of the lens and the voltage combination must be tuned to have the lowest aberrations. For that purpose an optimum semiconvergent angle can be calculated for a given working distance (W).

3.4 Deflection System

To be able to scan an area of the sample surface, the electron beam must be deflected. The system performing a deflection in one direction, can be just two plates where an opposite voltage is applied, as shown in figure 3.6.

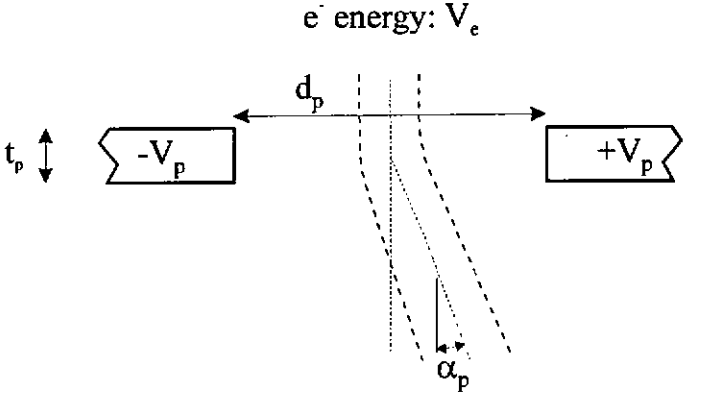

Figure 3.6: The deflection of electrons by two electrostatic plates with opposite potential.

In this case, the deflected angle is:

$$\tan \alpha_p = \frac{t_p V_p}{d_p V_e},$$

which is approximately α_p at small angles. For high energy electrons, the length of the plate must be large, since their high velocity decreases the flying time in the electric field area, and the deflection efficiency will be decreased. But in our case, with low energy electron, this length can be small (typically in the 100 μm range). This fact will help us to integrate the deflector.

The deflection of the beam is done by applying a symmetrical potential between the poles in both sides of the deflection plane as shown in figure 3.7a. There is also a focusing effect during the deflection, since the electrons closest to the positive electrodes will move faster and will be deflected less. In practice, the deflector has height poles, called an octupole or scanner-stigmator. With this type of deflector one can not only have x-y deflection (which would need only four poles), but also a correction of the beam shape. If there is a misalignment between the different elements in the source, the beam shape will be elliptical distorted(astigmatism). To correct it, an elliptical field will be added (figure 3.7b) to have a orientation-dependent focusing effect which will form a circular beam shape at the sample level.

3.5 Detector

In our experiment, the microcolumn was mainly used in transmission mode. In this mode, a mesh was used as a sample, and by scanning the beam the mesh image was recorded with a channeltron located on the other side of the sample. This technique cannot be used to visualize the front side of the samples, and, since in the microcolumn the space between the sample and the bottom of the objective lens is less than 0.5 mm, such a system or a microchannel plate device cannot be used. The detector device to record

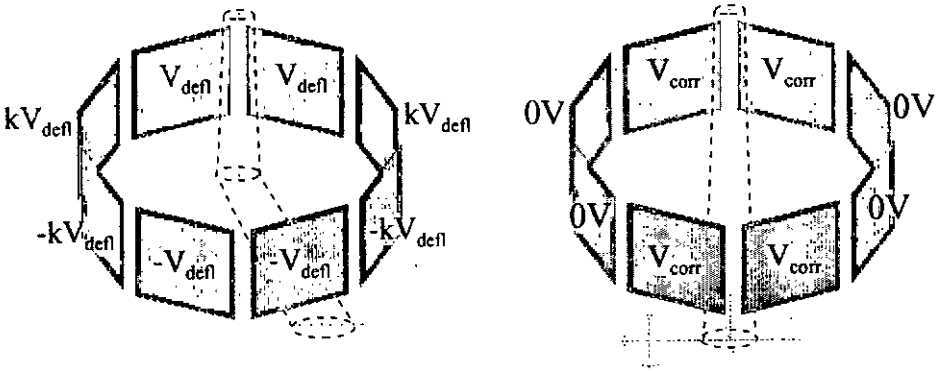

Figure 3.7: The two operating modes of the octupole; a) the deflection, b) the beam astigmatism correction.

the backscattered electrons must therefore be a very compact device with a thickness of less than 0.3 mm. Such a device must also have its sensitive part at the very top of its surface, because backscattered electrons have a very low energy of several electron-volts, resulting in a low penetration depth and because there is no room for an electron accelerator device. Therefore, for 1 keV electron energies, a metal-semiconductor-metal diode (MSM) in silicon [62] or in gallium arsenide [53] has been fabricated and tested successfully. A critical issue for these detectors is the dark current, since such a diode is located at the surface of the chip and no passivation layer can be incorporated (otherwise the diode is buried and will not receive any electrons), the surface leakage current is quite important.

A similar technique can be used for the 100 eV microcolumn, albeit with a lower efficiency, since the number of backscattered electrons is compared to 1 keV, thereby lowering the ratio of signal current to dark current. The challenge would therefore be to

fabricate an integrated electron multiplier.

3.6 Aberrations

The greatest limitation of the beam diameter is imposed by the aberrations of the lenses. That the electrons emission is not monochromatic, the lens fabrication suffers from imperfections, and the electrostatic field produced by the lens does not act as a perfect lens, all lead to an increase of the beam diameter. The real beam size is approximatively the geometrical sum of the beam diameter without aberration and all the confusion disk diameters of each kind of aberration:

$$d^2_{\text{beam}} = d^2_{\text{beam without aberrations}} + \sum d^2_{\text{aberration i}}$$

3.6.1 Spherical aberrations

Since the electric field producing the focusing effect in a lens is not ideally curved; the electrons have a different focal length depending on their radial distance from the optical axis. This defect is caused by a stronger focusing effect near the electrode as shown in figure 3.8.

The disk diameter of confusion at the image crossover, d_s, is

$$d_s = 0.5 C_s \alpha^3,$$

where C_s is the spherical aberration coefficient which is directly proportional to the focal f, and α is the semiconvergent angle in the image space. It is impossible to correct an aberration introduced into a beam by a lens with subsequent beam reshaping. Therefore, it is imperative to have an electrode configuration that produces the most suitable electric field. The equation above shows that d_s can be reduced by limiting the convergent angle. Since the spherical aberration coefficient increases with the focal length, the more efficient

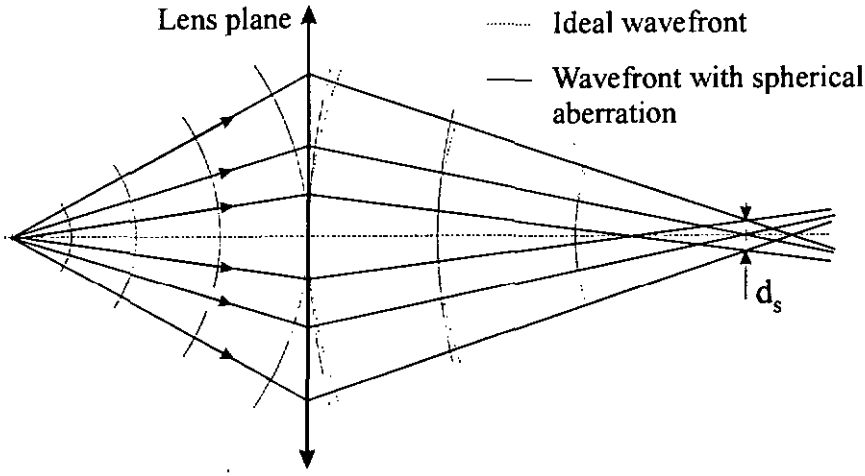

Figure 3.8: Schematic of the spherical aberration induced by a lens.

possibility to reduce the beam convergent angle is to add a limiting aperture, but this will lower the beam current. The optimum will be a trade-off between the spot diameter and the beam current.

3.6.2 Chromatic aberrations

Since, at the emission, the beam have not electrons with all the same energy, their behaviors into the lens will be different depending of their specific energy. A high-energy electron will have a weaker focusing effect than a low-energy electron (see figure 3.9). The term " chromatic" is used analogously with the visible light optic in which photon energy is correlated with the colors of the light and, depending of their color, have a different velocity in the glass media of the lens, producing a different focusing effect of the glass lens.

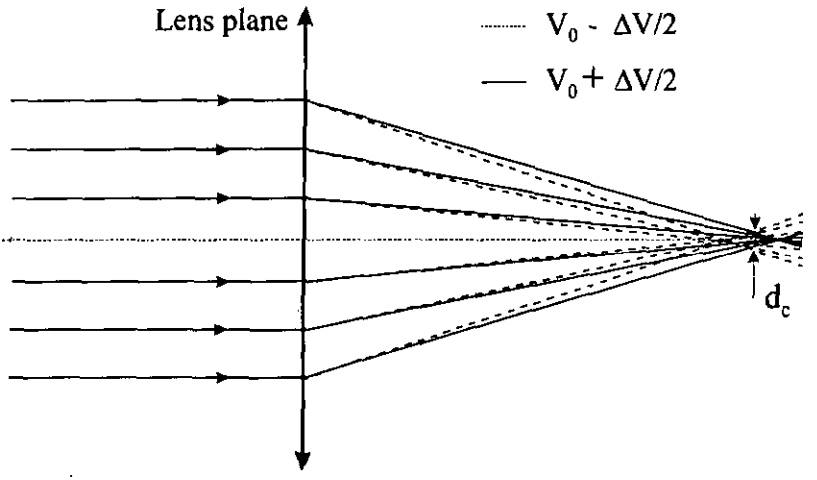

Figure 3.9: Schematic of the chromatic aberration introduced by a lens.

The disk diameter of confusion due to the chromatic aberration, d_c, is

$$d_c = C_c \frac{\Delta V}{V_0} \alpha,$$

where C_c is the chromatic aberration constant, which is also directly proportional to the focal f, ΔV is the energy spread, and V_0 is the mean energy of the beam. For low energies this effect is quite important since this aberration is proportional to the ratio $\Delta V/V_0$, and the energy spread is independent of the mean energy. Hence, for low energies, the electron emission process must keep the energy spread very low (field emission). As with the spherical aberration, reducing the convergent angle will reduce the chromatic aberration, but at a lower rate (linearly instead of to the third power).

The chromatic aberration will occur also in the deflection process during scanning. It will limit the quality of the beam with large deflection.

3.6.3 Astigmatism

Astigmatism occurs when the element of the optic are misaligned with regard to the optical axis. It can he that the electrodes are not perpendicular to the optical axis, or they can be shifted with regard to the optical axis. The result is an elliptical shape of the heam as shown in figure 3.10.

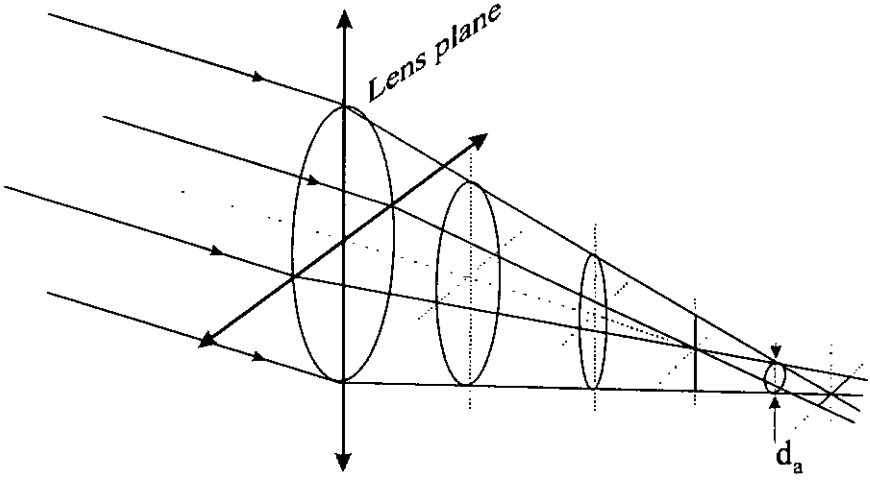

Figure 3.10: Schematic of the astigmatism introduced by a lens.

The minimum disk of confusion d_a is directly proportional to the semiconvergent angle, α, through the astigmatism constant C_a:

$$d_a = C_a \alpha.$$

This imperfection can he corrected by a stigmator as mentioned in the previous chapter.

3.6.4 Diffraction

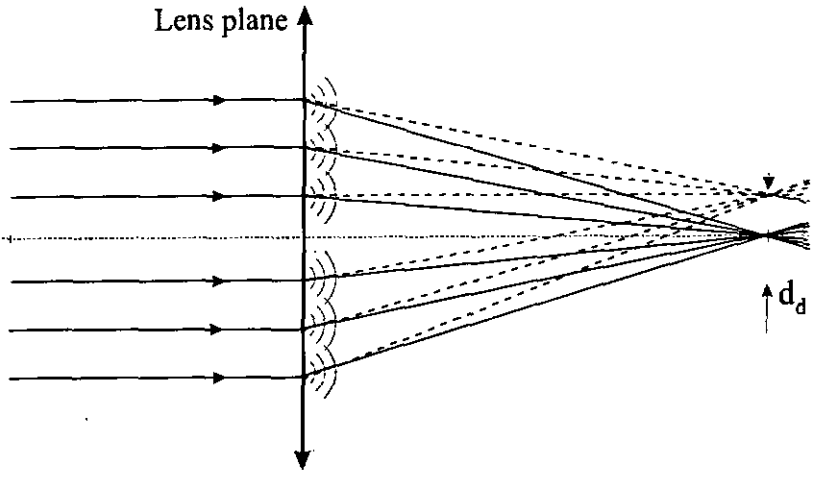

Figure 3.11: Schematic of the diffraction introduced by a lens having a limited aperture.

When the electron beam passes through a limiting aperture, as with a ligbt heam, the beam is diffracted. The spot due to this diffraction (see figure 3.11) is

$$d_d \approx 0.6\frac{\lambda}{\alpha},$$

where λ is tbe de Broglie wavelength of the electrons, which can be approximated with the following expression::

$$\lambda \approx 2.5\frac{1}{\sqrt{V_0}} \quad \text{[nm] with } V_0 \text{ in [eV]} \quad \Longrightarrow d_d \approx 1.5\frac{1}{\sqrt{V_0}\alpha}.$$

Here also, the lowering of electron energy does not improve tbe beam quality. However, contrary to spherical and chromatic aberrations, decreasing the convergent angle by reducing the diameter of the aperture will increase the diffraction rate. We can conclude already that an optimum convergent angle is necessary to minimize the beam diameter.

3.6.5 Electron-electron interactions

In the region where the density of electrons is very high, the electrons are close enough to interact. This leads to an energy broadening (commonly referred to as the Boersch effect) and to a displacement of their trajectories. In the microcolumn this effect is mainly confined to the cathode region [50], where the electron density can he very high and the electrons velocity very low. The consequence is an augmentation of the chromatic aberration of the electron probe. The displacement trajectory occurs mainly in the region before the aperture, after, which the current drops, hence lowering this effect in the rest of the column.

Once again, in the context of electron-electron interactions, working at low energy is not an advantage, hut it can he compensated for hy the miniaturization of the source region.

3.6.6 Lens imperfection aberration

Many other effects can add aberrations and/or increase the aberration coefficients of the above-mentioned cases. The roughness of the electrodes will disturh the electric field in the lens area and can change locally the focalisation effect. The roundness of the electrode creates a rotation asymmetry, which can induce an angle dependence on the focusing rate (astigmatism). This two imperfections must he kept under 1% of the electrode diameter to limit their effect on the field.

The spherical aherration coefficient usually given in the literature is determine within the paraxial approximation. If the dimension of the heam hecomes non-negligible compared to the radius of the electrodes, the coefficients will he higher. This is illustrated by the following relation, which has been determined experimentally [68],

$$C_s \propto \frac{f^3}{R^2},$$

where f is the focal length and R the radius of the electrode.

A misalignment between electrodes is also a source of deterioration of the beam quality because it introduces coma into the beam [50].

3.7 Microcolumn design rules

Lens aberrations occur in both source and objective lenses, but their proportion and amplitudes are different. Figure 3.12 illustrates and gives a global view of the microcolumn, and highlights the areas where problems that decrease its performance, are generated.

The first improvement of the miniaturization and the piezo alignment stage for positioning the tip is that the distance between the tip and the extraction electrode can be kept very small (between 20 and 50 μm). Therefore the extraction voltage for a given extraction current will be significantly lowered compared to that of a conventional source. This is quite important because the lifetime of tips is usually limited by erosion due to ion impact generated by high-energy electrons hitting the extraction electrodes and dispelling ions from the electrode. Due to the electric field these ions will be accelerated back to the tip and mill it. This precise positioning also allows one to reduce the diameter of the extraction electrode to 1 μm, which is a limit given by the quality of its fabrication. Since aberrations scale with the lens size [66], this important downscaling will reduce significantly the lens aberrations of the extraction electrode. Another advantage, is that many aberrations with low-energy electron beams are expected to come from the extraction area [31] because this region has a very high field gradient, which will strongly affect electrons with low velocity. By shortening this area, the mean flying time of electrons can be reduced and hence the global effect on them as well. The energy spread due to electron-electron interaction can also be reduced by shortening the distance between the tip and the first electrode, and the trajectory displacement of the electron due to this

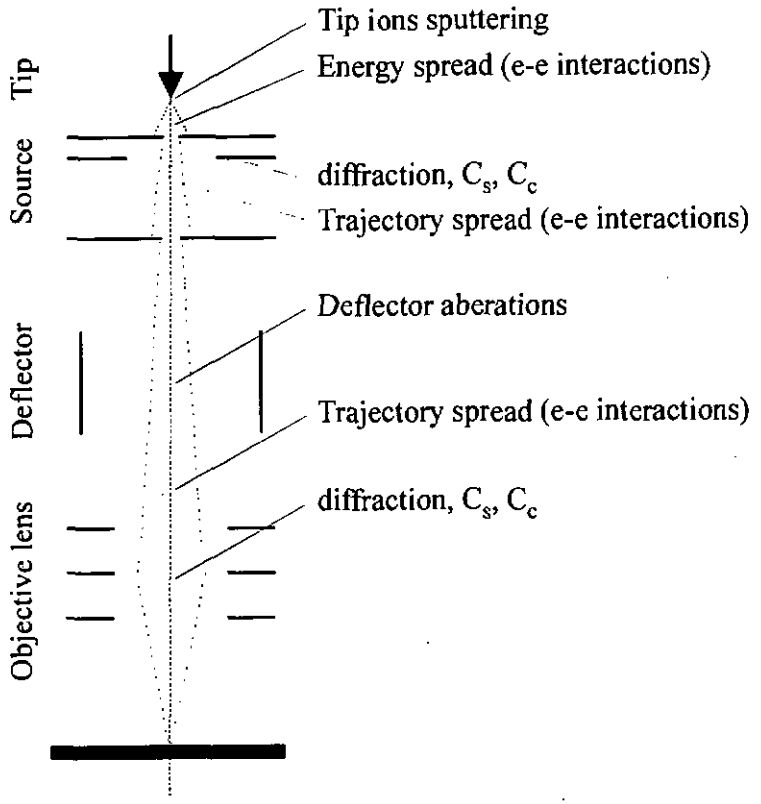

Figure 3.12: Overview of the weak points in the microcolumn which decrease its performance.

same effect can also be reduced by decreasing the source lens thickness.

To estimate the electron-electron interaction in the different regions of the microcolumn having different electronic currents, the number of electrons simultaneously in the parts of the column and the mean distance between them must be calculated. The number of electrons n is given by

$$n = \frac{It}{q}$$

with I the electronic current, t the flying time for electrons to go through the column part, and q the electron charge (1.6×10^{-19} [C]). The velocity v of electrons having energy E is

$$v = \sqrt{\frac{2qE}{m}}$$

with m the electron mass (9.11×10^{-31} [kg]). Since the flying time can he replaced hy $t = l/v$, where l is the length of the column part, the number of electrons is

$$\mathrm{n} = \frac{Il}{q}\sqrt{\frac{m}{2qE}}.$$

But the interaction hetween two electrons is also proportional to, first, the repulsion force F hetween two electrons, which is inversely proportional to the square of the electron distance, r. This electron-to-electron distance can he evaluated by a mean value equal to l/n. Second, it is proportional to the time t the electron stays in such an environment. Hence an electron-to-electron interaction factor k, valid if $n > 1$, can he calculated:

$$k = \frac{1}{r^2}t = \left(\frac{n}{l}\right)^2 \frac{l}{v} = \frac{I^2 l}{q^2}\left(\frac{m}{2qE}\right)^{3/2} \quad \text{if} \quad n > 1\,,$$

$$k = 0 \quad \text{if} \quad n \leq 1\,.$$

It shows that this effect will be proportional to the square of the current and it is linear with the length of the area. To get an idea of the electron-electron interaction for the three parts given above, considering that in the tip-extraction electrode area the current is typically 5 μA and represents a distance of about 50 μm, in the extraction electrode-aperture area the typical current is 3 nA and 500 μm long, and in the aperture-sample area the current is 500 pA and 3 mm long. Taking an electron energy of 100 eV in the three parts, we have:

1. In the tip-extraction electrode area: $n = 265$ electrons, and $k = 235$.

2. In the extraction electrode-aperture area: $n = 1.6$ electrons, and $k = 0.0005$.

3. In the aperture-sample area: $n = 1.6$ electrons, and $k = 0.00008$.

The k value in the tip-extraction electrode area is seven orders of magnitude greater than in the rest of the column. Even if this is just an approximation, it is clear that the main electron-electron interaction problem will be between the tip and the extraction electrode. This is perfectly illustrated by the simulation done by Thomson [72]. He calculated that for a field emission source, which at 300 K has an energy spread of 0.25 eV when the extraction current is low, the energy spread can increase up to 0.4 eV for an angular density of around 10 μA/sr under operating conditions relatively similar to those that yielded above. Nevertheless keeping the column length as small as possible will always be better in view of the electron-electron interaction.

But working with low-energy electrons also has advantages regarding to the aberration problem. It allows, for the same focusing effect, to reduce the applied voltage and thus the lens dimension to be reduced (less aberration). The limitation of this downscaling is first the breakdown voltage in vacuum ($V_B \sim 10$ V/μm), and second that the beam diameter in the lens area must be much smaller than the bore diameter (in general the beam diameter is kept less than 10% of the bore diameter) to avoid an excessive spherical aberration coefficient ($C_s \propto$ (bore diameter)$^{-2}$). The beam diameter into the objective lens depends on the distance between the virtual source and the objective lens and on its emission angle. The emission angle is imposed by the given required current; again the improvement of the objective lens quality, depends on our ability to minimize the column length.

For the first electrode of the source lens, the beam is as large as the electrode bore, and considerable aberration will be generated by the non-paraxial part of the beam. Hence the source aperture is necessary to cut the edge of the beam where the aberrations are

the largest.

The second part of the source lens is not reduce as much as the first part, because the breakdown voltage in the vacuum (10 V/μm) does not allow such a high downscaling. If the accelerating electrode also acts as a lens; because its goal is only to accelerate or to decelerate the electrons, its focusing effect can be kept small. Hence, its position and diameter is not that critical compare to the first part and th size limitation due to the vacuum breakdown voltage will not be a significant restriction of the source quality. Reducing drastically the dimension of the first part of the source lens and less drastically the second part is the selective downscaling approach developed by T.H.P. Chang's team [20, 48]. As a result, they show that the source brightness for low-energy beams can be increased by at least two orders of magnitude.

Now that the various generations of beam distortion have been revealed and the means to reduce them have been given, their effects on the brightness, which depend on the ratio between the electron probe current and its diameter, must be evaluated. Figure 3.13, show a decomposition of the microcolumn into two parts, which will help us to differentiate the parameters related to the source from those related to the objective lens. The current is determined by the source, which is given by

$$I_2 = I_1 = \pi \alpha_0^2 \frac{dI}{d\Omega_0} \quad \text{if } \alpha_0 \text{ is small},$$

where I_1 and I_2 are the beam current after the source and at the sample level, respectively, α_0 the semiconvergent emitting angle of the source given by the aperture, and $dI/d\Omega_0$ the angular emission density of the gun. To find the diameter of probe size d_2, the optimum semiconvergent angle α_2 must be found with regard to a minimum of the aberrations:

$$d_2 = ((M_2 d_1)^2 + d_{d2}^2 + d_{C,2}^2 + d_{C,2}^2)^{1/2}$$

where $M_2 = \alpha_1/\alpha_2$ (if α is small) is the magnification of the objective lens, d_1 the source diameter given by the gun (tip and source lens), and d_{i2} the different disks of confusion

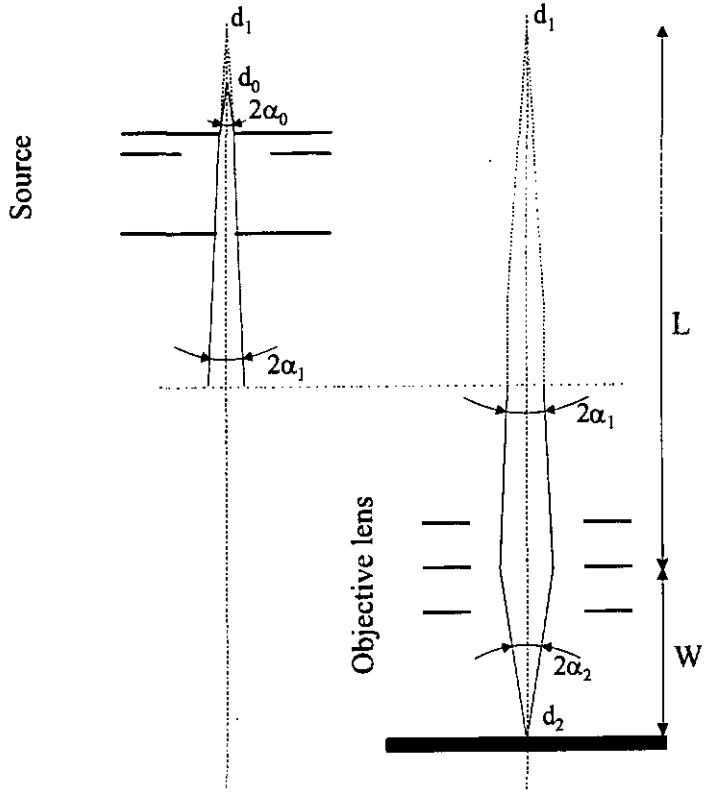

Figure 3.13: Decomposition of the microcolumn into two parts, the source and the focalisation part, in order to determine the electron probe brightness.

of the principal aberration of the objective lens (spherical, chromatic, and diffraction).

The value of d_1 depends, first, on the virtual size of the tip d_0 multiplied by the magnification factor of the lens formed by the source lens effect M_1 and, second, on its aberration

$$d_1 = ((M_1 d_0)^2 + d_{d1}^2 + d_{C_s 1}^2 + d_{C_c 1}^2)^{1/2} .$$

If we assume that the a focusing effect of the source is kept low, to minimize the aberration coefficient due to the focusing effect: we have $\alpha_1 \sim \alpha_0$, $d_1 \sim d_0$, and the absolute value of M_1 is equal to 1.

If we take again the equation for d_2, with d_1 fixed by the source quality which was optimized by limiting its focusing effect and by its miniaturization; this results in

$$d_2 = \left(\left(\frac{\alpha_0}{\alpha_2} d_1 \right)^2 + \frac{1.5}{\alpha_2} \sqrt{V_2} + 0.25 C_{s2} \alpha_2^3 + C_{c2} \alpha_2 \frac{\Delta V}{V_2} \right)^{1/2},$$

and the optimum α_2 minimizing d_2 is given by

$$\frac{\partial d_2}{\partial \alpha_2} = 0.$$

The α_2 optimum is dependent on the working distance, so a mere geometrical consideration yields

$$\alpha_2 = \frac{\frac{\alpha_1}{L}}{W} = \alpha_0 \frac{L}{W}.$$

Hence, with α_0 given by the current required and W given by the working distance, an optimum column length can be found to minimize the beam diameter d_2. Unfortunately we were not equipped with a simulation program to optimize the microcolumn taking all the appropriate parameters into account. But from the calculation done by the Chang team for an energy of 200 eV, a working distance of 1 mm, and a beam current of 1 nA, the optimum length of the column is in the range of 1 mm, and the smallest beam diameter achievable is 16 nm [31]. For 100 eV the optimum would be for an even shorter column length, but such a small length cannot be achieved with our actual. Nevertheless it gives a global information on the way in which the lens and microcolumn development should progress.

Other improvements and optimization can be performed. As an example, using an asymmetric objective lens (neither the diameter of the bores nor spacing are all the same dimension) [50]. Since we did not have the optimum length for low-energy electrons (our

microcolumn is too long), a configuration in which the beam energy is higher in the column and slows down just before landing (retarding mode) into the objective lens can be used.

All these considerations are valid for an on-axis beam, but optimization of the beam diameter during deflection is also desirable. For example a pre-objective lens double deflection system offers a significant improvement during scanning. In the other hand such a system must be kept very short for the above-mentioned considerations. Another possibility is an integrated deflection system in the objective lens to perform a moving lens concept with vertical landing can result in a significant improvement during deflection [50].

All these techniques are possible, but a trade-off must be made between maximizing the microcolumn quality and minimizing its complexity.

Chapter 4

Arrays of source lenses fabricated with silicon membranes and Pyrex spacer

This chapter describes the fabrication and testing of arrays of source lens made of silicon membranes for the electrodes and Pyrex for the insulator spacer.

4.1 Design and fabrication

The fabrication of source lenses using silicon membranes as electrodes and a Pyrex spacer plate as insulator was pioneered by Chang's group [43]. But their process is not well suited for batch fabrication of lenses. Their approach, consists of fabricating the electrodes separately, and then assembling and aligning them under a microscope with micromanipulators, the bonding being done anodically. In our first fabrication schemas, the same materials were used. Other possibilities where investigated such as using a Polyimide spacer which can be spun to a layer thickness of several tens of micrometer and is UHV compatible, or using an evaporated layer of metal for the electrode. But because we were

not working with large samples or wafers, it proved too difficult to spin an homogeneous Polyimide layer on the sample. Also, patterning a high quality hole in a metal layer (by etching or by plating) was found to be difficult.

4.1.1 Choice of materials and design

The choice of using silicon membranes and Pyrex as the base materials to fabricate the source lens is motivated by the following points:

1. Monocrystallin silicon membranes are mechanically very stable which is desirable since they will be subject to electrostatic forces during operation and, at a lot of manipulation during fabrication and mounting in the test device.

2. These membranes are fabricated using a highly boron doped etch stop technique [73]; hence, they have a good electrical conductivity. This is especially important for the first electrode which intercepts the biggest part of the extracted current (up to 10 μA).

3. Monocrystallin silicon is a very often used material in micromachined devices, and very high quality machining techniques are commonly available for it. Since for the lens bores, the quality of the fabrication is really crucial, such techniques will be invaluable.

4. Pyrex is of course a good dielectric material (its breakdown voltage is higher than that of vacuum). But its most helpful characteristic is the possibility of bonding it with silicon by anodic bonding. This technique has the advantages of being low temperature (below 450 °C), Ultra High Vacuum (UHV) compatible, and simple to perform. Also, Pyrex has a thermal expansion coefficient α well matched to silicon ($\alpha_{Pyrex} = 2.9 \times 10^{-6}$ K^{-1}, $\alpha_{silicon} = 2.6 \times 10^{-6}$ K^{-1}) [74], thus avoiding stress in the final structure after cooling.

If lens array or lens batch processing is to be done, a process must be developed able not only producing fine bores in the electrodes, but also of having a high alignment accuracy of the bores forming a lens, and this for each lenses of the wafer or chip. This is especially true for the objective lens where misalignments introduce coma aberrations, but is also desirable for the source lens. Figure 4.1 shows the configuration of a source chip containing only one lens.

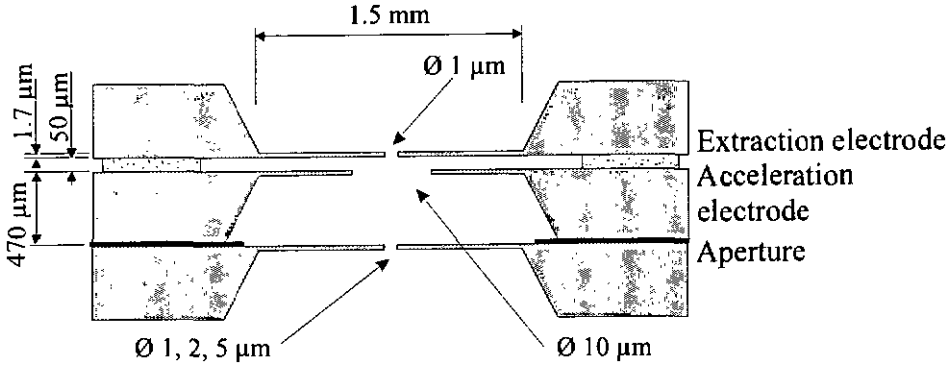

Figure 4.1: Basic source lens configuration.

The thickness of the electrode membranes is 1.7 μm, making them stable enough even with a lateral size of 1.5 x 1.5 mm. The Pyrex spacer is 50 μm thick; while for low energy electrons, such a thick inter-electrode space is not needed, this is about the minimum of what we were able to polish down and to manipulate safely. The space between the accelerating electrode and the aperture is 470 μm. To avoid electron trajectory spreading due to the electron-electron interaction in this region where a high electrons density will be, it would be preferable to minimize this distance (with a smaller aperture) However, it is constrained in practice to the thickness of the wafer. The bore in the first electrode has a diameter of 1 μm, which is, according to down-scaling theory, suitable to provide a

high-brightness low energy source, and simultaneously does not challenge the machining limitations so that high quality hole pattern can be achieved. The acceleration bore is 10 μm in diameter. The aperture has a diameter of 1, 2, or 5 μm depending of the lens in the array. Hence, different beam sizes can be tested.

4.1.2 The process

The source lenses chip fabricated is an array of seven lenses placed as a 3×3 matrix shown in figure 4.2, with a top-view picture of the first electrodes and a one-lens details after fabrication. Two prealignment crosses occupy two corners of the array, while the seven other positions are the actual source lenses. Each one consists of a 1 μm diameter hole, with four triangular shapes used to have an optical feedback of the bore position during the alignment of the tip, and four crosses used for the electrode alignment procedure. Note that around the hore nothing is patterned to avoid forming parasitic electron beam that might interfere with the primary beam. A safety distance of 50 μm is used to prevent this.

Membrane fabrication

Membranes are made by wet etching, using a highly boron doped etch stop technique [73] and ethylenediamine-pyrocatechol (EDP)-based as an anisotropic silicon etchant [75]. This technique is commonly used to fabricated silicon membranes as a support for X-ray masks. Although this etch stop technique also works with the more commonly used potassium hydroxide (KOH) or tetramethethyl ammonium hydroxide (TMAH) based anisotropic etchant, these do not give the same etch stop quality. With EDP, etch rate selectivity of up to 10^4 is achievable at a dopant concentration of 7×10^{19} cm^{-3}, which decreases the timing accuracy necessary to achieve a given membrane thickness. The highly doped layer is 1.7 μm thick and grown by a chemical vapor deposition (CVD) epitaxial

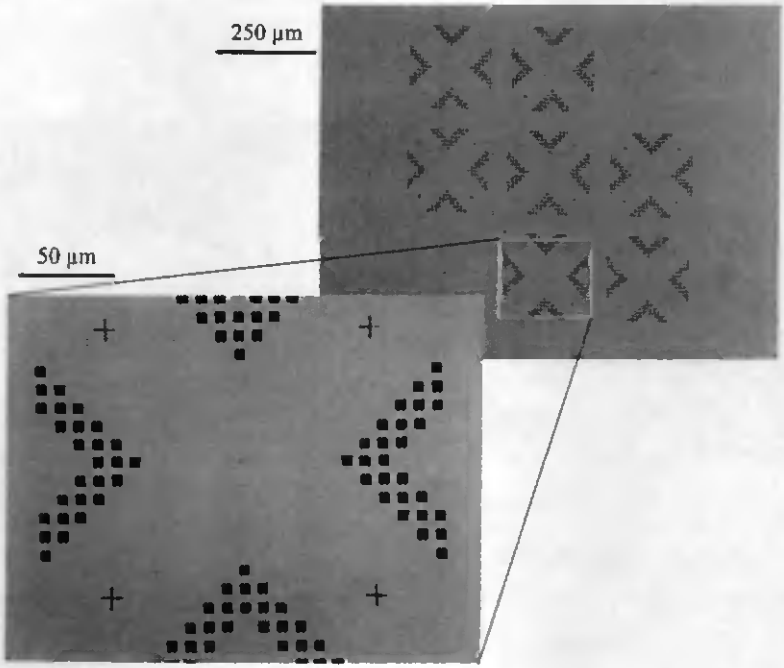

Figure 4.2: Picture showing the first electrode of the source lens array, and a close-up view of one component of the array, with the optical alignment marks, the electrode alignments marks, and the 1 μm hore.

technique [76]. Epitaxy was preferred over implantation/diffusion techniques because, during implantation, the channeling of boron ions in the silicon crystal results in a non homogeneous doping profile [77]. This in turn results in an insufficiently backside of the silicon membrane after etching. This difference between epitaxy and diffusion membrane material is clearly visible in figure 4.3, where the back side of both types of membrane is shown near a 1 μm micromachined hole. The ion channeling effect leaves a corrugated texture on the surface, which is not desirable for lens electrodes because it can disturb

the electric field and, for the first electrode, a smooth surface is essential for the optical tip alignment (mirror effect).

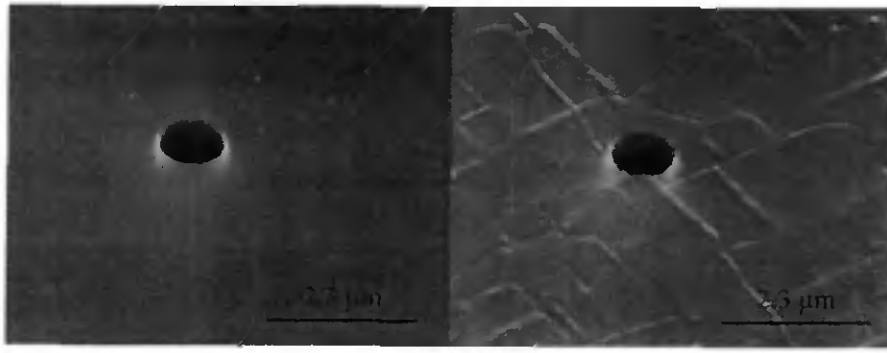

Figure 4.3: SEM pictures of two membrane back-sides made from two different boron doped layers. One was made by epitaxy (left), and shows a very smooth surface. The second was made by boron implantation and diffusion, and shows a roughness of the surface due to the channeling effect during the implantation (right). In both membranes a 1 μm hole was etched as a size reference.

Bore fabrication

Bore patterning requires a very high definition. High quality e-beam lithography was used with a deflection system carefully calibrated to have exactly the same deflection in x and in y directions in order to achieve the required roundness of better than 1 %. Masking is done using a 500–nm-thick layer of Plasma Enhancement Chemical Vapor Deposition (PECVD) silicon oxide nitride (SiON), and the pattern imaging layer is 500 nm of KRS, a high performance IBM e–beam resist [78]. The relative proportion of oxygen and nitride in the SiON film can be tuned to zero stress induce by the film on the membrane, and

hence, deformatioo and even cracks are avoided. The SiON deposition was found to be stress-free at a refractive index of 1.554.

The pattero delineated io the KRS is transferred iato the SiON by reactive ion etching (RIE) using a standard CHF_3/O_2 process (flow rate for CHF_3 of 50 sccm and for O_2 of 2.5 sccm, RF density of 0.16 W/cm^2, and pressure of 50 μbar). After stripping the remaining resist in an oxygen asher, the SiON pattern is transferred into the silicon membrane by RIE with an Ar/Cl_2 mixture (total flow rate 35 sccm, 14 % of Cl_2, RF power density of 0.16 W/cm^2, and pressure of 20 μbar). Finally, the SiON film is removed by a buffered hydrofluoridric acid (BHF). Figure 4.4 shows a 1 μm electrode bore machined in a 1.7-μm-thick silicon membrane, with very small edge roughness (about 10 nm) aod very vertical side walls.

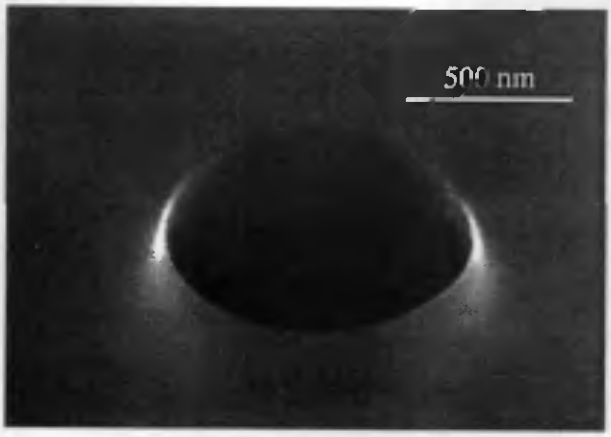

Figure 4.4: 1 μm lens bore fabricated io a silicon membrane with very vertical side walls and a roughness of less than 10 nm.

Silicon membrane/Pyrex spacer/silicon membrane stack fabrication.

Anodic bonding was used to assemble the silicon membrane/Pyrex spacer/silicon membrane stack. To avoid charging effect on the Pyrex surface, no insulator material must be around the optical axis area. Hence, the Pyrex spacer is made out of two bars positioned to have a large opening between them. In addition, this configuration facilitates the out-gassing of the microlenses in the UHV environment tremendously and makes the operation of the microcolumn more reliable.

This bond must be mechanically stable enough to withstand normal handling and further chemical etching processes which can occur during the lens fabrication. Whereas the anodic bonding of silicon to Pyrex at a single interface is well known [79], performing such a strong bond on both sides of a thin Pyrex plate is not that easy. The first experiments we performed, consisted of bonding one interface after the other using the silicon chips as contacts. We found great difficulties in obtaining an adequate second bond even with perfectly controlled parameters (of voltage, temperature, time, etc). We explain this fact as follows: during the first bonding, the Pyrex near the bonded interface is densified and completely depleted of the sodium ions (Na^+) which drift towards the Pyrex-side contact. This zone is then no longer a medium permeable to ion-diffusion current because of the densification. As a consequence, the second bond will be incomplete. This is illustrated in figure 4.5, where the current during the first and the second bonding of a silicon-Pyrex-silicon stack are shown. It is clear that the total charge, which is proportional to the area under the curve, provided to the bond is much higher for the first bond than for the second one. The way around this problem is to control the first bond formation to be good enough to be mechanically stable, but "bad" enough to allow an ionic current in the Pyrex. In practice, the depleted zone at the first bond interface should be kept thin, or not done in the whole area, so that a current can be generated for the second bond.

For this purpose we developed an AC anodic bonding technique [80]. This new ap-

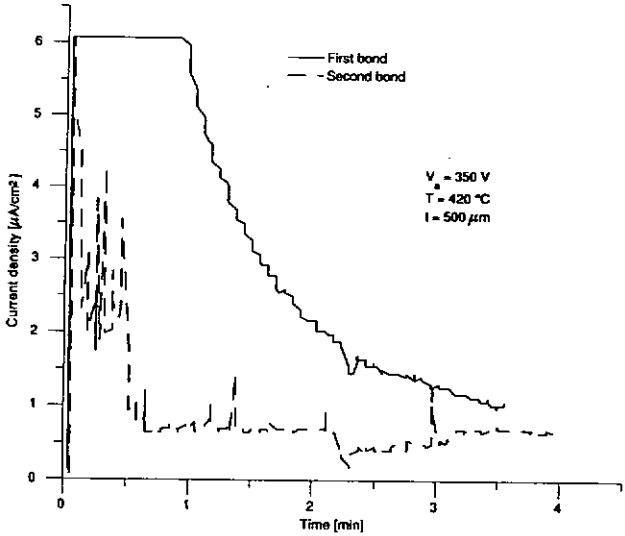

Figure 4.5: Current peak during the first bond (solid line) and during the second (dotted line) of a double-sided bond formed sequentially .

proach relies on square-wave bonding voltage which leads to a simultaneous bonding of both interfaces. The depletion layers are formed and alternately widened on both sides of the glass. To be sure that both bonds start at the same time, the right frequency must be found. Since this frequency varies a lot depending of the bond configuration, a sweep from high frequency to low frequency is applied. At high frequencies, the bond does not have the time to form. When the frequency starts to be in the range of the time constant of the anodic bonding process, the two bonds will be initiated. First this formation will be "soft", while the frequency does not allow the generation of a lot of charge, but as the frequency is decreased the waveform phase periods will increase, slowly strengthening the bonds, until the process stops. Figure 4.6 shows the setup for the AC anodic bonding.

The frequency is swept from 10 to 0.005 Hz over 15 min. A first order, low-pass filter with a cut-off frequency of 2.5 Hz is added, with the purpose of smoothing the amplitude increase around the frequency where bonding starts. The chosen frequency range is relatively wide, to ensure independence of parameter modification. To monitor bond formation, the current integration during the positive and negative waveform phases are evaluated to determine the bond quality, since we have no means to inspect the propagation visually as we would for a single-face bond trough the Pyrex. The voltage used is 350 V and the temperature 420 °C.

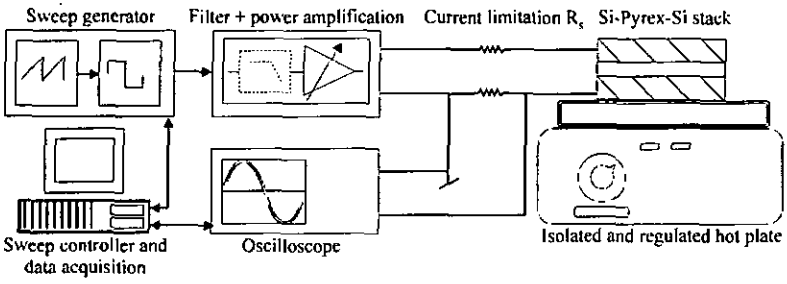

Figure 4.6: Setup for AC anodic bonding.

In a comparative test between a DC single-sided bond and an AC double-sided bond, the mechanical and chemical strengths were checked. No significant difference was measured between the two techniques; a shear force between 1 and 2 MPa was applied before rupture in both cases, and both structures could withstand more than 3 hours in a BHF (7:1) bath. For comparison, a double-sided DC bond shows a shear force rupture lower than 0.5 MPa and cannot withstand more than 30 min in a BHF bath.

Bores alignment

In order to achieve precise alignment between the lens bores for each lens in an array, we develop a technique consisting of fabricating the lenses chip layer by layer. The bore pattern in the first electrode is machined first, and provides reference marks for aligning the two other electrodes. This idea is presented in figure 4.7. After the fabrication of the first electrode and its assembly with the Pyrex and the second electrode, reference mark openings in the first electrode are used as a shadow mask to e–beam expose a resist spun on the back side of the second membrane.

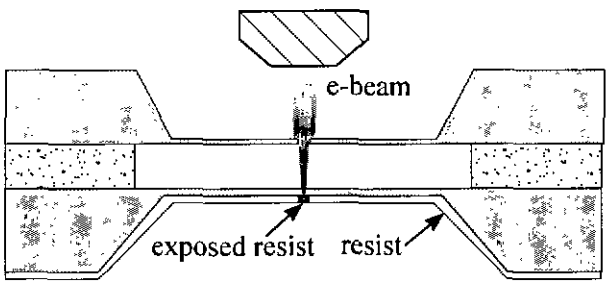

Figure 4.7: Schematic of the trough-membrane alignment, where a reference mark in the first electrode is transferred by e–beam exposure into the resist spun on the back side of the second electrode.

For this process, two techniques must be tightly controlled: the exposure trough a membrane, and the spinning of a resist into the window of the membrane. Since the lenses were fabricated individually while developing this process, the resist deposition was done by spinning with the membrane centered with the spinner axis. In this way an adequately homogeneous resist layer was obtained. For batch processing this is of course not possible, but other techniques can be used, such as resist spray coating and resist electrodepositionning [81].

Exposure through a membrane is possible using an e-beam because, first, the electron penetration depth in the material is relatively high and having an electrons penetration of several micrometers at an electron energy of several tens of kiloelectronvolts is perfectly feasible (see chapter 2), and second the depth of focus of the e–beam system used is large enough to ensure relatively small projected image on the second electrode, even though it is not possible to focus on it accurately. The electron energy must be chosen high enough to allow electrons to go through one membrane but not two, otherwise the first electrode will not play its role as a mask. The quality of such an exposure is mainly limited by the electrons scattering in the membrane. Figure 4.8 shows two examples demonstrating the feasibility and the resolution limits of an exposure trough a 2 μm-thick silicon membrane. It was done at an e-beam energy of 35 kV. The first exposed pattern consists of the two words "Back Side", and after development of the resist the mirror version can be read. The second shows the quality limitation of such an exposure due to electron scattering into the membrane; a 1 μm square exposed pattern results in a 1.3 μm circular shape in the resist, with a sidewall roughness of about 50 nm. Nevertheless the quality of such a mark is adequate for use it as a reference for the second electrode.

To achieved high accuracy, the lithography through the membrane must be characterized (in terms of exposure dose, electron energy, and development time) for a given resist layer thickness. In our application, where the bore fabrication process require a double mask layer of SiON and resist, the lithography must be characterized for a composite membrane consisting of a 1.7 μm silicon layer, 500 nm of SiON, and 500 nm of resist. Figure 4.9 shows a characterization sample. The experiment consisted in leaving the electron beam in one place during various times and at various energies. It shows how the forward scattering effect can spread the electrons in dependence of the energy and the dose, and hence, expose the resist at a distance from the point of impact of the beam. The inner circle visible for energies larger than 12 kV is due to reversal of the

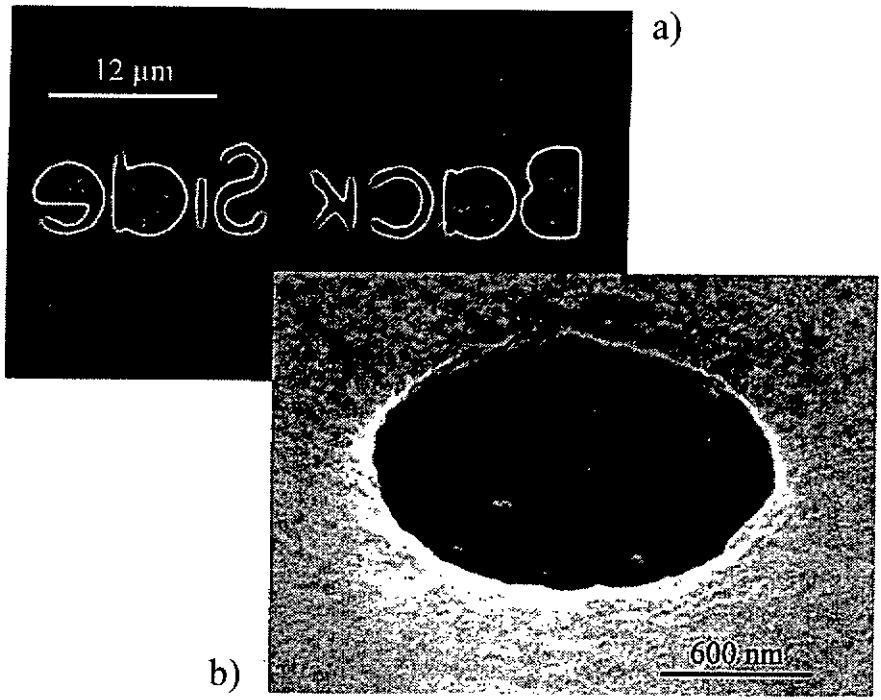

Figure 4.8: SEM pictures demonstrating the feasibility of the exposure trough a membrane. a) The two words "Back Side" were patterned from the other side of the supporting membrane. b) Due to the scattering of the electrons, the pattern is distorted. Here a 1 μm square was patterned, resulting in a 1.3 μm circular shape.

resist. Polymers which are broken by electrons in this positive resist are relinked when the dose is too high (i.e. it act as a negative resist).

To do the exposure trough the shadow mask, the e-beam is raster-scanned over an area overlapping with the reference mark openings in the first electrode (the marks typically have a feature size in the 700 nm range). The beam is scanned at a relatively high

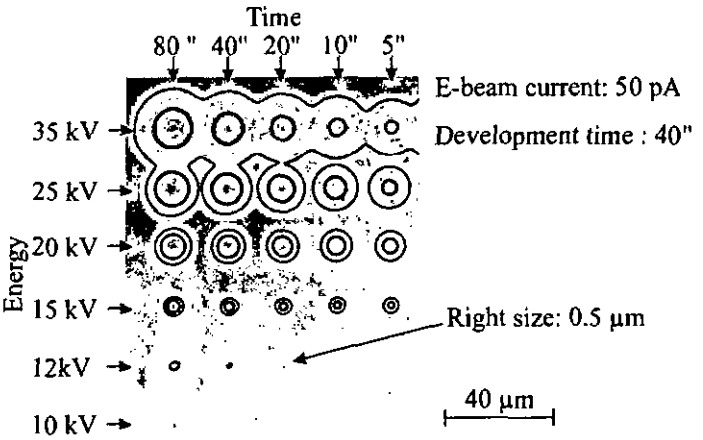

Figure 4.9: Exposure trough a membrane, with different energy and different dwell time.

magnification (writing field $\approx 1.5\mu$m) so that the deflecting angle is small enough to affect the alignment accuracy. Another consideration is that the electron current may not be too high, as the exposure time must be kept large compared to the couple of second necessary to center the alignment mark openings with respect to the scanned area. The exposure time will also increase with the ratio between the scanning area and the opening area in the shadow mask. From figure 4.8, and given that the ratio between the scanning area and the opening area in the first electrode is about 2:1, we choose an exposure time of 30 sec, an electron beam energy of 12 kV, and a development time of 45 sec.

Another issue during the electrode alignment is the tilt between the e-beam axis and the axis of the future source lens. A misalignment of 0.1 deg when the two electrodes are separated by 50 μm produces a shift error in the alignment mark position of 100 nm. In practice, the lenses chip was always leveled to better than this value, so that we were able to achieve alignment with an accuracy better than 200 nm between the two first bores,

which is a 5 times improvement over current capabilities [50]. But the main advantage of this technique is that it can he combined with the batch processing and assemhling of lens arrays.

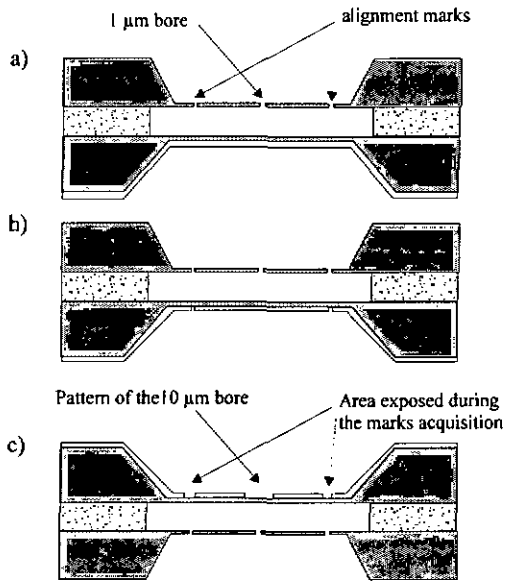

Figure 4.10: Process flow chart of the alignment procedure.

The different steps in the alignment procedure are summarized in figure 4.10. After the machining of the first electrode and the bonding of the Pyrex and the second electrode, the resist is spun on the backside of the second electrode (a). The sample is then mounted on the stage of the e–beam exposure tool and leveled. The reference mark in the first electrode are centered with respect to the e–beam deflection field, and projection-exposed in resist trough the second membrane. The resist is then developed to reveal these marks (h). Finally, the sample is mounted upside down in the e-beam lithography tool and

the second electrode's bore pattern is exposed using the projected mark structures in the resist for conventional e-beam alignment (c).

Gold-silicon eutectic bonding.

Since the potential of the accelerating electrode and of the aperture must be the same, it is desirable to simplify the wiring by assembling the two silicon chips supporting these membranes using a conductive bond. But because of the already made silicon membrane/Pyrex spacer/silicon membrane stack, such a bond must be done at low temperature ($< 500°C$). A gold-silicon eutectic bonding technique [82] was chosen because it is performed at a low temperature and owing to its conductive propriety. This is in fact the eutectic alloy with silicon, which is formed at the lowest temperature (363 °C). A layer of 10 nm of chrome and 100 nm of gold is deposited on one of the silicon chips. The chrome layer is used as an adhesion promoter for the gold layer, and simultaneously act as a diffusion barrier for the gold where diffusion is not needed. Thus, the gold will react only with the second chip. Since silicon oxide is also a good diffusion barrier for gold, the native oxide on the chip surface is removed using a short BHF etch before bringing the two chips into intimidate contact.

Figure 4.11 shows a bonding interface, where the upper part is the chip on which the chrome-gold layer was deposited (no diffusion), the lower interface, which is not as sharp, displays interdiffusion. Figure 4.12 shows a cracked bond obtained by applying a shear strength larger than 2 MPa. The star patterns characteristic of an eutectic material germination are visible [83], together with piece from the second chip which demonstrates how strong such a bond can be. The chrome-gold layer is deposited selectively on the frame of the future aperture membrane using a lift-off technique.

For our application, conductivity and bond strength are already good enough with only a fraction of the interface bonded. Thus only a very light pressure is applied between the

two chips, and the stack is put in an oven at 400 °C in nitrogen atmosphere (to prevent oxidation problems) during 10 min.

Final process

To summarize the fabrication of this source lens, figure 4.13 shows its process flow chart. The silicon membrane is first fabricated by EDP etching using an SiON mask pattern by optical lithography and etched with BHF(a). Then the 1 μm bore, the optical marks for tip alignment, and the reference marks are patterned and etched by RIE into the first electrode (b). The silicon membrane/Pyrex spacer/silicon membrane stack is assembled and bonded by AC anodic bonding (c). In the next step, the reference marks of the first electrode are transferred into the resist spun on the back-side of the second electrode by an exposure trough the membrane (d). These marks are used to align the

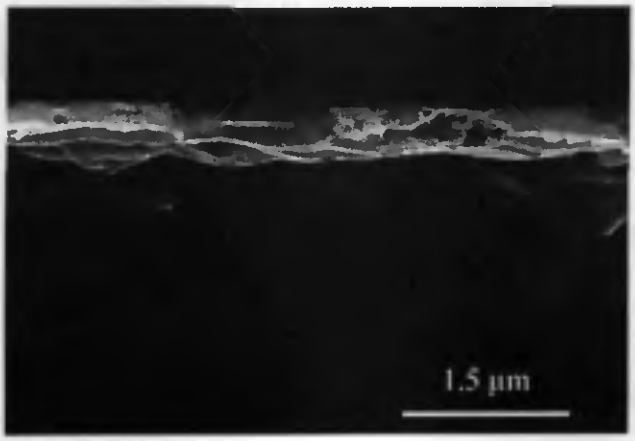

Figure 4.11: Gold-silicon interface of a cleaved sample, showing the interdiffusion of the two components.

Figure 4.12: Gold surface after gold-silicon eutectic bonding and after the bond was broken. The characteristic star structures of a eutectic alloy can be seen.

bore of the second electrode, which is then patterned and is transferred by RIE (e). To add the aperture, a third silicon membrane chip is bonded to the already made stack by eutectic gold-silicon bonding (f). Finally, using the same process as with the second electrode, the aperture pattern is aligned with the lens axis, and transferred into the membrane (g). To conclude this section, figure 4.14 shows an optical photograph of a completed source chip, which contains an array with seven precisely aligned lenses.

4.2 Source lens testing

The testing and characterization of the microcolumn as well as the lithography experiment were mainly done by my two colleagues Camille Stebler and Urs Staufer. This section gives only an overview of the experiments done with the lenses described above. For more

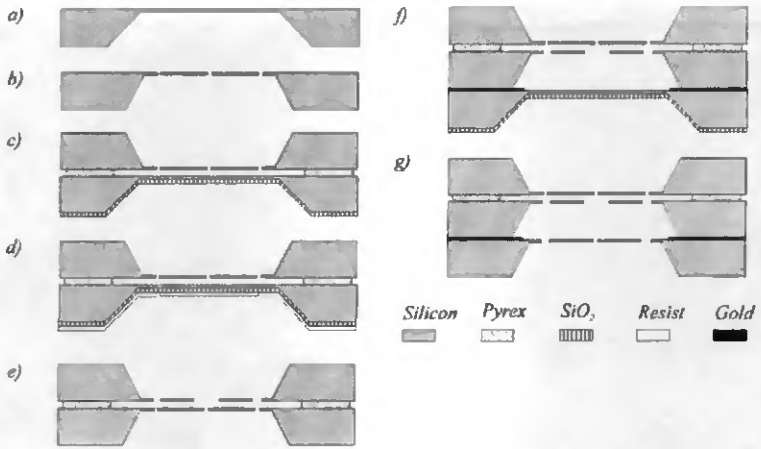

Figure 4.13: Process flow chart of the source lens process.

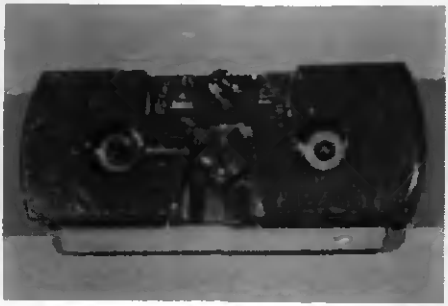

Figure 4.14: Picture of the fabricated source lens array mounted on the lens holder.

details about the testing, low energy lithography, and the instrumentation, the reader is referred to the thesis of Camille Stehler (to be presented at the Institute of Physic of Basel University), and the following papers [71, 65, 84, 85], several examples can be find in the appendix.

The test setup consists of several compooents which are outlined in block diagram in figure 4.15. There is a device for positioning the field emission tip, a microlenses

stage containing also a miniaturized fine machined scanner-stigmator, a sample stage, a channeltron (photomultiplier), a microchannel plate, and an electronic controller unit.

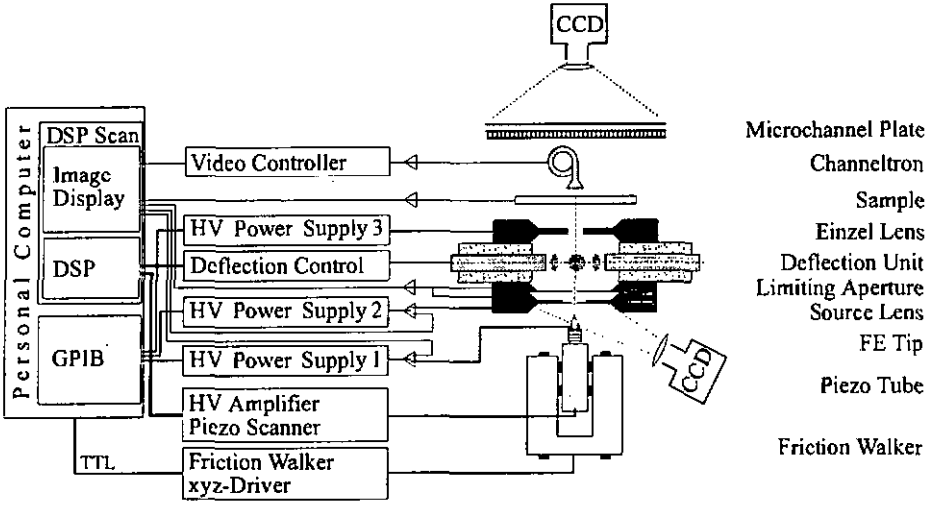

Figure 4.15: Block diagram of the microcolumn test setup.

A source lens was mounted together with an objective lens obtained from the group of Philip Chang. First, the maximum applicable voltage between the two electrodes of the same lens was checked. No instability or arcing was found up to 700 V, yielding an electric field of 14 V/μm. This is greater than the usual value given for the breakdown voltage into vacuum, but is not too surprising, as an increase of the breakdown voltage is generally observed when the dimensions are decreased. Nevertheless, we can conclude that we are not limited by other effects such as, for example, instabilities of the membranes under electrostatic forces, or surface breakdown voltages on the Pyrex walls.

When operating the instrument at an energy of 200 eV and using perforated carbon-films as samples, a resolution of better than 60 nm in transmission has been achieved (see

figure 4.16). In the cross-section shown in figure 4.16b, two fibers separated by 60 nm can still be resolved. This optimum beam was obtained with a 2 μm aperture and with a current of approximatively 10 pA.

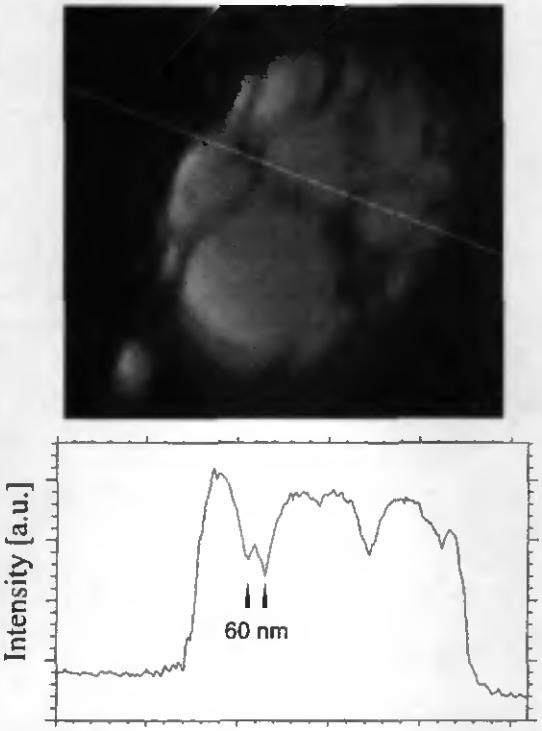

Figure 4.16: a) Two carbon fibers are stretched across a hole in carbon foil. The fibers are 60 nm apart and can still be resolved as it can be seen in the cross-section depicted in b).

At 100 eV, the resolution drops considerably and the beam shape displays a lot of distortion suggesting a charging effect (the beam have a star pattern). The most probable

explanatioo for this is charge trapping in a native oxide that has grown on the silicon surfaces of the limiting aperture. Such native oxides appear spontaneously in air, aod saturate at a thickness of 2 to 3 nm, which corresponds approximately to the range of electron penetration at 100 eV. We expected that, hy performiog a short BHF etch to remove the oxide and hydrogen-passivate the silicon surfaces just before mounting the lens in UHV, this charging effect would he decreased or disappear entirely. This type of passivation can withstand a couple of days in air and if duriog operation hydrogen-silicon hood can he crack under the electron impact, in UHV the oxidation process should he negligihle. These was, however, oo notahle. This means either that the charging elsewhere, or that the passivation was not intact hy the time the leos operatioo was started. In reality the time hetween the BHF etch and the mounting of the electrode in the UHV was oot very well controlled (time required to assemhle the microcolumo components) underwent several heat treatments (baking after electrode contacting with silver paint outgassing io the load lock) which are done, may have compromised the passivation and caused some oxidation. Further experiments would he necessary to check the efficiency of this passivation technique.

Chapter 5

Fabrication of an integrated silicon-based array of source lenses

The fahrication method described in the previous chapter already brings substantial improvements to alignment and assembling techniques. Although it avoids tedious alignment operations, however, the assemhly of multiple components remains a drawhack for the hatch processing of such lenses.

To cope with this drawhack, we developed a new lens fabrication technique designed especially for an electron energy of ~100 eV. Lenses are fully integrated in silicon, allowing a spacing hetween the electrodes of ~10 μm, which is suitahle for 100 eV and not possible with the previous technique since polishing Pyrex strips to a thickness less than 50 μm makes them too delicate to manipulate. Also a simpler hore alignment procedure with a precision in the 100-nm range is possible with this new process. Finally, the adequacy for hatch processing and array fahrication of these lens on single wafers is improved. The thickness of the lens was also reduced, first, hy using thinner wafers (270 μm), which will reduce the distance between the accelerating electrode and the aperture, and second, by reducing the distance between the extracting electrode and the accelerating electrode to

a strict minimum. Hence the spreading of electron trajectories in the source, due to the electron-electron interactions (where their density is large) will be reduced by decreasing this critical distance.

In this chapter only a two element source lens fabrication will be developed, the addition of tbe aperture was not done. Nevertheless the feasibility of such a lens has been demonstrated, and extension to a three element source lens and to an objective lens fabrication can be done.

5.1 Concept and fabrication technique of a two elements lens

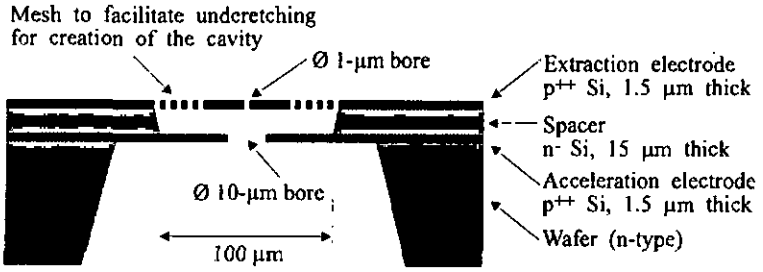

Figure 5.1: Basic configuration of an integrated two–electrode source lens.

Figure 5.1 is a schematic of a two-element source lens that we have fabricated. Tbe conceptual approach is to start with an epitaxially grown structure made of a 1.5-μm-tbick p^{++} layer, a 15-μm-thick n^- layer and another 1.5-μm-thick p^{++} layer to create two freestanding electrodes by machining a cavity in the n^- layer and using the p–n junction in reverse mode as isolation. The choice of such a silicon epitaxial structure to fabricate a lens was motivated by several points:

1. At 100 eV, the interelectrode spacing of the source lenses can be limited to 10 μm. As mentioned earlier, this space must be minimized for its e-beam quality to be as high as possible. It is not trivial to have an insulator spacer in tbe 10-μm range, which is quite thick for thin-film technology and too thin for bulk technology. Using silicon epitaxy, it is feasible to grow a well-controlled layer with a thickness of between practically 0 up to 50 μm or more.

2. As monocrystalline silicon is mechanically a very stable material and allows fine pattering by reactive ion etching (RIE), this is a material of choice for making electrodes that must be a stable thin membrane with very fine micromachined bores. To our knowledge, a $p^{++}n^{-}p^{++}$ silicon epitaxy structure is the only way to fabricate a stack comprising a monocrystalline silicon layer, an isolation layer, and a monocrystalline silicon layer without bonding or assembling.

3. A very precise profile of dopant concentration can be made during growtb to delineate the p^{++}–n^{-} junctions used for isolation. By carefully choosing the dopant concentration of the n layer, a breakdown voltage of the junction in reverse mode higher than the UHV breakdown voltage can be achieved [86], and hence it is not a limitation of the lens efficiency.

4. The p layer can be bigbly doped witb boron. Such a material has a very low etcb rate in an etbylenediamine-pyrocatechol(EDP)-based anisotropic silicon etching solution. Hence a cavity can be etcbed in the n^{-} layer without significantly altering the boron-doped layer, which will be the lens electrode.

5. Sucb a structure is UHV-compatible. It also supports a temperature treatment up to 800 °C (limited only by the diffusion of the boron atoms into the silicon). It is interesting in the case of using a Zr/O/W tip in Schottky mode as electron emitter, which must be heated to 1500 °C to be operated [51]. In this case, even if the tip is in close proximity to the lens, it will not alter the lens.

6. The fact that the spacer is no longer of an insulator material avoids charging effects due to trapped electrons at its surface.

To achieve such a thick epitaxial layer, a chemical vapor deposition (CVD) technique was used [76]. The critical part is the n^- layer, which must he carefully adjusted in order that the breakdown voltage he as high as possible. As in a Thyristor, for a given thickness, the dopant concentration is chosen to minimize the punch-through effect as well as the avalanche effect [86]. They are evaluated for the case of an ahrupt junction with a heavily doped p layer with the following equation:
The avalanche breakdown voltage:

$$V_A = 5.34 \times 10^{13} (N_n)^{-0.75} \text{ [V]}$$

The punch-through effect:

$$V_{PT} \simeq \frac{qN_nW_n^2}{2\epsilon_s} \text{ [V]},$$

where N_n and W_n are the dopant concentration and the thickness of the n layer, respectively, q the elementary charge, and ϵ_s the specific permittivity of silicon. With a thickness of 15 μm, the optimum dopant concentration is approximately 1.5×10^{15} cm^{-3}, which allows us to apply a voltage of higher than 200 V to the pnp junction without breakdown. Figure 5.2 show a graph of the optimum thickness of the n layer and the corresponding hreakdown voltage versus the n doping concentration.

To avoid electric field deformations around the optical axis hy the electric field in the depleted zone of the pn junction, a cavity is created hy etching far away from the optical axis of the n layer. For this purpose, a so-called EDP-hased anisotropic solution is used [75]. It has the advantage of a strong etch-rate reduction (up to 10^4) for the highly boron-doped layer (1×10^{20} cm^{-3}), which allows the n layer to he etched without altering the electrodes significantly. To create a cavity, a mesh surrounding the platform where the hores from the first electrode will he located is etched hy RIE in the first p^{++} layer.

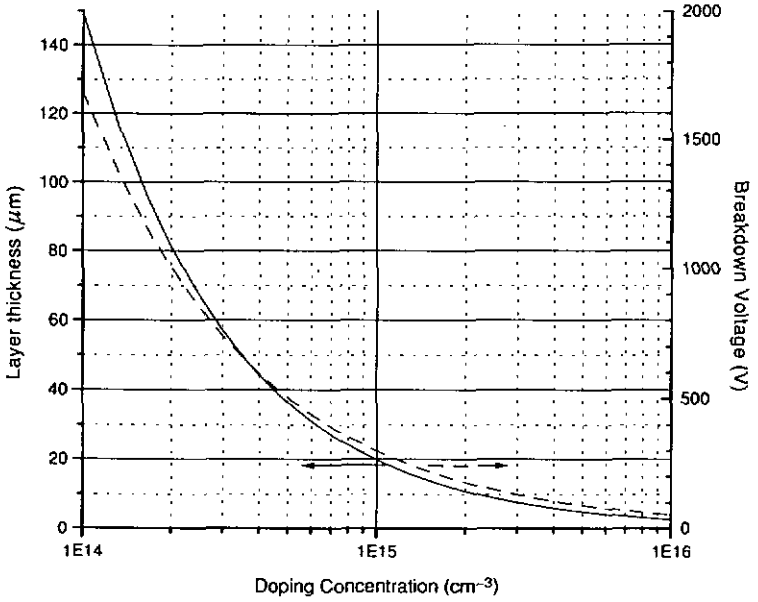

Figure 5.2: Graph showing the optimum thickness of the n layer and the corresponding breakdown voltage versus the n doping concentration.

It is formed by squares rotated 45° compared to the (111) silicon planes to have a high underetch rate (see figure 5.3). The n silicon layer under the mesh area will be removed until the etch is stopped at the buried p^{++} layer. During this procedure, a very strong underetching also takes place under the platform, whereas the design allows any etch to stop on the (111) planes. Hence, two freestanding silicon membranes are made without assembling or bonding.

To illustrate this, a process flow chart for the fabrication of a two-electrode miniaturized lens is shown in figure 5.4. After deposition on both sides of the wafer of a low-stress silicon oxide by plasma enhancement chemical vapor deposition (PECVD), a window is

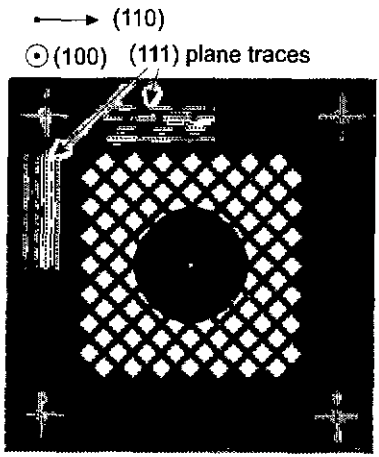

Figure 5.3: Design of the first electrode. The mesh squares are rotated 45° compared to the trace at the surface of the (111) crystallographic planes. The 1-μm hole from the first bore and the alignment marks (crosses) are also visible.

opened into the backside oxide by buffered hydrofluoric (BHF) acid etching. Then, by tetramethylammonium hydroxid (TMAH) anisotropic etching, the backside of the lens is pre-etched until about 50 μm before the buried p layer (figure 5.4a). From the front side, the 1-μm hole for the first electrode, the mesh, the contacting pad for the buried electrode, and the alignment marks — which will be used to align the hole of the second electrode — are then patterned into the p^{++} top layer (figure 5.4b, see also figure 5.3). Because the 1-μm bore must be very round and have little roughness, high-quality e-beam lithography is used, followed by two RIE steps as explain in the previous chapter. The pattern is transferred from the resist into the SiON mask with a CHF_3/O_2 RIE and from the SiON into the p^{++} silicon layer with a Ar/Cl_2 RIE. With this process, 1-μm bores with very vertical and smooth walls (roughness $<$ 10 nm) have been obtained in a 1.7-μm-thick

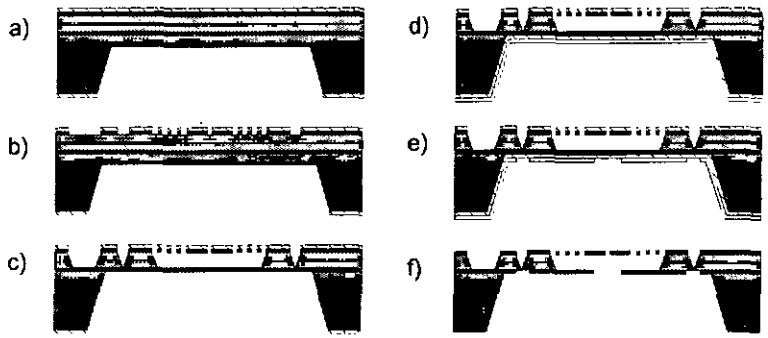

Figure 5.4: Process flow chart of the fabrication of a fully integrated, two-electrode source lens.

silicon layer. The cavity is then etched in the n layer using EDP, simultaneously with the alignment marks, the contacting pad for the second electrode, and the remaining 50 μm of the backside opening (figure 5.4c). Figure 5.5 shows the platform area after its release by the EDP etch.

The fabrication of the second electrode starts with a second PECVD evaporation of SiON and the spinning of the e-beam resist on the backside (figure 5.4d). Because the alignment between bores is a very critical parameter of lens quality, a special alignment technique was used. The alignment marks delineated in the same exposure as the first electrode bore (meaning that they are perfectly referenced with respect to first bore) are dimensioned such that, after being transferred through the n^- layer by the EDP etch, they have a dimension of a few 100 nm range when the etch reaches the second electrode. This is a very well-defined transfer of the alignment mark because the etch follows the four (111) crystallographic planes forming the inverted pyramid, yielding a perfect reference at the second p^{++} layer with which to align the second bore. Because any surface contrast in the backside of the second electrode can he seen to recognize these marks, a transmission

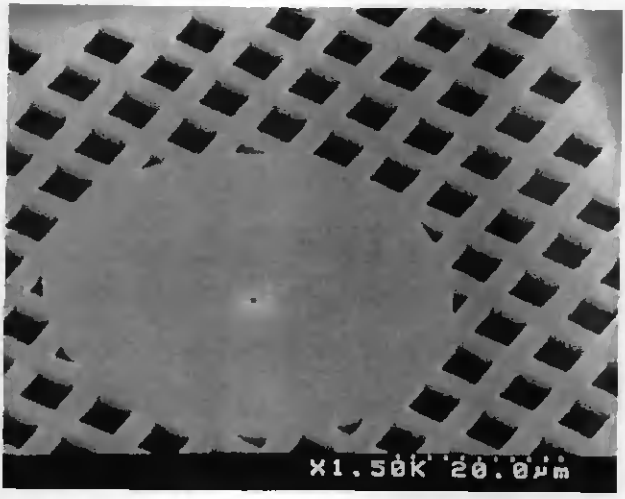

Figure 5.5: SEM image showing the platform area after its release by the EDP etch.

contrast or, more precisely, a thickness difference contrast is used for the alignment. From the backside, when the e-beam scans the alignment mark, the number of backscattered electrons is less than when the e-beam scans outside of the alignment mark because a significant part of the primary electrons go through this thin membrane ($\sim$3 μm) without generating secondary electrons.

The shift between the e-beam position and the alignment mark is then corrected to pattern the second bore exactly under the first one (figure 5.4e). Using the same RIE process as for the first electrode, the pattern is transferred into the second electrode, resulting in a completed two-electrode lens after removing the resist and the silicon oxide (figure 5.4f). Figure 5.6 shows a SEM image of the backside of the second electrode fabrication. The square shape corresponds to the cavity area and the small points located at each membrane corner correspond to the alignment marks. The areas appear darker,

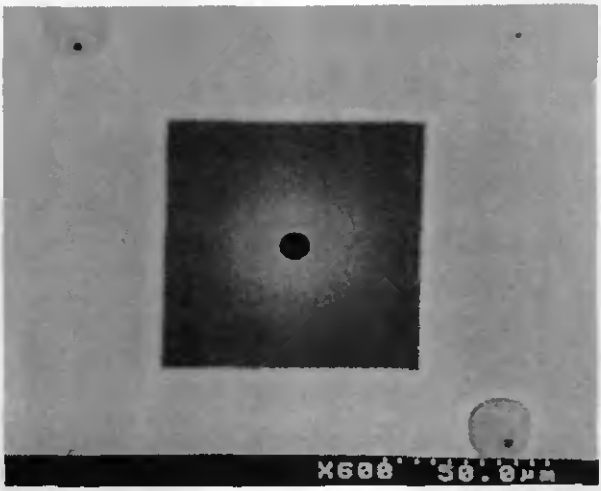

Figure 5.6: SEM image showing the back side of the second electrode after completed processing and demonstrating thickness contrast. The square in the middle is delineated by the second electrode membrane, and the small points at the corners are the pattern of crosses used as alignment marks transferred into the second electrode. The areas scanned during mark recognition are also visible.

because less electrons are backscattered. This thickness contrast is visible even with conventional electrons energy which was 25 kV, for this picture. The areas scanned during the mark recognition are also visible (upper left and lower right corner), because the resist was exposed during this operation and subsequently transferred into the second electrode.

This fabrication process offers other advantages. It not only enables the fabrication of very small lenses and very accurately aligned bores, it also allows fabricating a full array of lenses on the same wafer, with individual bore alignment. The dimension of

the array is only limited by the stability of the membrane delineated by the backside opening. Because silicon is mechanically very stable and the main part of the membrane has a thickness of 18 μm (the thickness of the entire *pnp* structure), it should be perfectly feasible to achieve arrays with a side length as long as 100 mm.

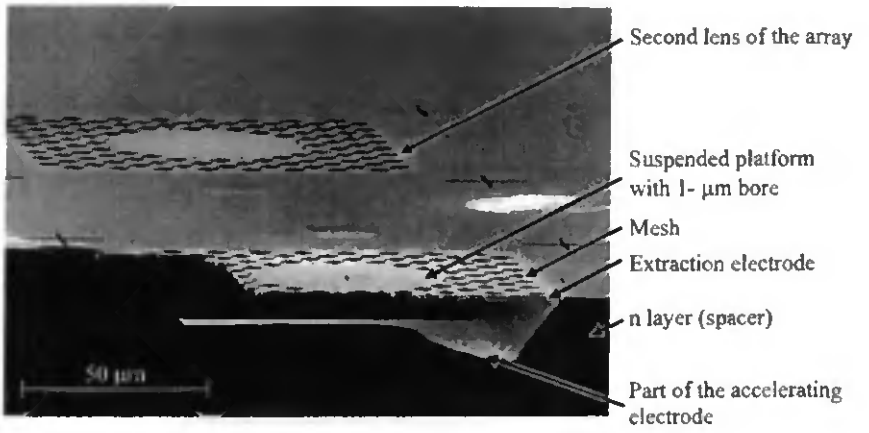

Figure 5.7: Cleaved array of source lens. The two electrodes shown are made in a highly boron-doped layer, and the cavity between them is etched in a low-doped n layer.

Figure 5.7 shows a part of a lens array fabricated by this process. The wafer was cleaved through one lens, showing the cavity between the two electrodes. We can see a part of the accelerating electrode (bottom membrane) and the extraction electrode formed by the platform suspended from the mesh. At the back a second lens of the array is also visible. Figure 5.8 shows a bottom view of the lens bores and the quality of their alignment. The 10-μm bore of the acceleration electrode and the 1-μm bore of the extraction electrode, which are separated by 15 μm, have a alignment accuracy in the 200-nm range.

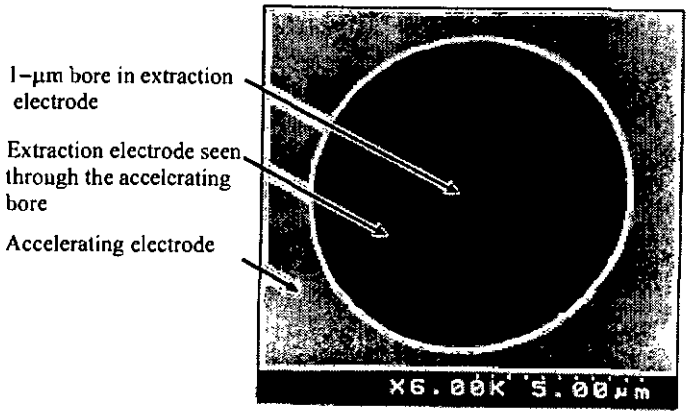

Figure 5.8: SEM bottom view of the lens hores. The alignment accuracy between the 10-μm and the 1-μm hores is within approximately 200 nm. The space hetween them is 15 μm.

5.2 Surface leakage current and active structure confinement

On a silicon surface not covered by another material, many impurities can act as dopants, producing a hending of the electronic hand at the surface. This effect creates a surface currents when a voltage is applied between two points. In silicon microelectronics, devices are always passivated by an oxide to avoid such surface leakage currents. In the case of microlenses the same effect occurs at the surface of the n^- layer on the cavity walls and at the horder of the chip walls. But for low-beam-energy applications, a thick oxide is not desirable because electrons can be trapped at the surface and can disturb the electric field at the electron optical axis.

To avoid surface leakage current, the area of the first electrode was limited to the

ahsolute minimum, without etching the n layer, and the walls in the cavity were passivated hy a very thin native oxide. The limitation of the first layer has two purposes. First, because the n layer is not removed, the surface path between the top electrode and the buried electrode is much greater than the thickness of the n layer. Hence, the resistivity of the surface is increased, and the surface current is reduced to a negligible amount. Second, it limits the area of the active *pnp* junction, thus reducing the leakage current of the junction itself. Figure 5.9 shows the test chip, the area of the top electrode of which is limited. At the center, a 3×1 lens array can be seen. The bright surface is the area where the top p^{++} layer was removed by RIE. This picture also shows that the alignment mark was made outside of the active area, and that the p^{++} channel, which forms the link of the lens itself to the connecting pads, was made in the p^{++} layer as well. A closeup picture of one lens platform is shown in figure 5.10. The n layer surface is observed to have a lot of pinholes, a problem which arises from the fact that the SiON mask was not sufficiently thick, and was not playing its role perfectly during the wet etching.

However, the n walls inside the cavity can still contribute to the leakage current hy the ahove-mentioned mechanism. The only solution is to passivate them. Our first attempt was to apply a hydrogen passivation by means of a BHF dip. But it was found that this kind of passivation is not stable enough in air at room temperature and that any increase of temperature that may occur during operation could be large enough to break the SiH bond. The second approach was then to apply an oxide to the n walls into the cavity without oxidizing the membrane. Normal oxidation, for example growing a thin oxide hy soft thermal annealing in air, is not desirable because it would oxidize the electrode surfaces. Instead, the following process was used. A short BHF etch removed the native oxide, and the silicon surface was passivated by hydrogenization. Then a potential was applied between the two electrodes in air. During this procedure, we observed that the leakage current drops steadily from an initially high value. After a few minutes, the current

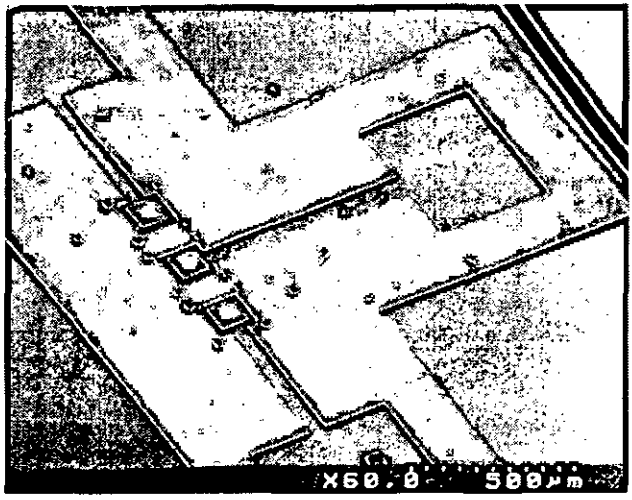

Figure 5.9: SEM image of the overall setup. It consists of a 3 × 1 array of two-electrode lens (center). The main part of the p^{++} top layer was removed to limit the leakage current (light part). Only a channel links the lenses to the pads.

became stable at a value that appears to be acceptable for operating the lens. Thus the I–V characteristic was stable with a reasonable leakage current of the *pnp* junction. This effect is illustrated in figure 5.11. The solid line shows the I–V curve of the *pnp* junction in air during the first applied voltage; the current reached 500 μA at 50 V. After being at 50 V for 5 min, the current decreased until it became stable at about 30 μA. Then, the characteristic also became stable at low current (dashed line). We explain this behavior as follows. When we first applied the voltage to the *pnp* junction, the current was relatively high, meaning that the power level was quite high (25 mW in the example cited above). We believe that the current is mainly a surface-leakage current, which means that the power is largely confined at the surface of the n walls inside the cavity, which constitutes

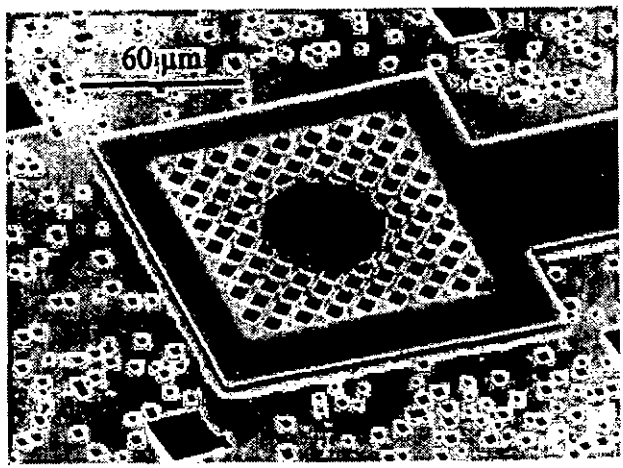

Figure 5.10: SEM image of one lens of the first electrode.

a relatively small volume compared to the power to be dissipated. The temperature rises locally to a value high enough to accelerate the oxidation of the walls. This oxidation prevents the surface current, the current drops, and the temperature decreases: hence, the process stops. Therefore, a localized oxidation of the walls of the n layer can be achieved without significantly altering the surface of the electrodes. This explanation, however, must be confirmed by further experiments.

5.3 Lens testing

To predict the breakdown voltage, the exact dopant profile in the actually grown n layer should be known. For this purpose, an analysis by secondary ion mass spectroscopy (SIMS) was performed, resulting in the profile of doping concentration shown in the figure 5.12.

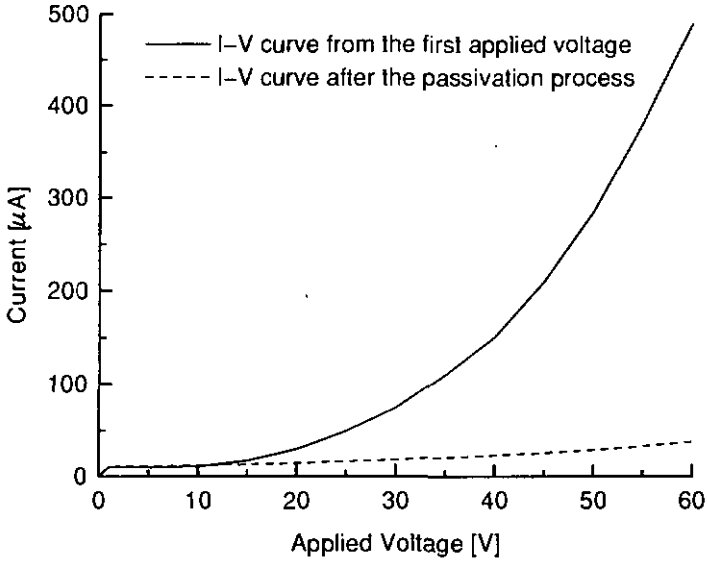

Figure 5.11: *I–V* curve of the lenses before (solid line) and after (dashed line) the passivation process. The current is reduced by a factor of more than 10 after applying 50 V for 5 min.

The SIMS analysis reveals that, the n^- layer is not homogeneous, and can even switch to p during the growth process. This epitaxy, which was done at the Microsystem Institute of the university of Stuttgart, was the attempt to grow a thick epitaxial n^- layer coupled with a highly doped p^{++} layer. After the growth of the high-dopant-concentration p^{++} layer, the side wall of the reactor was contaminated by boron impurities. During the n^- layer growth step, the growth temperature was increased to improve the deposition rate, causing the boron impurities stuck on the reactor walls to desorb and participate in forming the composition of the n layer. This caused the doping type of the n layer to change to p. After the boron was completely removed in the chamber, the layer change

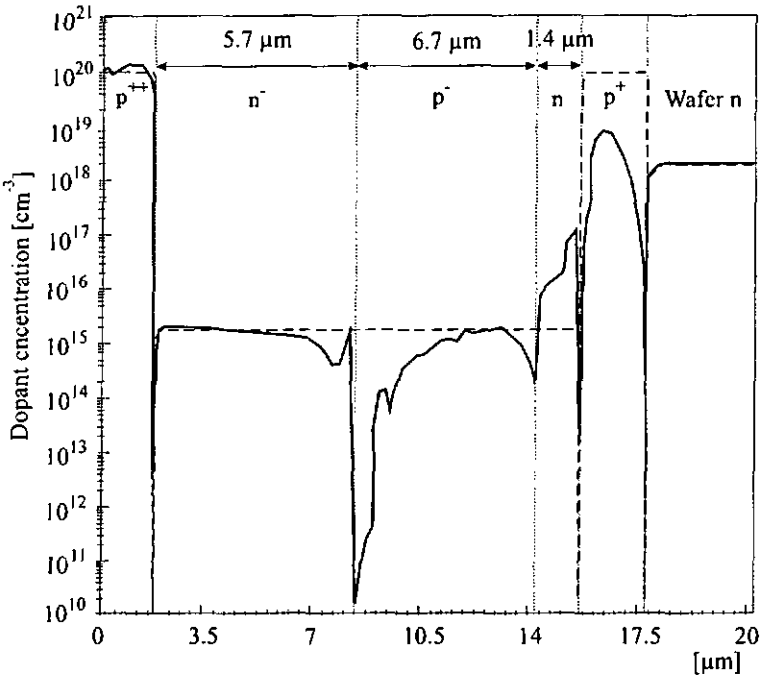

Figure 5.12: Doping concentration profile of the $p^{++}n^{-}p^{++}$ structure done by secondary ion mass spectroscopy (SIMS). In reality in the n^{-} layer the dopant concentration is not homogeneous, it even turn to p during the grow (solid line). In comparisons, the expected structure dopant profile is also plotted (dashed line)

to n. In the first p^{++} layer, because of the high temperature applied during the n growth step, an interdiffusion occurred lowering the dopant concentration of the p^{++} layer, causing the second membrane to have a thickness of only 500 nm instead of 1.7 μm. To avoid these problems, an improved epitaxial growth can be done by keeping the temperature relatively low throughout the growth, or by doing the epitaxy in two step: namely, the

first p^{++} layer and the two other $n^{-}p^{++}$ layers, with a cleaning step between them.

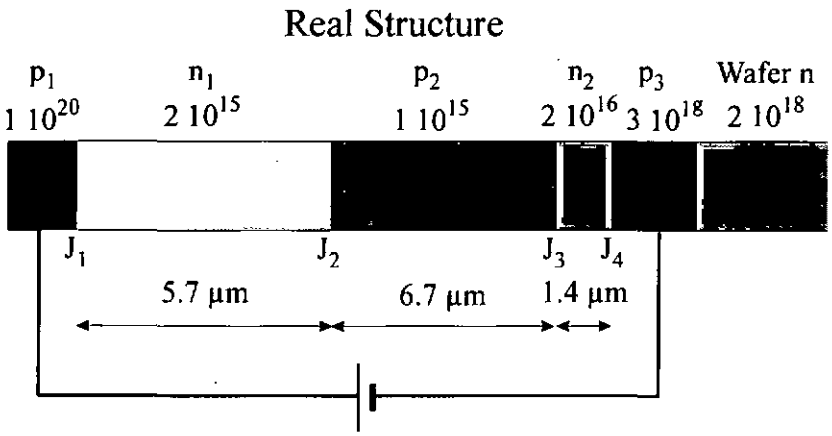

Figure 5.13: Simplified dopant profile structure.

To determine the breakdown voltage in botb polarities, since the structure is no longer symmetric, tbe sum of the breakdown voltages of each reverse-biased pn junction must be calculated. The structure can be simplified as shown in figure 5.13, where the mean dopant concentration in eacb part is taken. In reverse-bias (upper electrode negative), the junctions J_1 and J_3 are in reverse bias mode. For J_1 the depletion layer will grow in the n_1 layer (since $p_1 \gg n_1$), and for J_3 it will grow in the p_2 layer (since $p_2 \ll n_2$). Thus, the respective breakdown voltages for the avalanche effect and for the punch-through effect can be calculated from the following equations.

For avalanche breakdown voltage:

$$V_A = 5.34 \times 10^{13} (N_d)^{-0.75} \text{ [V]}$$

and for the punch-through effect:

$$V_{\rm PT} \simeq \frac{qN_dW_d^2}{2\epsilon_s}\ [\rm V],$$

where N_d and W_d are the dopant concentration and the thickness of the layer in which one the depletion will occur, respectively. In our device, we find: $V_{A1} = 179$ V, $V_{PT1} = 49.3$ V, $V_{A3} = 300$ V, and $V_{PT3} = 34.1\ V$, where the indices refer to the junction numbers. In both case the limitation is the punch-through effect, and the sum of the two punch-through voltages is equal to 83 V.

In forward bias (upper electrode positive), the junctions in reverse-bias mode are J_2 and J_4. For J_4 it is clear that the depleted zone will be in the layer n_2, giving $V_{A4} = 31.7\ V$ and $V_{PT4} = 30.6$ V. But for J_2, since the two dopant concentration are similar, the depletion will take place in both n_1 and p_2 layers, and is limited by the punch-through effect. The ratio of the depletion thicknesses of the two parts of the junction, x_{n1} and x_{p2} respectively, is given by:

$$x_{n1}N_{n1} = x_{p2}N_{n2}.$$

And the total thickness of the depleted zone w is,

$$w = x_{n1} + x_{n2} = \sqrt{\frac{2\epsilon_s}{q}\frac{N_{n1}+N_{p2}}{N_{n1}N_{p2}}(V_{bi} - V_{applied})},$$

where V_{bi} is the built-in potential of the pn junction. The punch-through effect will occur when p_2 is completely depleted since it is half as doped as the n_1 layer for an approximately the same thickness. V_{bi} can be neglected while, in silicon pn junctions, its value does not exceed 0.8 V. The punch-through V_{PT2} effect occurs when the applied voltage creates a depletion zone in p_2 equal to its thickness (W_{p2}). Hence, using the two above equations, V_{PT2} equal to:

$$V_{PT2} = V_{applied} = w^2\frac{q}{2\epsilon_s}\frac{N_{n1}N_{p2}}{N_{n1}+N_{p2}} = \frac{q}{2\epsilon_s}W_{p2}^2\frac{N_{p2}}{N_{n1}}(N_{n1}+N_{p2}).$$

This gives $V_{PT2} = 67.8$ V, resulting in a total breakdown voltage in forward bias of (31 + 68) V = 99 V.

The two calculated breakdown voltages, 99 V in forward mode and 82 V in reverse mode, are well correlated with the measured I–V curve, after passivation, as illustrated in figure 5.14. In forward mode, the breakdown voltage was higher than 100 V, and in reverse mode it was 78 V.

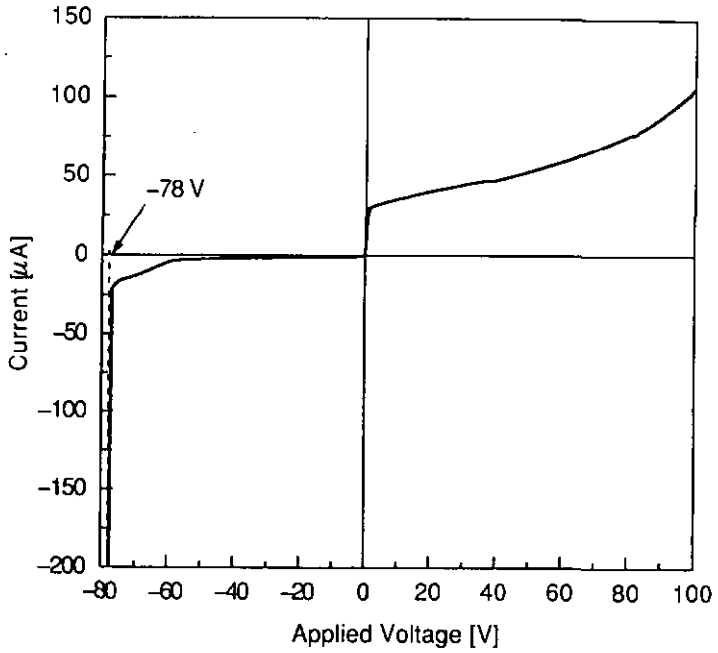

Figure 5.14: I–V characteristic of the lens. The breakdown voltage is higher than 100 V in forward mode (positive voltage to the upper electrode) and 78 V in reverse mode. They correlate well with the calculated breakdown voltage from the SIMS measurement, which is 99 and 82 V, respectively.

The lens was also operated as a source lens for extracting electrons from a field emission tip. The applied voltages were such that the lens worked in retarding mode. Testing was done in UHV using the same setup sketched in figure 5.15. The breakdown voltage of the p–n–p junction in UHV was at a lower value than in air. It occurred in forward-bias mode at 75 V. This reduction is not yet fully understood. If, at this low voltage, no crossover of the e-beam was achieved, the lens was successfully used as a source lens with a total emission current of up to 1.5 μA. The crossover was not achieved because of the relatively poor efficiency of the extraction electrode-accelerating electrode lens effect; the voltage applied was relatively low for the given second bore diameter (10 μm). This does not allow a very curved electric field distribution. Nevertheless the lens was successfully operated to control the energy of the extracted electrons, which is the goal of the source lens.

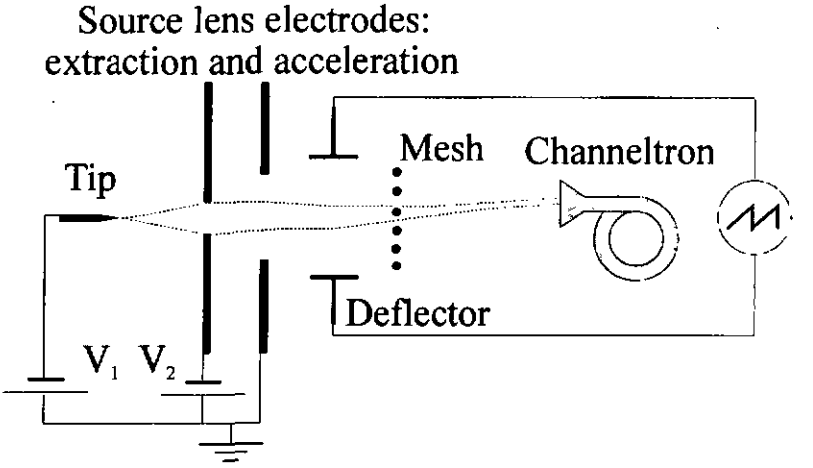

Figure 5.15: Setup for the two-element source lens experiments.

The next step will now be to add the objective lens in the microcolumn and to add a

limiting aperture to the source lens to obtain more information on microcolumn performance with such a lens.

5.4 Fabrication of a three-electrode source lens and an objective lens

Tbe fabrication of an objective lens using this technique will he even easier. Such a lens, for example, is made of three electrodes having the same bore diameter. Starting with an epitaxial layer made of a $p^{++}n^{-}p^{++}n^{-}p^{++}$ structure, and using a deep-RIE process, it is conceivable to etch the bores and the mesh through the entire stack in one RIE process using only one top mask. The electrodes need then only be released by an EDP etch. This process, shown in figure 5.16 has the advantage of being relatively simple and having self-aligned bores.

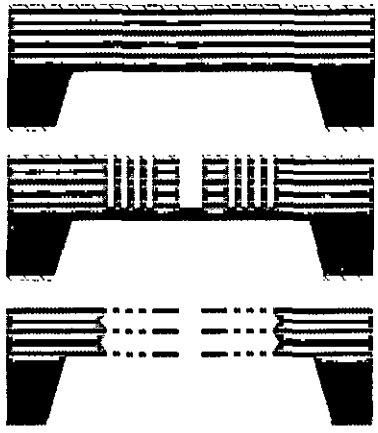

Figure 5.16: Basic process flow chart of the fabrication of a fully integrated objective lens.

For the source lens, such a process is not possible, because the bore diameters are usually not the same. For a three-element source lens, which includes the beam-limiting aperture, this is even more complicated. In this case, the largest bore is in the central electrode. This implies that for the third electrode an assembling step is necessary after the second bore has been fabricated. For this purpose, the same technique as explained in the previously chapter for adding the aperture can be used. This technique, adapted for the new device, is shown in figure 5.17. A chip consisting of a membrane comprising of 1.5-μm-thick p^{++} and 15-μm-thick n layer is fabricated. The n part where the future aperture will be is opened. Then it is mounted to the previously fabricated two-electrodes lenses by gold–silicon eutectic bonding or by low-temperature silicon–silicon bonding. The aperture electrode can also be made of a simple p^{++} membrane, but if large arrays are to be made, this electrode is not mechanically stable enough. For this reason we propose that the main area of the membrane should have a thickness consisting of the p^{++} and the n^- layer. This will act to reinforce the membrane. The n^- layer is removed only where necessary, i.e., in the optic axis area. After deposition of an oxide and spinning a resist on the backside of the third membrane, we scan the alignment mark of the first electrode with an e-beam from the front side. These marks act as a shadow mask; the tiny holes are transferred into the resist on the backside of the third membrane by exposing it through the third membrane. Then the resist is developed. From the backside, this mark will be recognized with the e-beam and used as a reference for delineating the aperture. With the same RIE process as used for the two first bores, the resist pattern is then transferred into the third membrane.

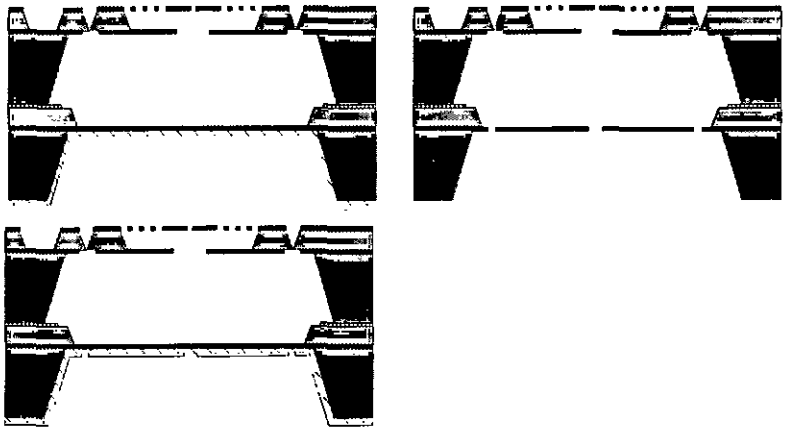

Figure 5.17: Basic process flow chart of assembling the two-electrode source lens of the aperture.

Chapter 6

Other Developments

Two other developments were made during this thesis, a double scanner-stigmator system, and an objective lens made by focusing ion milling (FIB).

6.1 Double scanner-stigmator

In our microcolumn setup, the scanner-stigmator system is made of a fine mechanical fabricated one-layer octupole. During beam deflection, such a configuration introduce aberrations, because the beam no longer passes along the axis of the objective lens. In a conventional SEM this problem is solved by a double deflection system that always keeps the beam on the axis of the column at the objective lens level. For the microcolumn discussed here, such an approach is desirable too (see figure 6.1). For this purpose, we developed a technique to batch-process a double deflection system on one chip, which is very compact (thickness: 600 μm) and has an alignment accuracy of the two octupole layers of a couple micrometers (typically 3 μm). The microcolumn's advantages are that its length can be reduced, that simplifies the microcolumn assembling by having this two-octupole layer in one chip, and that good alignment between the pole layers is possible (reduction of the beam distortion). Since the diameter of the octupole is typically in the

1 mm range, an alignment in the micrometer range is sufficient.

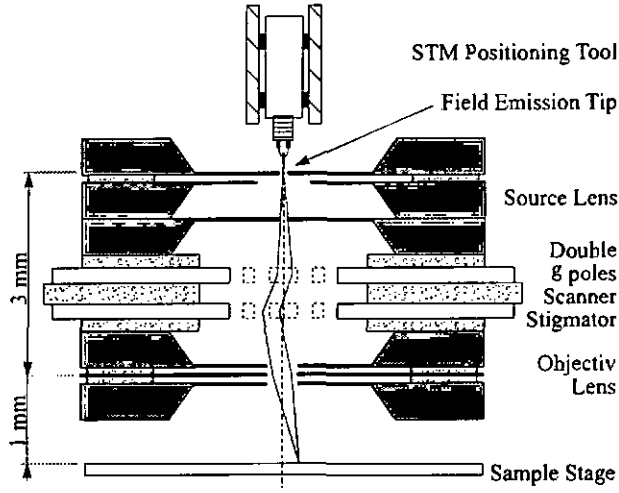

Figure 6.1: Basic configuration of the microcolumn with the two-deflection system.

6.1.1 Double octupole design

Basically such a deflector consists of hy two layers of height poles, the ends of which form a circle with the future path of the electron heam as its axis. These poles are located in an insulated hase with a hole that will leave a free path for the electron heam.

For the design, several points were taken into consideration: (1) the alignment between the two-pole layer must he accurate, to avoid additional distortion of the heam, (2) the ends of the poles must he freestanding to avoid field deformation due to the insulting hase, and (3) the poles must he thick enough to have the desired deflection angle for a reasonahle applied voltage. For our column working at low energy, the electron velocity is relatively low and the deflection efficiency will he greater than for common heam energies.

The scan range can be calculated as follows (c.f. figure 6.2). The deflection angle α_1 at the first level of the scanner is given by

$$\alpha_1 = \frac{t_p V_1}{dV_e} .$$

The deflection of the second level is equal at $\alpha_1 + \alpha_2$, hence

$$\alpha_2 = \frac{t_p V_2}{dV_e} - \alpha_1 .$$

The condition that the beam goes through the center of the objective lens is:

$$\frac{\tan \alpha_1}{\tan \alpha_2} = \frac{t_p + 2t_s + t_l}{2(t_i + t_p)} .$$

A simple geometrical argument then gives the scan-field to be:

$$S = 2\frac{(2W + t_l)(t_i + t_p)}{t_l + 2t_s + t_p} \tan \alpha_1 .$$

Without going into detail, we can define some parameters of these equations by the geometry of the microcolumn (d, t_p, t_s, t_l, W), others by the commercially available products (t_i, $V_{1,2max}$), or by the microcolumn application (V_e, S). For our practical case the thickness of the poles must be at least 70 μm thick (V_e = 100 V, d = 1.5 mm, $V_{1,2max}$ = 150 V, t_i = 0.4 mm, t_s = 0.6 mm, t_l = 0.1 mm, W = 1 mm, S = 0.1 mm).

A single-layer microfabricated octupole was made by the Chang group earlier [52]. The poles of the octupole are in a highly doped silicon wafer patterned with a deep reactive ion etching (RIE) step. Then, it is aligned and bond anodicaly to a Pyrex chip in which one hole has been drilled. Such a fabrication technique have the disadvantages of having a double octupole, two chips must be aligned together, and that several step are not suitable for batch processing (alignment and drill holes in the Pyrex). They also performed some experiments with poles made of gold electroplating, which have the same problem of structure transfer onto a substrate having in which holes have already been drilled.

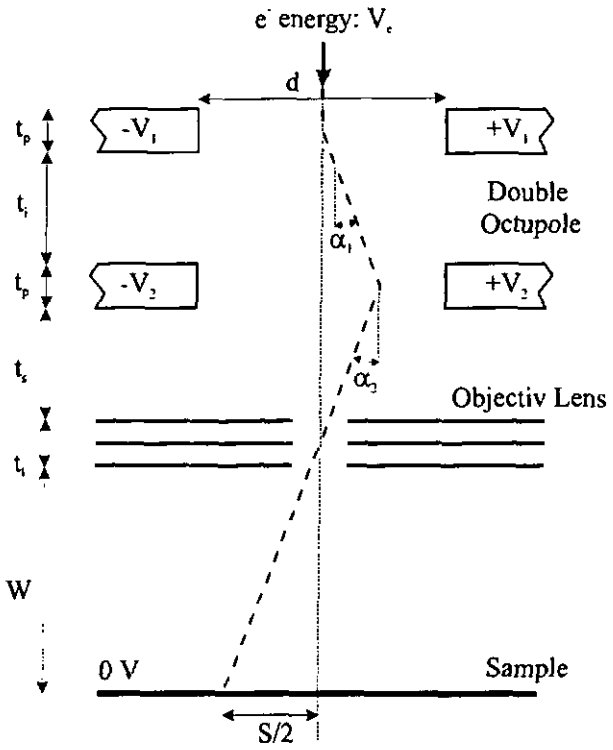

Figure 6.2: Dimension and voltage definitions to determine the double octupole size.

A new process has been developed to directly fabricate a double deflector in one chip using a photoetchable glass as the base insulator [87] [88], which allows structures to be plated on a pre-exposed glass. Since, the glass will not be developed until after the pole plating, freestanding end of the poles can be achieved after this development. This glass, consisting of Li_2/SiO_2-based material, is subject to crystallization by exposing it to UV light and by performing subsequent heat treatment, while a non-exposed part with the same thermal annealing is not prone to this phase transition. The crystalline phase is

lithium silicate, which is much more soluble in hydrofluoric acid (HF). As a result, the exposed part is etched in a 5% solution of HF, 50 times faster than the non-exposed part. For this fabrication, 3-inch, 400-μm-thick wafers of photoetchable glass from Hoya was used.

6.1.2 Process

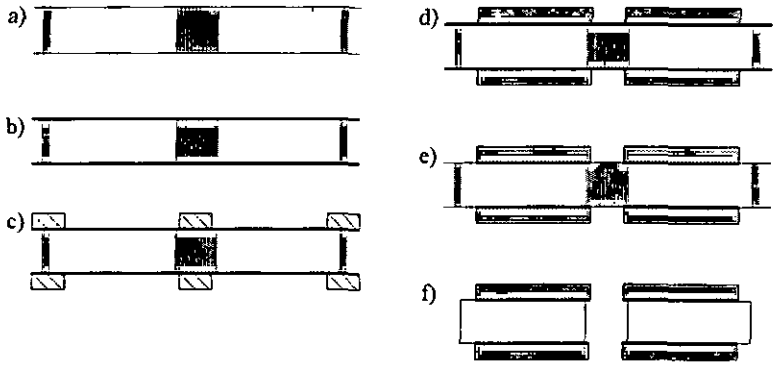

Figure 6.3: Process flow chart of double octupole fabrication.

In figure 6.3 the process flow chart of the fabrication of double octupole is presented. The process starts with the exposure of the hole in the photoetchable glass. The energy required at a wavelength of about 320 nm is 1.5 J/cm^2. The thermal annealing applied is a ramp from 25 to 350 °C at a rate of 150 °C/hour, a second ramp from 350 to 600 °C at a rate of 60 °C/hour, then the temperature is maintained 1 hour at 600 °C, and finally the temperature is decreased with a rate of about 100 °C/hour. This followed by a brief 5% HF etch (2 min) to improve the adherence of the metallic layers to the glass wafer. These layers are 500 Å and 1000 Å of chrome and gold, respectively (b). They are evaporated on both sides with an e-beam evaporation system, and will be used as a contacting layer

for electrodeposition.

The next step is the deposition and the patterning of a thick resist (c). We used a double layer of 50-μm-thick photosensitive foil called RISTON from DuPont [89]. This is a very cheap method to obtain a thick resist; the RISTON is simply laminated two times on both sides of the glass wafer to obtain a 100-μm-thick double-sided coated resist. To have a good alignment between the two octupoles, we used a double-sided aligner/exposer tool. First, the two masks (top and bottom) are aligned, then the glass wafer is aligned with the top mask through a special feature which can be aligned with the flat of the wafer. Hence, alignment of a couple of micrometers between the two octupole patterns can be performed, as well as a rough alignment with the glass holes of a couple of tens micrometers. Such an alignment with the flat is not very precise, but this is not important considering the size of the hole (3 mm) compared to the inner circle delineated by the poles (1.5 mm). The next step is the copper electrodeposition (d) of an 80-μm-thick layer done simultaneously on the both sides of the wafer. After the resist stripping and the chrome and gold etch (e), the glass can be developed (f). The development through the glass in a 5% HF solution takes approximately 30 min (if the HF solution is fresh, the etching rate is about 9 μm/min). During this operation trenches, which were also exposed at the same time as the holes and which delineate the border of the double octupole chip, were developed to facilitate chip separation.

6.1.3 First fabrication run

The first run of such a double octupole was performed. Unfortunately, the quality of the poles was not as good as expected, and the deflector could not be used. If freestanding poles have been made with this process, two problems occured. First, the definition and the adhesion of the RISTON was not good enough for this application (the distance between two poles is 100 μm), and several poles had bridges between them. Second, an

unexpected oxidation problem was encountered. After only a few hours poles turned hlue (one of the oxide pbases of copper). Such a copper oxidation does not appear for otber copper plating structures wbich maintain their reduced appearance for weeks. Certainly the copper bath was either too old or contaminated. Nevertbeless, it would be preferable to use gold to avoid oxidation. It was also planned to replace the RISTON resist with a new resist from IBM called SU-8 [52, 90]. Such a resist bas been tested, and structures with a thickness as high as 500 μm and an aspect ratio of 15 bave been demonstrated [91]. Figure 6.4 shows an SU-8 test structure showing the outstanding definition of this resist.

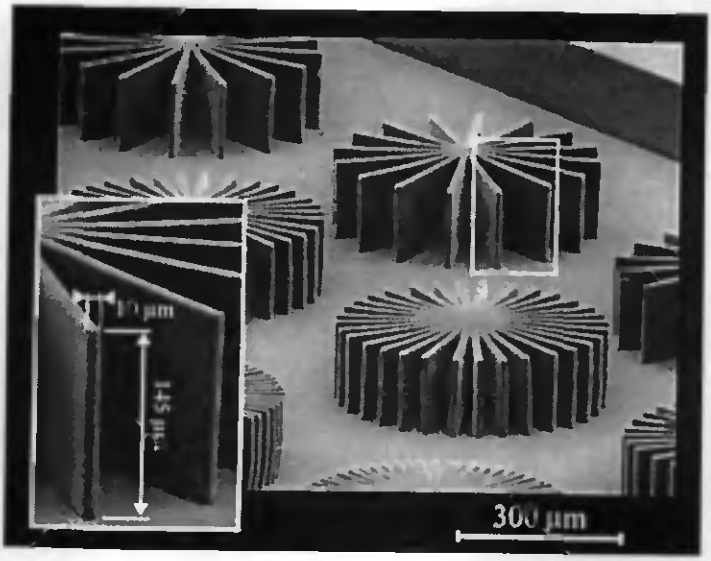

Figure 6.4: Structure of SU-8 demonstrating an aspect ratio of 15 for a 145-μm-thick resist layer.

6.2 Objective lens fabrication

The two source lens fabrication techniques described in the previous two chapters are perfectly compatible with objective lenses fabrication, but only few first experiments have been done on this topic, and no objective lens has yet been built by these means.

However, objective lenses were fabricated by focusing ion beam (FIB) milling. This is a very simple process, requiring no masking and no lithography. Figure 6.5 shows the two main steps of this process. First, a stack containing the three electrodes and the two spacers are fabricated by AC anodic bonding as explain in chapter 4. The central electrode was made by an ultra thin (4 μm) silicon wafer cleaved to the proper dimensions. Second, since the three electrode bores have the same diameter, the whole stack was milled simultaneously by delineating a circle with the FIB probe. Although this technique is simple, it is not suitable for the mid- or large-scale fabrication of lenses. To mill one lens having a 130-μm bore took more than 22 hours using the highest ion beam current available by the system.

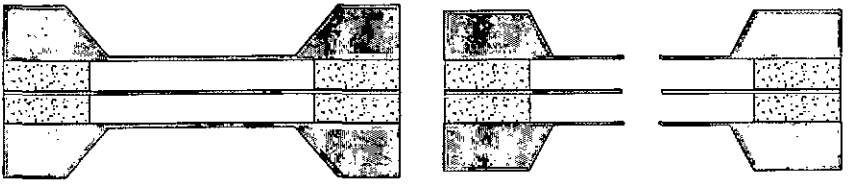

Figure 6.5: Schematic showing the two fabrication steps of an objective lens made by FIB milling.

Chapter 7

Conclusion

The goal of this thesis was to develop microfabrication techniques for the mid- or large-scale fabrication of miniaturized low-energy electron columns or arrays of such columns. The main part of this work was to make lenses for such columns; therefore, two different processes were investigated, and source lenses using these two techniques were fabricated.

The main idea for the lens fabrication, was to machine the lenses layer by layer, while using the previously machined electrode as a reference to align the following one. Since for lens fabrication high accuracy bore alignment is required, this technique allows the batch fabrication of lenses with a step where each lens is individually aligned precisely on the wafer or in the array.

The first type of lens was made of a stack of silicon membranes for the electrodes and Pyrex stripes for the dielectric spacer. The two key points of this fabrication were, the assembly of silicon membrane/Pyrex/silicon membrane stack, and the alignment of the second and third electrodes. In order to fabricate the stack, a technique based on AC anodic bonding was developed. This technique demonstrated strong enough bonding on both sides of the Pyrex such that the bonds withstood the further processing steps of the lens fabrication. We observed a bond quality four times better with the AC technique

than with a sequential DC anodic bonding. The alignment of the second and third electrodes regard with the first electrode was done by exposure of a resist layer through the silicon membrane by using e–beam lithography and the electron penetration depth in the membrane. This technique allowed reference marks from the first electrode to be transferred into a resist spun on the back side of the second electrode. By carefully choosing the electron beam energy and the exposure time, very fine transferred marks have been done and alignment in the 200 nm range was demonstrated, which is five times better than previously demonstrated techniques.

Arrays of three element source lenses were successfully fabricated and tested. Mounted in the microcolumn, 60 nm resolution was measured at 200 eV and 10 pA. At lower energy (100 eV), a charging effect was limiting the beam quality. This problem is attributed to either a native oxide or particles on the limiting aperture. Procedures were investigated to prevent the native oxide formation by hydrogen passivation and to clean the device, to avoid the charging effect.

The second lens fabrication technique involved a fully integrated array of two-element lenses in silicon made by an epitaxial growth $p^{++}n^{-}p^{++}$ structure, and dopant selective anisotropic etching techniques. The isolation of the electrodes was done by the *pn* junction of the epitaxial structure in reversed-bias mode. This technique allows the dimension of the lens to be reduced and facilitated the fabrication because no assembling was necessary. A new bore alignment procedure was developed using an observed thickness contrast in e-beam imaging, and 200 nm alignment accuracy was demonstrated. A special process to passivate the silicon surface was also developed to prevent surface leakage current.

Arrays of these integrated lenses were successfully fabricated and tested. The breakdown was measured to be lower than expected, but it is mainly due to epitaxial problem which occured during sample growth. The epitaxial profile was not optimize to maximize the breakdown voltage of the structure.

Finally, first experiments to fabricate a double octupole, using electroplating and a photoetchable glass substrate in which the exposed part is used as a sacrificial layer, have been done.

In summary, we have shown various microfabrication techniques for building a miniaturized electron column, suitable for batch processing and allowing a greater integration of high quality microcolumn. Witb the integrated lens technology coupled with the microfabrication tecbnique for the octupole, column lengths of less than 1 mm can be fabricated, which is necessary for working at the 100 eV regime. However, not all tbe integration problems have beeo treated and resolved in tbis work. For example, a major issue will be to integrate a source consisting of an electron-emission tip self-aligned with the source lens where the capability to prepare the tip without altering the extraction electrode can be performed. Or, for an integrated microcolumn array, the problem of interconnections, specially for the octupole, must be solved. The fabrication of microcolumn will surely provide numerous researcb themes for future theses.

Chapter 8

Appendix: Microcolumn testing and lithography experiments

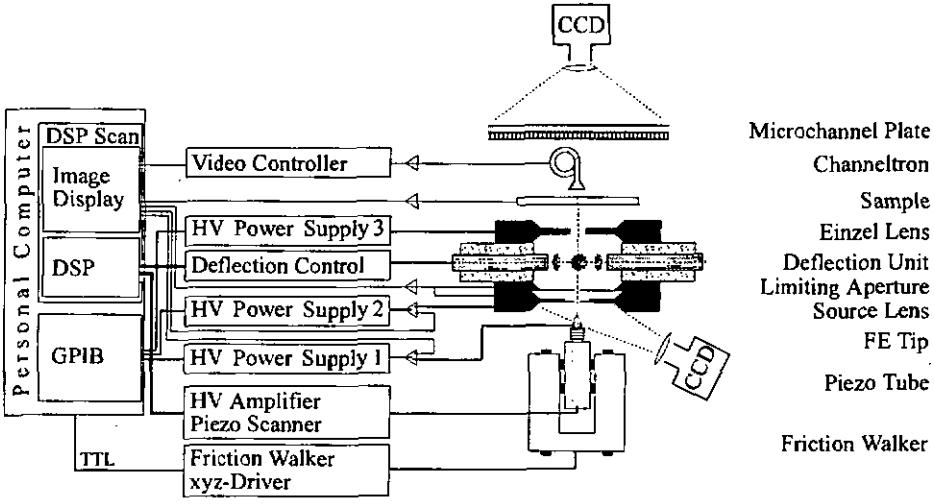

Figure 8.1: Block diagram of the microcolumn test setup.

The test setup consists of several components which are outlined in block diagram in

figure 8.1. There is a device for positioning the field emission tip, a microlenses stage containing also a miniaturized fine machined scanner-stigmator, a sample stage, a channeltron (photomultiplier), a microchannel plate, and an electronic controller unit.

8.1 Testing of a two-element source lens

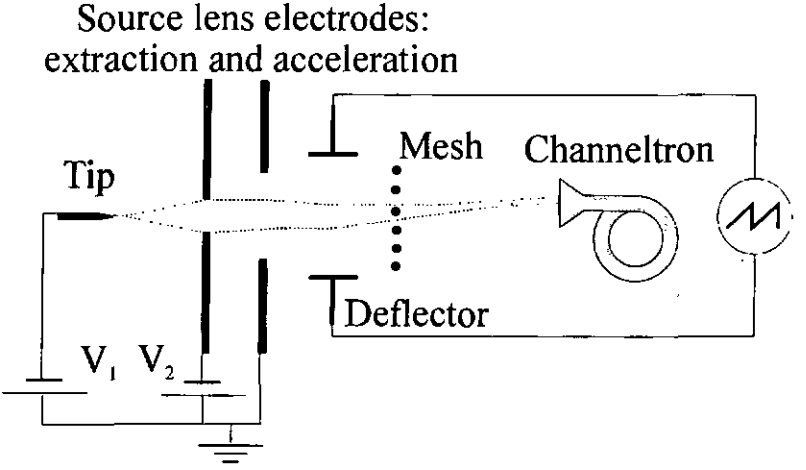

Figure 8.2: Setup for the two-element source lens experiments.

Various proprieties of the source lens have been assessed using a two-element version of the lens without an aperture, and without an objective lens. Omitting them, of course, influence the achievable spot size, but do not affect the lens proprieties. Testing was done in UHV using the simplified setup sketched in Figure 8.2.

The first experiment was to test the lens's focusing effect. For that purpose, we scanned a 1000 mesh with the beam formed by the lens. The tip position and the extraction potential ($V_1 - V_2 = 470$ V) were kept constant and, hence, the emission current was also

constant. An increasing deflection angle is observed for decreasing beam energies defined by V_1.

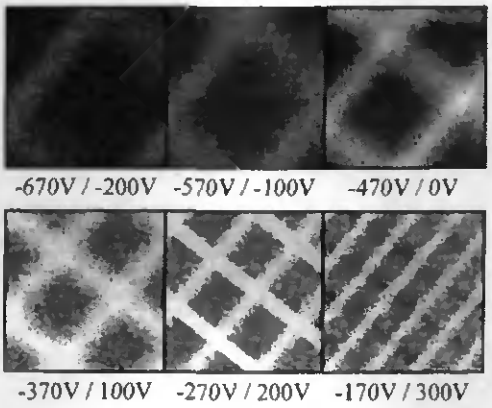

Figure 8.3: Mesh imaging with various tip/ accelerating voltages (corresponding to V_1/V_2 in Fig. 8.2).

Figure 8.3 shows an example of such experiments. During this experiment, the potential distribution in the lens changes because $V_1 - V_2$ was constant. At approximately $V_1 = 200$ V a crossover could be formed, which demonstrates that the electron beam can be focused with 270 eV.

8.2 Microcolumn resolution with a three element source lens

A source lens including the aperture was mounted together with an objective lens obtained from the group of Philip Chang. When operating the instrument at an energy of 200 eV and using perforated carbon-films as samples, a resolution of better than 60

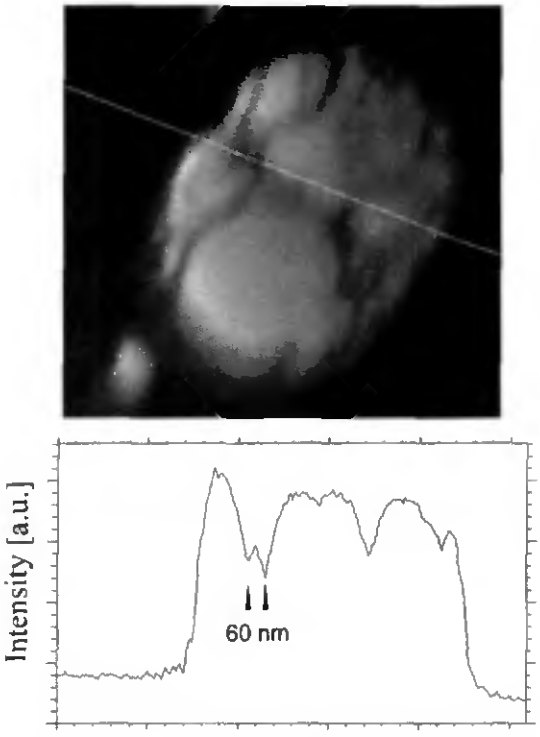

Figure 8.4: a) Two carbon fibers are stretched across a hole in carbon foil. The fibers are 60 nm apart and can still be resolved as it can be seen in the cross-section depicted in b).

nm in transmission has been achieved (see figure 8.4). In the cross-section shown in figure 8.4b, two fibers separated by 60 nm can still be resolved. This optimum beam was obtained with a 2 μm aperture and with a current of approximatively 10 pA.

No secondary electron detector was mounted in our setup, since there is too little room available between the sample and the objective lens to mount a commercially available one. It is also not really possible to channel the secondaries to one side as it is done in a conventional arrangement, because the electric fields involved would disturb the low-

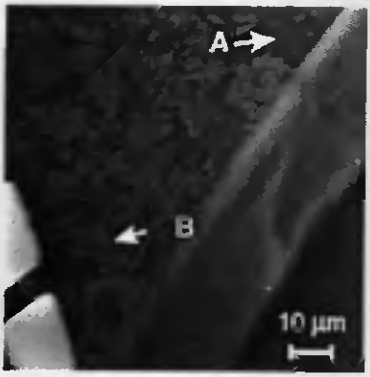

Figure 8.5: This picture shows the frame of a copper 1000-mesh, which was used for calibrating the scanning field. Marker A points to an area on the copper surface. The bright structures (indicated by B) on the frame of the mesh are residues of silver-paint which has been deposited for mounting the mesh to the sample holder.

energy primary beam. We found, however, that for perforated samples or for images taken close to the sample edge, another approach may he used; by applying a voltage of ahout +100 V to the entrance electrode of the channeltron behind the sample, secondary-electrons were channeled through the holes or around the edges to the detector (see figure 8.2). Areas up to 100 μm away from an edge or from a hole could still he imaged. As an example, figure 8.5 shows a copper-mesh with some residues of silver-paint. A clear material contrast hetween copper and silver is ohservahle. In figure 8.6, the edge of a silicon wafer is depicted. The resolution is somewhat worse compared to the pure transmission mode. The distance between two features that can still be resolved is ahout 100 nm.

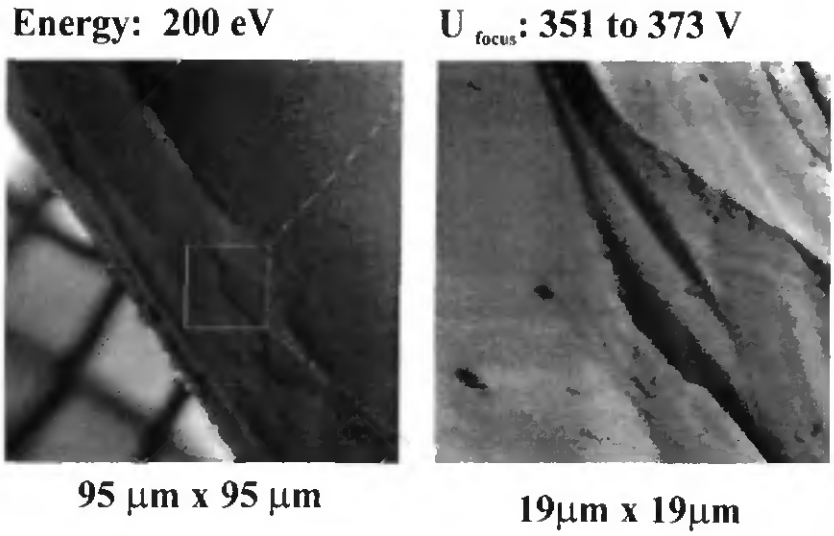

Figure 8.6: These two pictures were taken from an edge of a cleaved silicon wafer. The picture on the right hand is a close-up of the first picture. It gives an indication of the achieved resolution which is about 100 nm.

8.3 Low energy lithography

Feasibility experiments in lithography using the microcolumn at hoth 100 eV and 200 eV, were also performed. Three types of resist were tested: PMMA, hydrogen passivate layers, and self-assembled monolayers (SAM) [65]. These experiments were done a source lens without aperture and with an objective lens. Because of the missing aperture, the resolution was not checked.

8.3.1 Experiments with PMMA

Figure 8.7 shows ant exposure in 50 nm thick PMMA layer. The first square was

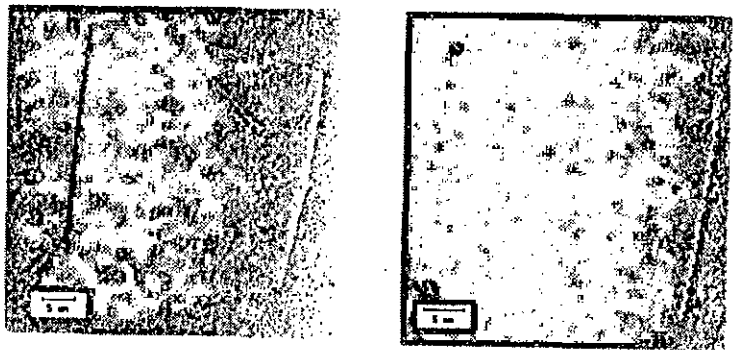

Figure 8.7: Shaded AFM image of two squares written in 50-nm-thick PMMA. a) Exposure made with 100 eV electrons and a dose of 148 $\mu C/cm^2$, yielding to a profile depth of 3 nm. b) Exposure with 200 eV electrons and a dose of 125 $\mu C/cm^2$, yielding a profile depth of 7 nm.

written with 100 eV electrons and a dose of 148 $\mu C/cm^2$, and the other with 200 eV electrons and a dose of 125 $\mu C/cm^2$. The depths, measured by AFM, are 3 and 7 nm respectively, which corresponds to the different penetration ranges of the electrons. The shape of the pattern is not rectangular, as it should be, but reflects the distortions in the electron optical system.

8.3.2 Experiments with hydrogen passivated silicon

Hydrogen passivated silicon was exposed at 100 eV. This inorganic resist consist of a monolayer of hydrogen formed on silicon substrate by dipping the sample in BHF. A minimum exposure dose of 4 mC/cm^2 at 100 eV has been reported in the literature [40]. The hydrogen atoms are believed to be desorbed upon electron impact, leaving behind bare silicon at the surface which oxidizes in air later. The resulting native oxide can then

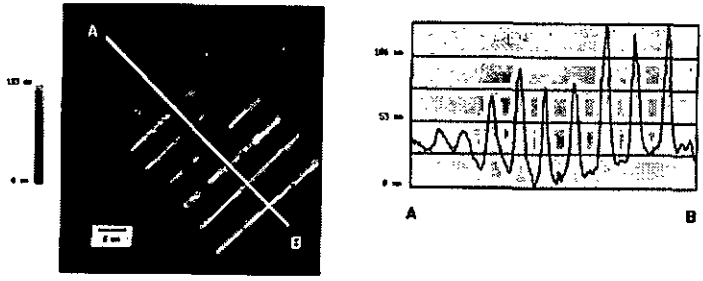

Figure 8.8: Grey-scale AFM image of (a) nine rectangles exposed with different doses in a hydrogen-passivated layer on Si(110) and transferred into the silicon using a TMAH wet etch. The doses were from left to right 1.7, 3.6, 4.4, 4.8, 5.3, 5.9, 6.4, and 7.0 mC/cm^2. (b) Cross-section along AB through the lines, demonstrating the observed dose dependence.

be used as an etch mask during a subsequent pattern transfer with TMAH. Based on this model, no effect of the dose is expected to be observable as soon as the minimum dose is exceeded and as long as the oxidation takes place after the writing is completed. The AFM image in figure 8.8a) shows lines patterned as rectangles nominally 2 μm $\times$ 40 μm in size. The exposure was done under UHV conditions (2×10^{-10} mbar). A clear dependence on the dose is observed (see figure 8.8b), which indicates that the exposed area were not completely depassivated.

8.3.3 Experiments with SAM

A first test exposure was also made on a self-assembled hexadecanethiol ($CH_3(CH_2)_{15}SH$) monolayer. The sample was prepared by first evaporating onto the silicon substrate a thin Ti adhesion layer (0.5 nm), followed by a 20-nm-thick layer of gold. The SAM was then formed on the gold layer by immersing the substrate in a solution of hexadecanethiol and ethanol. This material is known to be a self-developing resist. Figure 8.9 shows a

scanning electron microscope picture of four square patterns in the SAM.

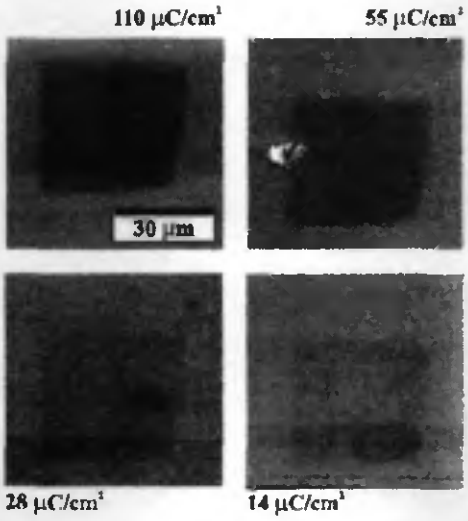

Figure 8.9: SEM image of squares written with 100 eV electrons in a SAM. The dose were from left to right and from the top to bottom 110, 55, 28, and 14 $\mu C/cm^2$.

Acknowledgments

My first thanks go to my two colleagues, Urs Staufer and Camille Stebler, for the very enjoyable three years we spent working together on microcolumns and for their friendship. I also would like to acknowledge Prof. Güntherordt of the University of Basel and Dr. Pierre Guéret. of IBM Rüschlikon for their supervision and support of this project. To these names, I would like to add Prof. Nico de Rooij, my supervisor, whose enthusiasm is so communicative that the work always seemed hetter after having discussed it with him than hefore, which I found was the hest type of motivatioo to go out and improve thiogs even more. Gilles Beljakovic, a diploma student, also worked with me a lot, and I thank him for the good collaboration we had. I am also grateful to Philip Chaog and Kim Lee, of IBM T.J. Watson Research Center, for their extremely useful advice and support.

My warmest thanks go to Peter Vettiger, my manager at IBM duriog the last few months of this work, who was always available to tackle administrative as well as technical prohlems, and who lent me his house so that I could write this down in peace. His tendency to push me in new directions got me working pretty hard, but we certainly had a good time.

It has heen a great pleasure for me to work for this project in IBM's Research Lahoratory in Rüschlikon, in a particularly stimulating environment. For an extended education in microfabrication technologies, which was essential to my work, I am greatly indebted to Gian-Luca Bona, Jürgen Brugger, Kurt Dätwyler, Urs Deutsch, Roland Germann, Ed-

ward Kiewra, Ilana Massarek, Damien Prongué, Heinz Richard, Peter Roentgen, Hugo Rothuizen, Heinz Schmidt and Peter Vettiger. I also feel that interacting with my multi-disciplinary colleagues has heen a great opportunity for me to open my mind and to find perhaps more original solutions as well as getting a hetter understanding of physical and chemical phenomena which were not really clear from my engineer's point of view. In this context, I would like to thank especially Frédéric Arrouy, Hans Biehuyck, Emmanuel Delamarche, Thomas Jung, Jean-Pierre Locquet, Markus Pfister, Heinrich Rohrer and Christophe Rossel. A very special thanks to Lilly Pavka and Charlotte Bolliger, of the IBM publications office, for their outstanding work in helping me publish my results. My friends Lilly Pavka, Hugo Rothuizen, Eliav Haskal, Urs Staufer and Peter Vettiger were also tremendously helpful in helping me correct the english of my thesis. I guess that without them, I would have had some problems delivering my manuscript in time.

I am also grateful to Willy Heuherger, Giovanni Sasso, and all the technical and administrative staff of the IBM Zurich Research Lahoratory in general, for their help.

Many of these persons have offered me their friendship, and this was perhaps my main achievement during this thesis. Accordingly, I would also like to thank the more recent arrivals Cornel Andreoli, Ute Drechsler, Alex Casser, Grégoire Genolet, Sandrine Vernier and Dorothea Wiesmann.

During this project, I had the opportunity to interact with many groups from different institutes to exchange knowledge and develop new ideas. I thank especially

1. Georges André Racine, Nico de Rooij, and in general all the Sensors, Actuators and Microsytems Lahoratory of the University of Neuchâtel.

2. Huhert Lorenz and Philippe Renaud from the Institute of Microsystems of the Swiss Federal Intitute of Technology, Lausanne.

3. Nancy LaBianca and Jane Shaw from IBM T.J. Watson Research Lahoratory.

4. Harald Gross, Wolfram Ziegler and Dieter Kern, of the University of Tübingen.

5. Uwe Behringer of IBM Sindelfingen.

6. Christian Schönenberger of the University of Basel

7. Wolfgang Appel of tbe University of Stuttgart

Philip Chang, Hans-Peter Herzig, Urs Staufer and Peter Vettiger are gratefully acknowledged for their acceptance in taking part in my defense jury.

This work was supported financially by the Swiss gouvernment trough the priority program OPTIQUE I.

Finally, I would like to thank my family and friends outside IBM, from Zurich, from Echallens and from the EPFL (and extensions), for their patience and support.

List of Publications

M. Despont, G.A. Racine, P. Renaud, N.F. de Rooij, "New design of micromachined capacitive force sensor", J. Micromech. Microeng. 3 (1993) 239-242.

M. Despont, U. Staufer, C. Stebler, R. Germann, P. Vettiger, "Microfabrication of lenses for miniaturized electron column", Microelectronic Engineering, 27 (1995) 467-470.

C. Stebler, M. Despont, U. Staufer, "Miniaturized e-beam writer: testing of components", Microelectronic Engineering, 27 (1995) 223-227.

M. Despont, U. Stebler, C. Stebler, H. Gross, P. Vettiger, "Electron-beam microcolumn fabrication and testing", Microelectronic Engineering, 30 (1996) 69-72.

C. Stebler, M. Despont, U. Staufer, "Microcolumn based low energy e-beam writing", Microelectronic Engineering, 30 (1996) 45-48.

J.P. Locquet, F. Arrouy, E. Mächler, M. Despont, P. Bauer, E.J. Williams, "Local electrochemical oxidation/reduction: First step towards a new lithography", Appl. Phys. Lett. 68 (1996) 1999.

M. Despont, H. Gross, F. Arrouy, C. Stebler, U. Staufer, "Fabrication of a silicon-Pyrex-silicon stack by AG anodic bonding", to be published in Sensors and Actuators A.

M. Despont, G. Beljakovic, C. Stebler, U. Staufer, P. Vettiger, "Fabrication of an integrated silicon-based lens for low-energy miniaturized electron columns", Japanese Journal of Applied Physics 35 (12B).

H. Lorenz, M. Despont, N. Fahrni, N. LaBianca, P. Renaud, P. Vettiger. "Epon SU-8: *Low-cost negative resist for MEMS*", presented at the MicroMechanic Europe 1996 conference (MME'96), Barcelona, Spain. And to be published in J. Micomech. .

C. Stebler, M. Despont, U. Staufer. "Secondary Electron Imaging by Means of a Microfabricated Electron Column", to be published in J. Phys. *III* France, 6 (1996) 1435-1439.

J. Brugger, G. Beljakovic, M. Despont, N.F. de Rooij, P. Vettiger. "Silicon Micro/Nanomechanical Device Fabrication Based on Focused Ion Beam Surface Modification and KOH etching", presented at the Micro- and Nano-Engineering 1996 conference (MNE'96), Glasgow, Scotland. To be published in Microelectronic Engineering.

M. Despont, H. Lorenz, N. Fahrni, J. Brugger, P. Renaud, P. Vettiger, "High-Aspect-Ratio, Ultratbick, Negative-Tone Near-UV Pbotoresist for MEMS Applications", to be published in tbe proc. of the 10th IEEE Int'l Workshop on Micro Electro Mechanical Systems (MEMS'97), Jan 26-30, Nagoya, Japan.

Curriculum Vitae

Name: Michel Despont
Birth: July 9, 1967 in Lausanne (Switzerland)
Nationality: Swiss
Languages: French (mother tongue), good knowledge of English, working knowledge of German

Employement Experience

1996 - present IBM Zürich Research Laboratory, Rüschlikon (Postdoctoral work).
- Microfabrication of Atomic Force Microscope (AFM) levers.

1993 - 1996 IBM Zürich Research Laboratory, Rüschlikon (while pursuing a PhD degree).
- Microfabrication of electron microlenses and testing of a miniaturized low-energy electron column.

1988 - 1993 Swiss Federal Institute of Technology of Lausanne (while pursuing a degree in Engineering).
- Design, fabrication and testing of a microfabricated capacitive force sensor.
- Design and fabrication of electrodes for a capacitive torque sensor.
- VLSI design of an integrated circuit for high-speed digital multiplication, based on a logarithm-addition-antilogarithm principle.
- Design and fabrication of an anti-arcing device for circuit breaker (in collaboration with Heinemann Electric SA, 1345 Le Lieu, Switzerland).

1984 - 1988 Kudelski SA (while pursuing an apprenticeship in electronics and fine machining).
- Digital and analog electronic circuit design and testing.
- Design and machining of fine mechanical devices.

Education

1996 PhD degree from the Faculty of Sciences of the University of Neuchâtel, Switzerland.

1993 Engineering degree in microtechnology at the Swiss Federal Institute of Technology of Lausanne, Switzerland (EPFL).

1988 Technician degree in fine mechanics and electronics. Apprenticeship at Kudelski SA, CH-1033 Cheseaux sur Lausanne, Switzerland.

Bibliography

[1] R. Stulen. Processes of the future. *Solid State Technology*, February:48, 1995.

[2] Semiconductor Industry Association. Process of the future, updated roadmap identifies technical, strategic challenges. *Solid State Technology*, February:42–53, 1995.

[3] M.D. Levenson. Extending optical lithography to the gigabit area. *Solid State Technology*, February:57–66, 1995.

[4] K.R. Early, M.L. Schattenburg, and H.I. Smith. *Microelectronic Engineering*, 11:317, 1990.

[5] H.I. Smith. 100 years of X-rays: Impact on micro- and nanofabrication. *J. Vac. Technol. B*, 13(6):2323–2328, 1995.

[6] T. Haga, M.C.K. Timone, H. Takenaka, and H. Kinoshita. Large-field (> 20 x 25 mm^2) replication by EUV lithography. *Microelectron. Eng.*, 30:179–182, 1996.

[7] N.M. Ceglio, A.M. Hawryluk, D.G. Stearns, D.P. Gaines, R.S. Rosen, and S.P. Vernon. Soft X–ray lithography. *J. Vac Sci. Technol. B*, 8(6):1325–1328, 1990.

[8] H. Hiroshima, S. Okayama, M. Ogura, and M. Komuro. Nanobeam process system: An ultrahigh vacuum electron beam lithography system with 3 nm probe size. *J. Vac. Sci. Technol. B.*, 13(6):2514–2517, 1995.

[9] P. Vettiger, K. Daetwyler, and D. Webb. Combined e-beam and optical exposure of diazo resists for lift-off processing. In *Proceedings of Microcircuit and Engineering, Cambridge, England*, pages 289–296. Academic Press, 1983.

[10] C. David, H.U. Mueller, B. Voelker, and M. Grunze. Low energy electron printing using a self-assembled monolayer resist. *Microelectronic Engineering*, 30:57–60, 1996.

[11] H.C. Pfeiffer and W. Stickel. Prevail - an e-beam stepper with variable axis immersion lenses. *Microelectronic Engineering*, 27:143–146, 1995.

[12] H. Yamashita, K. Tokunaga, Y. Kojima, H. Nozue, and E. Nomura. Resolution analysis in electron-beam cell projection lithography system. *J. Vac. Sci. Technol. B*, 13(6):2473–2477, 1995.

[13] Y. Sohda, Y. Someda, and Norio Saitou. Coulomb effect in cell projection lithography. *J. Vac. Sci. Technol. B*, 13(6):2419–2423, 1995.

[14] O. Fortagne, P. Hahmann, and Ch. Ehrlich. Weprint 200 - the fast e-beam printer with high throughput. *Microelectronc Engineering*, 27:151–154, 1995.

[15] B. Lischke, G. Christaller, K.H. Herrmann, A. Heuberger, E. Knapek, H. Kniepkamp, H. Rose, W. Ruettenauer, and G. Spiegel. An e–beam comb–probe printer for nanolithography. *Microelectronic Engineering*, 9:199–203, 1989.

[16] H. Schaefer, P. Schaeffer, S. Kleindiek, and K.-H. Herrmann. Advances in the electron optical design of a multi e-beam comb probe printer. *Microelectronic Engineering*, 11:355–358, 1990.

[17] E.S. Snow and P.M. Campbell. AFM fabrication of sub–10–nanometer metal–oxide devices with in situ control of electrical properties. *Science*, 270:1639–1641, 1995.

[18] A. Kumar, H.A. Biebuyck, and G.M. Whitesides. Patterning self-assembled monolayers: Applications in materials science. *Langmuir*, 10:1498–1511, 1994.

[19] M.J. Lercel, G.F. Redinbo, M. Rooks, R.C. Tiberio, H.G. Craighead, C.W. Shen, and D.L. Allara. *Microelectronic Engineering*, 27:43, 1995.

[20] T.H.P. Chang, D.P. Kern, and L.P. Muray. Microminiaturization of electron optical system. *J. Vac. Sci Technol.*, B 8(6):1698–1704, 1990.

[21] C.A. Spindt, I. Brodie, L. Humphrey, and E.R. Westerberg. *J. Appl. Phys.*, 47:5248, 1976.

[22] T.H.P. Chang. Proximity effect in electron-beam lithography. *J. Vac. Sci Technol.*, 12(6):1271–1275, 1975.

[23] E. Hammel, H. Loescher, G. Stengl, H. Buschbeck, A. Chalupka, H. Vonach, E. Cekan, W. Fallmann, F. Paschke, and G. Stangl. Masked ion beam lithography for proximity printing. *Microelectronic Engineering*, 30:241–244, 1996.

[24] L.R. Harriott, S.D. Berger, J.A. Liddle, G.P. Watson, and M.M. Mikrtchyan. Space charge effects in projection charged particle lithography systems. *J. Vac. Sci. Technol. B*, 13(6):2404–2408, 1995.

[25] U. Drodofsky, M. Drewsen, S. Nowack T. Pfau, and J. Mlynek. Atom lithography using light forces. *Microelectronic Engineering*, 30:383–386, 1996.

[26] R. Imura, T. Shintani, K. Nakamura, and S. Hosaka. Nanoscale modification of phase change materials with near–field light. *Microelectronic Engineering*, 30:387–390, 1996.

[27] R. Imura, H. Koanagi, M. Miyamoto, A. Kikukawa, T. Shintani, and S. Hosaka. Demonstration of nanometer recording with scanning probe microscope. *Microelectronic Engineering*, 27:105–108, 1995.

[28] C.T. Salling, I.I. Kravchenko, and M.G. Lagally. Atomic manipulation for patterning ultrathin films. *J. Vac. Sci. Technol. B*, 13(6):2828–2831, 1995.

[29] H.A. Biebuyck, N.B. Larsenand, E. Delamarche, and B. Michel. Lithography beyond light: microcontact printing with monolayer resists. *Invited contribution to special issue of IBM J. Res. Develop. to be published first quarter of 1997.*

[30] S.Y. Chou, P.R. Krauss, and P.J. Renstrom. Imprint lithography with 25–nanometer resolution. *Science*, 272:85–87, 1996.

[31] T.H.P. Chang, L.P. Muray, U. Staufer, M.A. McCord, and D.P. Kern. Arrayed lithography using an STM based microcolumn. *SPIE Institutes for Advanced Optical Technologies IS10*, pages 127–158, 1993.

[32] H.W. Fink, H. Schmid, H.J. Kreuzer, and A. Wierzbicki. Atomic resolution in lensless low-energy electron holography. *Phy. Rev. Let.*, 67(12):1543–1546, 1991.

[33] W.D. Meisburger, A.D. Brodie, and A.A. Desai. Low-voltage electron optical system for the high-speed inspection of integrated circuits. *J. Vac. Sci. Technol. B*, 10(6):2804–2808, 1992.

[34] A.N. Boers. Resolution limits for electron-beam lithography. *IBM J. Res. Develop.*, 32(4):502, 1988.

[35] Technical data from Jenoptik Technologie GmbH, Jena, Germany.

[36] W. Patrick and P. Vettiger. Optimization of the proximity parameters for electron beam exposure of nanometer gate-length GaAs metal-semiconductor field effect transistors. *J. Vac. Sci. Technol. B*, 6(6):2037–2041, 1988.

[37] Y.-H. Lee, R. Browning, N. Maluf, G. Owen, and R.F.W. Pease. Low voltage alternative for electron beam lithography. *J. Vac. Technol.*, B 10(6):3094–3097, 1992.

[38] M.A. McCord and R.F.W Pease. Lithography with scanning tunneling microscope. *J. Vac. Sci. Technol. B*, 4(1):86–88, 1986.

[39] P.A. Peterson, Z.J. Radzimski, S.A. Schwalm, and P.E. Russell. Low-voltage electron beam lithography. *J. Vac. Sci. Technol. B*, 10(6):3088–3093, 1992.

[40] N. Kramer, J. Jorritsma, H. Birk, and C. Schoenenberger. Nanometer lithography on silicon and hydrogenated amorphous silicon with low-energy electrons. *Microelectronic Engineering*, 27:47–50, 1995.

[41] M.A. McCord and T.H. Newmann. Low energy, high resolution studies of electron beam resist exposure and proximity effect. *J. Vac. Sci. Technol. B*, 10(6):3083–3087, 1992.

[42] J.C. Tracy, NATO Summer School Lectures, Ghent, (1972).

[43] K.Y. Lee, S.A. Rishton, and T.H.P. Chang. High aspect ratio aligned multilayer microstructure fabrication. *J. Vac. Technol. B*, 12(6):3425–3430, 1994.

[44] G.M. Sheed et al. *Rev. Sci. Instrum.*, 64(9):2579, 1993.

[45] H.W. Fink. Mono-atomic tips for scanning tunneling microscopy. *IBM J. Res. Dev.*, 50:460–465, 1986.

[46] H.F. Gray, L. Ardis, and G.J. Campisi. Ultrahigh-vacuum field emitter array wafer tester. *Rev. Sci. Instrum.*, 58:301–304, 1987.

[47] C.W. Jones, S.K. Jones, M. Walters, and B. Dudley. Microstructures for particle beam control. *J. Vac. Sci. Technol. B*, 6:2023–2027, 1988.

[48] T.H.P. Chang, D.P. Kern, and M.A. McCord. Electron optical performance of a scanning tunneling microscope controlled field emission microlens system. *J. Vac. Sci Technol. B*, 7(6):1855–1861, 1989.

[49] M.A. McCord, T.H.P. Chang, D.P. Kern, and J. Speidell. *J. Vac. Sci. Technol. B*, 6:1851, 1989.

[50] T.H.P. Chang, M.G.R. Thomson, M.L. Yu, E. Kratschmer, and S.A. Rishton. Electron beam technology - SEM to microcolumn. *To be published to a special issue in nanotechnology of the Microelectronic Engeenering journal*, pages 127–158, Nov/Dec 1996.

[51] H.S. Kim, M.L. Yu, E. Kratschmer, B.W. Hussey, M.G.R. Thomson, and T.H.P. Chang. Miniature Schottky electron source. *J. Vac. Sci. Technol. B.*, 13(6):2468–2472, 1995.

[52] K.Y. Lee, N. LaBianca, S.A. Rishton, S. Zolgharnain, J.D. Gelorme, J. Shaw, and T.H.P. Chang. Micromachining applications of a high resolution ultra-thick photoresist. *J. Vac. Technol.*, B, 1995.

[53] S. Zolgharnain, K.Y. Lee, S.A. Rishton, D. Kister, and T.H.P. Chang. Characterization of a GaAs metal-semiconductor-metal low energy electron detector. *J. Vac. Sci. Technol. B*, 13(6):2556–2560, 1995.

[54] D.A. Crewe, D.C. Perng, S.E. Shoaf, and A.D. Feinerman. Micromachined electrostatic electron source. *J. Vac. Sci Technol.*, B 10(6):2754–2758, 1992.

[55] A.D. Feinermann, D.A. Crewe, M. Ruffin, C.A. Spindt, P.R. Schwoebel, C. Holland, and A.V. Crewe. Initial images with a partially micromachined SEM. In *EIPBN'96, ATLANTA*, 1996.

[56] A.D. Feinermann, D.A. Crewe, and A.V. Crewe. Microfabrication of an array of scanning electron microscopes. *J. Vac. Sci. Technol. B*, 12(6):3182–3186, 1994.

[57] W. Liu, T. Ambe, and R.F. Pease. Miniature low voltage electron beam column with micro-objective lens and compact secondary electron detector. *J. Vac. Technol. B*, Nov/Dec issue, 1996.

[58] B.D. Terris and D. Rugar. In *Proceedings of 50th EMSA Meeting, edited by G.W. Bailey, J. Bentley and J.A. Small.*, page 952. San Francisco Press, 1992.

[59] W. Hofmann, L.Y. Chen, and N.C. MacDonald. Fabrication of integrated micromachined electron guns. *J. Vac. Sci. Technol. B.*, 13(6):2701–2704, 1995.

[60] W. Hofmann, L.Y. Chen, , J.H. Das, and N.C. MacDonald. Micromachined field emission devices. *Microelectronic Engineering*, 30:523–526, 1996.

[61] W.K. Lo, G. Parthasarathy, C.W. Lo, D.M. Tanenbaum, H.G. Craighead, and M.S. Isaacson. Titanium nitride coated tungsten cold field emission sources. *J. Vac. Technol. B*, Nov/Dec issue, 1996.

[62] H.S. Fresser, F.E. Prins, and D.P. Kern. Metal-semiconductor-metal structures as electron detector for 1 kV microcolumns. *Microelectronc Engineering*, 27:159–162, 1995.

[63] H.S. Fresser, F.E. Prins, and D.P. Kern. Low-energy electron detection in microcolumns. *J. Vac. Sci. Technol. B*, 13(6):2553–2555, 1995.

[64] H.S. Gross, F.E. Prins, and D.P. Kern. New method for fabrication of an array of individually controllable miniaturized electrostatic lenses. In *Proceedings of MNE96, Glasgow, England*, 1996.

[65] C. Stebler, U. Staufer, M. Despont, T.H.P. Chang, K.Y. Lee, and S.A. Rishton. Microcolumn based low energy e-beam writing. *Microelectronic Engineering*, 30:45–48, 1996.

[66] P.W. Hawkes and E. Kasper. *Principles of Electron Optics.* Academic Press, New-York, 1989.

[67] J.T.L. Thong. *Electron Beam Testing Technology.* Plenum Press, New-York, 1993.

[68] I. Brodie and J.J. Muray. *The Physics of Microfabrication.* Plenum Press, New-York, 1981.

[69] P. Dahl. *Introduction to Electron and Ion Optics.* Academic Press, New-York, 1973.

[70] P.W. Hawkes. *Electron Optics and Electron Microscopy.* Taylor & Francis LTD, London, 1972.

[71] C. Stebler, U. Staufer, and M. Despont. Miniaturized e-beam writer: testing of components. *Microelectronic Engineering*, 27:155–158, 1995.

[72] M.G.R. Thomson. *J. Vac. Technol. B*, 12(6):3468, 1994.

[73] B. Schmidt, J. von Borany, U. Todt, and A. Erlebach. Preparation and characterization of ultrathin crystalline silicon membranes. *Sensor & Actuators A*, 41-42:689–694, 1994.

[74] Technical data of Schott Schleiffer AG, CH-8714 Feldbach.

[75] U. Behringer et al. Membrane mask technology. In *Proceedings of the VDI Conference on Mask Technology*. VDI Verlag, 1993.

[76] W. Appel *et al.*: Lithography independent nanometer silicon MOSFET's on insulator. *to be published in the special issue on "Present and Future Trends in Device, Science and Technology" of the IEEE Trans. Electron Dev.* (Sept. 1996).

[77] S. M. Sze. *VLSI technology*. McGraw-Hill, Singapore, 1987.

[78] K.Y. Lee et al. Evaluation and application of a very high performance chemicaly amplified resist for electron-beam lithography. *J. Vac. Technol.*, B 11(6):2807, 1993.

[79] G. Wallis and D.I. Pomerantz. Field assisted glass-metal sealing. *J. Appl. Phys.*, 40(10):3946, 1969.

[80] M. Despont, H. Gross, F. Arrouy, C. Stebler, and U. Staufer. Fabrication of a silicon-pyrex-silicon stack by AC anodic bonding. *To be published in Sensors & Actuators A*, pages 69–72, 1996.

[81] P. Kersten, S. Bouwstra, and J.W. Petersen. Photolithography on micromachined 3D surfaces using electrodeposited photoresists. *Sensors and Actuators A*, 51:51–54, 1995.

[82] R.F. Wolffenbuttel et al. Low-temperature wafer-to-wafer bonding using gold at eutectic temperature. *Sensors and Actuators A*, 43:223–229, 1993.

[83] W. Kurz, J.P. Mercier, and C. Zambelli. *Introduction a la science des materiaux.* Presses Polytechniques Romandes, Lausanne, 1987.

[84] C. Stebler, U. Staufer, and M. Despont. Secondary electron imaging by means of a micofabricated electron column. *Submitted to Journal de Physique*, 30:45–48, 1996.

[85] M. Despont, U. Staufer, C. Stebler, H. Gross, and P. Vettiger. Electron-beam microcolumn fabrication and testing. *Microelectronic Engineering*, 30:69–72, 1996.

[86] S. M. Sze. *Semiconductor devices, physics and technology.* John Wiley & Sons, New-York, 1985.

[87] Technical data from HOYA Company, Hoya photsensitive glass - PEG3.

[88] T.R. Dietrich, W. Ehrfeld, M. Lacher, M. Kraemer, and B. Speit. Fabrication technologies for microsystems utilizing photoetchable glass. In *Micro- and Nano- Engineering 95.* Elsevier, 1995.

[89] Technical data from DuPont Electronics Company, RISTON 4700 Series, Aqueous Processable Photopolymer Dry Film Resist.

[90] U.S. Patent 4882245, (1989).

[91] H. Lorenz, M. Despont, N. Fahrni, N. LaBianca, P. Renaud, and P. Vettiger. EPON SU-8: a low-cost negative resist for mems. In *Proceedings of the MME'96 conference, Barcelona, Spain.* Elsiver, Oct. 21-22 1996.